Université de Neuchâtel

Institut de Microtechnique

Longitudinally polarized fields in near-field imaging systems

Thèse

Présentée à la Faculté des Sciences
pour obtenir le grade de docteur ès sciences
par

Emiliano Descrovi

Neuchâtel, août 2005

Thèse de l'Université de Neuchâtel

Date de soutenance : 9 Septembre 2005

Rapporteurs: Prof. H.-P. Herzig (directeur de thèse)
Dr. S. Quabis
Prof. O. J. Martin
Prof. U. Staufer

Mots-clés:
Microscopie optique à balayage en champ proche (SNOM), optique non paraxiale, plasmons de surface (SPP), super-résolution optique, modélisation des champs électromagnétiques, guides d'ondes métalliques.

Keywords:
Scanning Near-field Optical Microscopy (SNOM), non-paraxial optics, Surface Plasmon Polaritons (SPP), optical super resolution, modeling of electromagnetic fields, metallic waveguides.

Université de Neuchâtel

IMPRIMATUR POUR LA THESE

Longitudinally polarized fields in near-field imaging systems

Emiliano DESCROVI

UNIVERSITE DE NEUCHATEL

FACULTE DES SCIENCES

La Faculté des sciences de l'Université de Neuchâtel,
sur le rapport des membres du jury

Mme S. Quabis (Erlangen),
MM. H.-P. Herzig (directeur de thèse),
U. Staufer et O. Martin (EPF Lausanne)

autorise l'impression de la présente thèse.

Neuchâtel, le 10 janvier 2006

Le doyen :

J.-P. Derendinger

Faculté des Sciences
■ Rue Emile-Argand 11 ■ CP 158 ■ CH-2009 Neuchâtel
■ Téléphone : +41 32 718 21 00 ■ Fax : +41 32 718 21 03 ■ E-mail : secretariat.sciences@unine.ch ■ www.unine.ch

to Heidi L.

Introduction

Seguite con me questi occhi sognare,
fuggire dall'orbita...
...e non voler ritornare !

–F. de André–

"There's plenty of room at the bottom". With his famous talk at the annual meeting of the American Physical Society in 1959, the nobel prize Richard Feynman symbolically opened a new season for scientific research. This new perspective is generally labeled with the term *nanotechnologies*. Although an exhaustive definition does not exist yet, we may say that the word *nanotechnologies* indicates a wide range of activities aimed at a controlled manipulation of small objects perhaps down to the atomic scale. A basic condition for the development of such an ability is represented by the possibility of seeing nano-scaled objects. Therefore, it is not astonishing that the evolution path of nanotechnologies necessarily moves through the domain of microscopy. Among all the kinds of imaging tools available today, optical imaging systems are of primary importance. In addition, since many research subjects involve investigations on the optical properties of small objects (macromolecules, particles, nano-structured materials, waveguide, photonic crystals), the monitoring of light-matter interactions constitutes a crucial topic.

When using optical imaging systems, we take profit of the information remotely delivered by light to the detector, after interaction with the sample. Nevertheless, as light moves away from the place of interaction, a part of this information is inevitably lost. If the interacting objects are large enough (as compared to the radiation wavelength λ), this degradation of information is not critical, but if objects are small, they might be barely, or not at all, imaged. With the help of suitable probes, light in close proximity of the illuminated sample can be detected. In this way, an extraordinary richness of information about the sample becomes accessible and we can manage to "see the invisible". Light confined in proximity of the sample is called near-field and near-field microscopy is the branch of microscopy dealing with the detection of such an optical field.

In the domain of near-field microscopy, the rigorous electromagnetic and the optical description of light meet together. When images are formed by detecting optical fields close to illuminated samples, the vectorial and electromagnetic nature of light can not be neglected. In this thesis we focused our attention on the special case of electromagnetic fields oriented parallel to the optical axis (longitudinal fields). The subject is particularly intriguing, as longitudinally polarized fields cannot be detected using standard microscope devices. We mainly considered the interaction of longitudinal fields with microfabricated, fully metal-coated quartz nano-probes, and managed to give a description of their role in the near-field imaging process. The work will be presented as follows.

In the first chapter, an introduction to Scanning Near-field Optical Microscopy (SNOM) is given. Starting from the concept of super-resolution in paraxial imaging systems, we introduce the concept of near-field microscopy. For two of the best known SNOM techniques we demonstrate that a resolution beyond the capabilities of classical microscopes can be, in principle, achieved. Moreover, we present a rigorous electromagnetic description of a simplified SNOM system, and stress the necessity of adequate tools for the understanding and the interpretation of near-field images.

The second chapter is devoted to the description of the SNOM system with which the main part of the experimental work has been performed. The near-field microscope is particularly interesting since it employs an innovative kind of probes: microfabricated, metal-coated quartz probes with no aperture at their apex. The presence of a full metal coating has strong effects in the near-field imaging characteristics of the probes. Results form standard imaging tests are also presented in this chapter. We demonstrate that fully-metalized probes can actually couple evanescent fields and are capable to attain super-resolution.

Microfabricated probes can be used either as light sources or as light collectors. In the third chapter we study their optical response when 3D-oriented fields are collected. We find a non trivial selective collection behavior for longitudinally and transversely polarized fields. Moreover, the lateral resolution of our system shows a clear dependence on the polarization state of the collected field. A phenomenological explanation of this effect, involving a polarization-dependent coupling mechanism of light into the probes, is proposed.

In the fourth chapter we study the behavior of fully-coated transparent probes as light emitters. With the help of a three-dimensional numerical model, we characterize the guiding properties of the probes and analyzed the near-field and far-field emitted patterns. A set of experimental measurements confirms the results expected by simulations and validates our phenomenological model describing the interaction of light with the probes. In addition, the essential role of longitudinal fields in an illumination-mode near-field scanning system is underlined. We managed to directly measure the longitudinally-polarized, ultra-small hot spot produced at the metallic apex, after injection of a radially polarized mode into the probe.

An alternative way of producing longitudinally polarized light source for near-field imaging is proposed in the fifth chapter. With a set of theoretical calculations, we demonstrate that Surface Plasmon Polaritons (SPP) excited on structured metallic thin films can be exploited as non-radiating, strongly localized light sources. The study presented in this chapter is purely computational: no practical implementation of the proposed device has been performed yet.

A conclusive summary of this work is presented in the sixth chapter.

Contents

Chapter 1

Super-resolution and near-field microscopy

In the last two decades, the rapid development of domains such as micro and nano-technology, material science and molecular biology has underlined the urgent need of non-invasive imaging systems providing highly magnified sample images. A large diversity of optical systems making use of macroscopic optical elements (lenses, mirrors) have been developed and are now accessible for a wide range of different applications. Nevertheless, the lateral resolution of all these instruments is fundamentally limited to 250-300 nm by diffraction of light.

A general definition of resolution limit is somewhat arbitrary and depends on particular working conditions such as coherence of illumination and type of sample used. Probably the best known definitions come from the works of Lord Rayleigh, Sparrow and Abbe. Rayleigh and Sparrow based their resolution criteria on the ability of optical systems to distinguish two point-like sources in the image plane [1, 2], while Abbe was mostly concerned with imaging problems involving gratings and periodic objects [3]. In spite of the small differences between these definitions, it is widely accepted that the lateral resolution of standard far-field imaging systems does not exceed $\sim \lambda/2$. Although the diffraction limit can be interpreted as a particular case of the more general Heisenberg uncertainty relation, it does not represent a fundamental barrier for optical imaging [4] and it can be overcome in different ways. With the term *super-resolution* we indicate the ability of an optical system to image details smaller than half a wavelength [5]. Thanks to technological progress, several kinds of imaging systems can carry out optical super-resolution in various experimental situations, ranging from optical data storage to thin film analysis and single molecule detection. Among them, we cite, for instance, the Kino's solid immersion lens [6], the scanning holographic microscope [7] and the STED microscope [8].

A particularly important class of imaging devices is represented by scanning systems. In a scanning system, the image is sequentially obtained by raster scanning a sample illuminated with structured light. In this chapter, three kinds of scanning systems are considered: the conventional microscope, the Scanning Confocal Microscope (SCM) and the Scanning Near-field Optical Microscope (SNOM). We will describe the theoretical basis of scanning systems, with particular emphasis on their resolution capabilities. Some general hints on the use of super resolving pupil masks for the improvement of SCM resolution limit will be proposed as well. The last section is devoted to the description of SNOM. Within the "physical optics" approximation [9], we propose a simple model for a tutorial explanation of SNOM operating in illumination [10] and collection mode [11]. After demonstrating that super-resolution can be achieved with both operation modes, we conclude the chapter by recalling that the strong limitations of such a scalar model motivate the need of deeper investigations on the response of SNOM systems with rigorous electromagnetic tools.

1.1 Optical scanning systems in paraxial approximation

In this section we consider two arrangements of optical scanning systems: the conventional (or Type I) microscope and the confocal (or Type II) microscope. In the following, we go through the formalism describing image formation in these devices by using a one-dimensional model and a scalar approximation of optical fields. To this aim, we assume the Numerical Aperture (*NA*) of lenses involved in the model to be small.

Imaging systems are linear if we ignore the role of the detector. Therefore, images can be expressed as superposition integrals of the form

$$U_i(x) = \int_{-\infty}^{+\infty} h(x, x') U_o(x') \, \mathrm{d}x' \ , \tag{1.1}$$

where $U_i(x)$ is the field distribution in the image plane, $U_o(x)$ the object field and $h(x, x')$ the impulse response of the system. The object is represented by a complex transmission function. Since an ideal imaging system is space invariant, it is possible to write Eq. 1.1 as a convolution

$$U_i(x) = h(x) \circ U_o(x) = \int_{-\infty}^{+\infty} h(x - x') U_o(x') \, \mathrm{d}x' \ . \tag{1.2}$$

The impulse response $h(x)$ (also known as the Point Spread Function -*PSF*-) represents the system response to a point-like input $\delta(x')$:

$$h(x) = \int_{-\infty}^{+\infty} h(x - x') \delta(x') \, \mathrm{d}x' \ . \tag{1.3}$$

In the following, we will discuss the lateral resolution of the considered imaging systems in terms of their *PSF*.

An optical system represented by a single, aberration-free lens with focal length f and (one-dimensional) pupil width W is characterized by a *PSF* proportional to the following expression

$$h(x) \propto W \frac{\sin 2NA\pi x/\lambda}{2NA\pi x/\lambda} \ , \qquad\qquad NA = n \sin\theta \ , \tag{1.4}$$

where n is the refraction index of the medium in which the lens is working and θ is one half of the lens angular aperture. If we place a point-like source at ∞, the lens entrance pupil is illuminated by a plane wave. In this condition, the *PSF* is realized in the lens focal accordingly to Eq. 1.4. The position of the *PSF* first zero with respect to the central peak can be considered as an estimation of the smallest lateral distance resolved by the imaging system: $\lambda/2NA$. In the best case, an imaging system (in air) can achieve a resolution of $\lambda/2$.

If the object lies between $-w/2$ and $w/2$, the image (assuming magnification equal to one) is described by the following expression

$$U_i(x) \propto W \int_{-w/2}^{+w/2} U_o(x') \cdot \frac{\sin 2NA\pi(x-x')/\lambda}{2NA\pi(x-x')/\lambda} \, \mathrm{d}x' \; . \tag{1.5}$$

Let us define a new integration variable $X = 2NAx/\lambda$ and the *Shannon number* $\mathcal{S} = NAw/\lambda$. Eq.1.5 can now be written as:

$$U_i(X) \propto W \int_{-\mathcal{S}/2}^{+\mathcal{S}/2} U_o(X') \cdot \operatorname{sinc} \pi(X-X') \, \mathrm{d}X' \; , \tag{1.6}$$

which clearly shows that the frequency band of the imaging system is always limited to $[-\pi, \pi]$ for any *NA*. The 2-dimensional result obtained so far is valid for scalar fields, but vectorial generalizations to 3-dimensional geometries are possible [12].

In a scanning system, the object illumination is provided with structured light. In the simplest arrangement, illumination is constituted by a focused plane wave. In Fig. 1.1 the basic setup of a scanning system is presented.

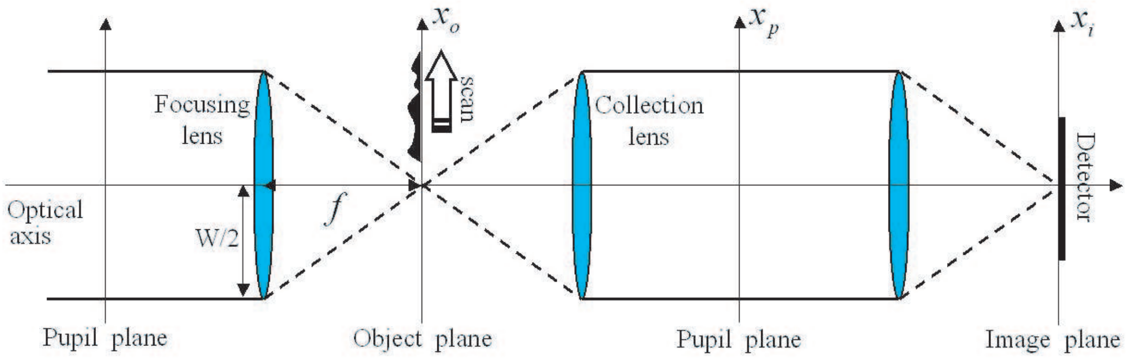

Figure 1.1: Schematic representation of an imaging scanning system.

A plane wave is filling the entrance pupil of the focusing lens, thus providing the illumination field of the scanning target. In the focal plane of the focusing lens, the moving object is defined by a complex function $U_o(x_o - s)$, where s represents the scanning variable. The scanning variable s indicates the time-dependent relative shift of the object reference system with respect to the fixed reference system of the object plane. After the interaction with the object, light is collected by a collection lens and focused again on the image plane where the detector is placed. For sake of simplicity, we assume all the lenses in the setup having the same *NA*. The collection lens "sees" an input field given by

$$U_o'(x_o - s) = U_o(x_o - s) \cdot \frac{\sin 2NA\pi x_o/\lambda}{2NA\pi x_o/\lambda} \; . \tag{1.7}$$

For each position s of the object, the image can be calculated by applying Eq. 1.7 to Eq. 1.6. After the linear transformation of the scanning variable $S = 2NA\, s/\lambda$, we obtain

$$U_i(X_i; S) \propto \int_{-\infty}^{+\infty} U_o(X_o - S) \cdot \operatorname{sinc} \pi X_o \cdot \operatorname{sinc} \pi (X_i - X_o)\, \mathrm{d}X_o \; . \tag{1.8}$$

This linear expression is also known as the Fredholm equation of the first kind. Because of the spatial limitation of both illuminating field and object, we could spread to ∞ the integration limits without loosing in generality. The integrand of Eq. 1.8 is constituted by three terms: a moving object $U_o(X_o - S)$, an illumination $PSF_{ill} = \operatorname{sinc} \pi X_o$ and the collection $PSF_{coll} = \operatorname{sinc} \pi (X_i - X_o)$. Once the general expression of the field in the image plane is obtained, we can go further and consider the two following cases.

1.1.1 Type I scanning system

The type I scanning system is basically a conventional microscope arranged in a scanning configuration. It is used in optical disc read-out systems [13]. The detector is extended over a large region of the image plane and its read-out signal results from the integration over the whole photosensitive area.

As specified above, the resolution limit can be estimated by studying the system response to a point-like input. For this purpose, we perform an ideal scan of a point-like object $U_o(X_o) = \delta(X_o)$. The total intensity I_i hitting the detector is then given by

$$\begin{aligned} I_i(S) &\propto \int_{detector} \left| \int_{-\infty}^{+\infty} \delta(X_o - S) \cdot \operatorname{sinc} \pi X_o \cdot \operatorname{sinc} \pi (X_i - X_o)\, \mathrm{d}X_o \right|^2 \mathrm{d}X_i = \\ &= \int_{detector} \left| \operatorname{sinc} \pi S \cdot \operatorname{sinc} \pi (X_i - S) \mathrm{d}X_o \right|^2 \mathrm{d}X_i = \\ &= \operatorname{sinc}^2 \pi S \cdot \int_{detector} \operatorname{sinc}^2 \pi (X_i - S) \mathrm{d}X_i \; . \end{aligned} \tag{1.9}$$

If the detector area is large enough, the last integral in Eq. 1.9 represents a constant contribution. Ignoring multiplicative constants, the intensity *PSF* of a type I scanning system is then given by

$$I_i(S) \propto \operatorname{sinc}^2 \pi S \; . \tag{1.10}$$

As the detected intensity of a point-like object is proportional to the square of the lens *PSF*, the resolution limit is given by the half-width of the *PSF* central lobe, i.e. the diffraction limit $\lambda/2NA$.

1.1.2 Type II scanning system

In Type II (or confocal) scanning systems, the detector in the image plane is considered as point-like, and placed on the optical axis. Experimentally, this conditions can be carried out with the use of a pinhole in front of the detector.

By setting $X_i = 0$ in Eq. 1.8 we get rid of the integration over the detector area. We obtain:

$$\begin{aligned} I_i(S) &\propto \left| \int_{-\infty}^{+\infty} \delta(X_o - S) \cdot \operatorname{sinc} \pi X_o \cdot \operatorname{sinc} \pi(-X_o) \, \mathrm{d}X_o \right|^2 = \\ &= \left| \int_{-\infty}^{+\infty} \delta(X_o - S) \cdot \operatorname{sinc}^2 \pi X_o \, \mathrm{d}X_o \right|^2 = \\ &= \operatorname{sinc}^4 \pi S \; . \end{aligned} \tag{1.11}$$

The detected intensity is proportional to the fourth power of the lens *PSF*, meaning that the field amplitude is imaged via convolution with the squared *PSF*. In the most general case, the effective amplitude *PSF* of the system is given by the product of the illumination and collection impulse responses. Strictly speaking, if we define the resolution of the imaging system as the position of the *PSF* first zero with respect to the *PSF* peak, a confocal scanning system is equivalent to a standard microscope in terms of resolution performances. Otherwise, if we consider the resolution as the *PSF* Full Width Half Maximum, then a confocal microscope can take advantage of a narrower *PSF*, with a gain of $\simeq 20\%$ in resolution. The term *ultra-resolution* is sometimes used in this case .

1.1.3 Resolution improvements of SCM systems

Confocal microscopes are particularly useful for imaging three-dimensional objects because of their unique optical sectioning property [14]. Nonetheless, the possibility of modify the effective impulse response of the system by properly engineering the illumination and collection *PSF* makes confocal microscopy very promising for achieving super-resolution. Well-established super-resolving techniques are based on the use of particular amplitude/phase masks providing a very narrow spot for sample illumination.

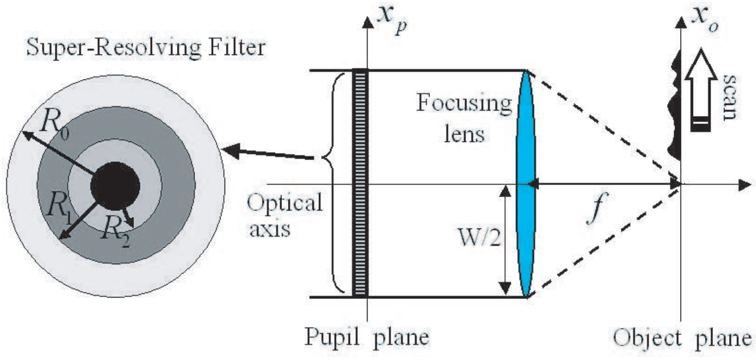

Figure 1.2: Schematic representation of the illumination part of a scanning system with a pupil-plane super-resolving filter.

Super-resolving filters are usually placed in the pupil plane of the focusing lens (Fig. 1.2) and sometimes employed in conjugate pairs in illumination and collection lens pupil planes [15, 16].

Pupil-plane super-resolving filters were firstly proposed by Toraldo di Francia [17] in analogy with highly directive microwaves antennas. After this pioneering work, a number of similar filters have been also proposed [18, 19]. Toraldo filters are composed by a series of concentric annuli having different complex transmission coefficients. By carefully choosing the transmission coefficients, it is possible to produce an arbitrary small spot surrounded by a dark ring. Unfortunately, pupil-plane filters present some severe limitations, such as dramatic losses of light in the central spot and very bright sidelobes limiting the field of view.

The intimate working mechanism of Toraldo filters is based on a controlled pattern interference from annular masks. Let us consider the general case of a N-ring pupil filter (outer radius R_0) placed in front of a focusing lens having the same radius. The *PSF* of such a system, expressed in the dimensionless variable $\rho = 2NA\pi\, r/\lambda$, is given by

$$\Psi(\rho) \propto \sum_{j=1}^{N} c_j \cdot \psi_j(\rho) \; , \tag{1.12}$$

where $\psi_j(\rho)$ represents the contribution of the j^{th} ring and c_j the corresponding complex transmission coefficient. Accordingly to the Babinet theorem, the function $\psi_j(\rho)$ can be written in the following way

$$\psi_j(\rho) = \pi\Big(R_{j-1}^2 \frac{2J_1(\rho R_{j-1}/R_0)}{\rho R_{j-1}/R_0} - R_j^2 \frac{2J_1(\rho R_j/R_0)}{\rho R_j/R_0}\Big) \; , \qquad j = 1, 2, \ldots N \; . \tag{1.13}$$

The general expression of the Toraldo filter *PSF* has $2N$ degrees of freedom, represented by the N radii R_j defining the ring structure and the N transmission coefficients c_j. Once the normalization factor of the *PSF* is fixed, the remaining $2N-1$ constraints that are needed to completely define the system can be arbitrarily chosen. Toraldo di Francia suggested to simplify the problem by using a defined sequence of N radii $R_j = R_0\sqrt{1 - j/(N+1)}$, which is such that all the annuli have the same area $\pi R_0^2/(N+1)$. The remaining $N-1$ constraints can be fixed by imposing the zero points of the $\Psi(\rho)$ function. In this way, the extension and the amount of light contained in the dark ring surrounding the central peak can be controlled. A typical pattern of a 4-ring Toraldo filter is shown in Fig. 1.3. The giant sidelobes shown in the picture represent probably the most limiting aspect of this kind of filters. Although it is possible to reduce the sidelobes level by a suitable multiplication of illumination and collection *PSF* [15], the usable field of view is still very small.

The performance of the pupil filter can be studied by means of some important parameters such as the Strehl ratio, the spot width, the signal-to-noise ratio (SNR) in the dark ring. Sales *et al.* [16] pointed out that all these parameters cannot be optimized at the same time and trade-off must be attained. After some thousands of calculated filter configurations, we can outline the following general trends:

- as the spot becomes larger, the SNR of the pattern increases;
- the dark region surrounding the spot cannot be arbitrarily enlarged while keeping constant the number of rings of the filter and the level of background at the same time;

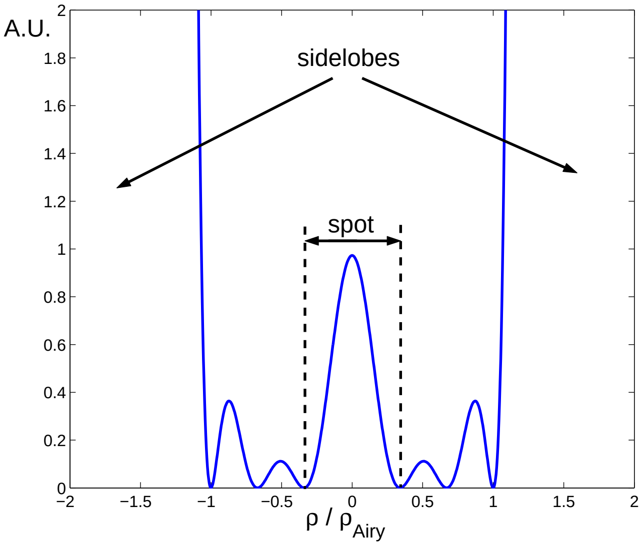

Figure 1.3: Point Spread Function of a 4-ring Toraldo di Francia filter placed in the pupil plane of a lens. The half-width of the central peak is 20% of the Airy radius. Beyond the dark region surrounding the spot, two bright giant sidelobes are visible.

- better PSF profiles can be obtained using a large number of rings, but the energy contained in the spot drops exponentially each time a ring is added.

An example of the this last point is showed in Fig. 1.4.

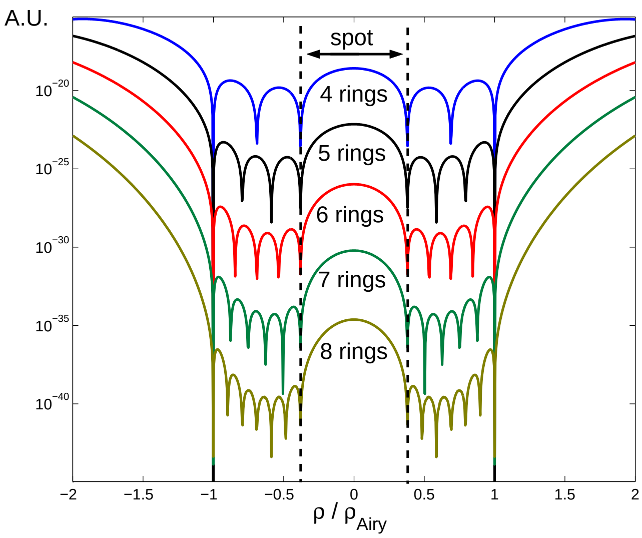

Figure 1.4: Logarithmic representation of the Point Spread Function of a series of Toraldo di Francia filters placed in the pupil plane of a lens. In each profile, the central spot has always the same width ($\simeq 0.38\rho_{Airy}$) and the dark region has the same lateral extension ($\simeq \rho_{Airy}$).

There we consider different filter configurations (with $N = 4, 5, 6, 7, 8$ rings) producing patterns with a constant central spot width ($\simeq 0.38\rho_{Airy}$) and dark region extension

($\simeq \rho_{Airy}$). As the SNR decreases, the energy contained in the spot drops by several orders of magnitude and the brightness of the sidelobes increases drastically. Toraldo di Francia proposed to confine the giant sidelobes in the evanescent region of the diffraction pattern by forcing a strong enlargement of the dark ring surrounding the peak. In order to implement this concept, very small filters would be necessary, and the existence of the ultra-small spot would be assured only in close proximity of the mask. The realization of a illumination system capable of super-resolving features becomes, therefore, naturally connected to the domain of near-field microscopy.

1.2 Aperture near-field optical scanning systems

In the previous section we considered optical imaging systems based on scanning mechanisms. Their working principle is based on a localized sample illumination and a confocal light collection. The lateral resolution depends on the product of two impulse response functions, associated to the illumination and the collection part of the system respectively. The narrower the impulse response function is, the better is the lateral resolution. Eq. 1.4 shows that a *PSF* having a central peak smaller than the diffraction limit $\lambda/2$ can be obtained if $NA > 1$ is provided. This condition suggests that evanescent field (associated to high spatial frequencies) plays a crucial role in achieving super-resolution. Scanning optical microscopes able to operate in the near-field region of the sample are called SNOM. We distinguish between SNOM operating in illumination-mode and in collection-mode: the former provides a very localized light distribution for sample illumination, while the latter collects the evanescent components of the scanned field.

1.2.1 Illumination-mode SNOM

In his visionary work, Synge [10] proposed a method for obtaining an ultra-small spot to be used for sample illumination. The principle is sketched in Fig. 1.5.

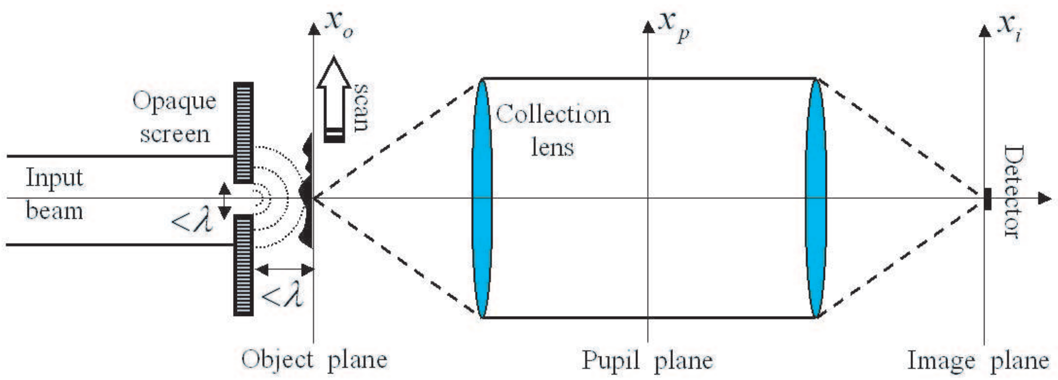

Figure 1.5: Schematic representation of the Synge's idea for an illumination-mode SNOM.

An opaque screen with a subwavelength-sized hole is used as a nano source of light. At small distances from the aperture, the distribution of the emitted light is confined in a region of space smaller than $\lambda/2$. As the sample is scanned through the probing spot, light is collected by a lens system in a confocal (type II) mounting. Assuming an ideal point-like source in contact with the sample, the resulting image can be obtained by means of Eq. 1.8

$$U_i(S) \propto \int_{-\infty}^{+\infty} U_o(X_o - S) \cdot \delta(X_o) \cdot \operatorname{sinc} \pi(-X_o)\, \mathrm{d}X_o = U_o(S)\ . \tag{1.14}$$

The last expression demonstrates that a complete recovery of the object in the image plane can be, in principle, obtained.

For a more concrete illustration of the illumination-mode SNOM working principle, we built up the following one-dimensional scalar model [4]. Let the probe be a nano-sized slit $W_p = 20$ nm wide illuminated by a $\lambda = 633$ nm collimated laser beam and let the object be a subwavelength slit $W_o = 80$ nm wide. In addition, let the collection optics be characterized by $NA = 0.1$. All optical elements in the model are described in the thin-element approximation. If we place the probe at a distance d from the object plane, the collecting lens will see the following object field

$$U'_o(x_o - s) = U_p(x_o; d) \cdot U_o(x_o - s)\ , \tag{1.15}$$

where $U_p(x_o; d)$ represents the field emitted by the probe aperture at a distance d. After the interaction with the object, light is low-pass filtered by the lens, then focused on the image plane and detected by the on-axis point-like detector. Three scans at different distances d have been simulated. The results are presented in Fig. 1.6. Calculation have been carried out by means of the angular spectrum representation of scalar optical fields.

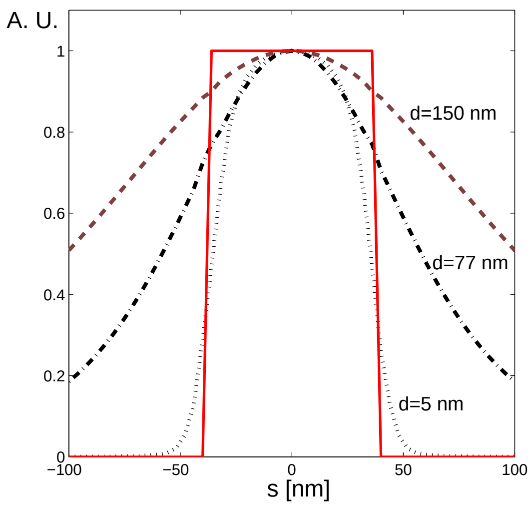

Figure 1.6: Scan of a slit ($W_o = 80$ nm) performed by a rectangular probe ($W_p = 20$ nm) serving as light source. Three sample-source distances are considered: 5 nm (dotted line), 77 nm (dash-dotted line) and 150 nm (dashed line). The object profile is also shown (solid line).

We remark that the resolution of the detection system falls off as the distance source-sample increases. Super-resolution is achieved if the illuminating spot is smaller than the diffraction limit. This condition is satisfied as long as d and W_p are small ($\sim 10-100$ nm).

The influence of the probe size on the lateral resolution is considered in Fig. 1.7, where the profile of the object slit scanned by three different probes at $d = 5$ nm is presented.

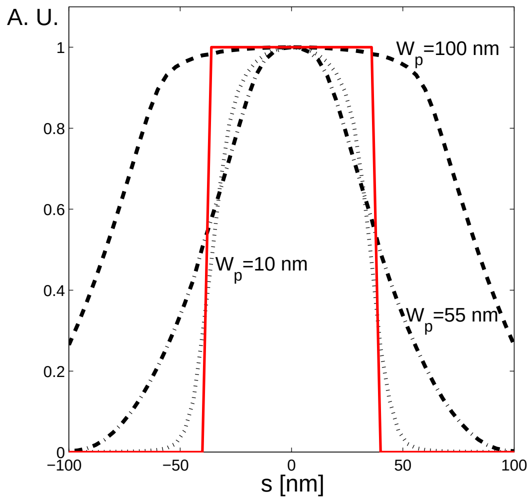

Figure 1.7: Scan of a slit 80 nm wide performed by rectangular probe serving as light source. Three aperture widths W_p are considered: 10 nm (dotted line), 55 nm (dash-dotted line) and 100 nm (dashed line). The object profile is also shown (solid line).

Although the use of small probe apertures provides a good lateral resolution, it reduces dramatically the amount of transmitted light (Bethe's law). In 1984, a remarkable work of Lewis *et al.* demonstrated that visible radiation transmitted through small metal apertures (diameter $\simeq$ 30 nm) can still be detected [20]. In the same year, Pohl *et al.* developed the first illumination-mode SNOM, by opening a subwavelength pupil at the end of a metalized quartz tip [21]. The use of a sharp probe instead of a flat screen was particularly promising, because of the possible exploitation of sample-probe distance control systems based on localized mechanical interactions.

1.2.2 Collection-mode SNOM

In a complementary implementation of SNOM, a small aperture in the opaque screen is used as a light collector (Fig. 1.8). The first implementation of such a collection-mode SNOM was reported by Betzig *et al.*, who employed an Aluminum-coated micro-pipette with an aperture of 150 nm diameter at its apex [11].

Image formation in a collection-mode SNOM system is described by Eq. 1.14, provided that the collecting aperture is point-like and in contact with the sample. Therefore, the collection-mode SNOM is also capable of super-resolving features. When the one-dimensional scalar model is applied to a slit-on-slit arrangement working in collection-mode, results in complete analogy with the illumination-mode configuration are found.

If the vectorial nature of optical fields and the finite dimensions of object and probe are taken into consideration, the scalar approximation we used so far is inadequate. Therefore, a rigorous computation method is necessary for a full understanding of the near-field image formation. We consider again an object represented by a slit in a opaque screen. The

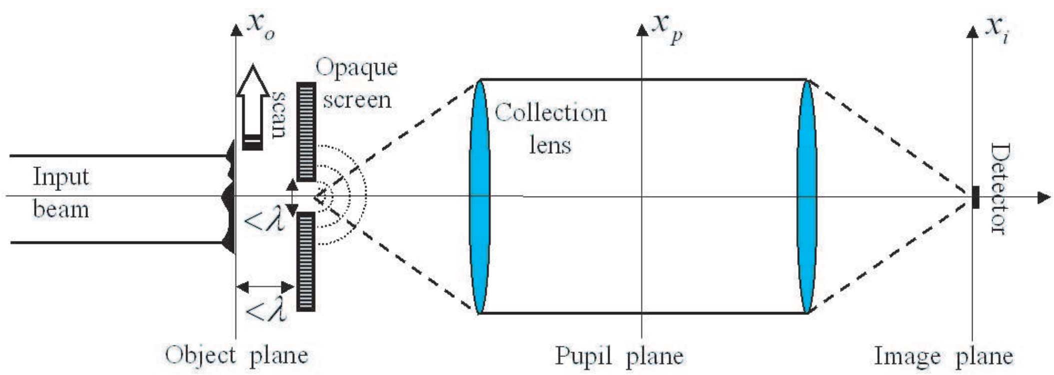

Figure 1.8: Schematic representation of a collection-mode SNOM.

aperture is 80 nm wide and is etched in a highly conductive metal film ($\epsilon = 1 + i10^5$), 18 nm thick. The structure is illuminated with a plane wave TM or TE polarized. Near-field distribution of the electric field squared amplitude in both illumination cases is shown in Fig. 1.9. Calculations have been carried out by means of the Moment Method proposed by Totzech and Tiziani in Ref. [22].

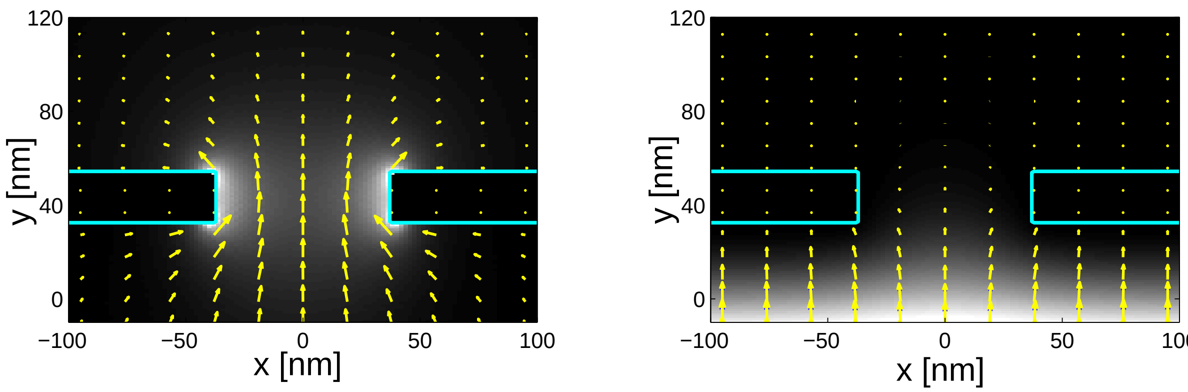

Figure 1.9: Squared amplitude of the electric field (color plot) and Poynting vector distribution (arrow plot) in the near-field region of a slit illuminated by (a) TM-polarized and (b) TE-polarized plane wave. The arrow lengths are proportional to the modulus of the Poynting vector and are barely visible in the half space beyond the slit because of the low power transmittance.

The boundary conditions imposed by Maxwell's equations on the electromagnetic field vector at metal-air interfaces gives rise to two different electric field distributions in the near-field region. Depending whether the electric field is tangential or perpendicular to the slit borders, we observe a complete absorption of the field (Fig. 1.9(a)) or a depolarization effect [23] (Fig. 1.9(b)). The integral method used for the previous calculations can also be employed to simulate a scan process. The collection probe is represented by a slit 20 nm wide, etched in a highly conductive metal film ($\epsilon = 1 + i10^5$), 18 nm thick. The probe scans the object slit at a distance of 5 nm. The transmitted power is low-pass filtered in order to simulate the collection of a standard lens of $NA = 0.1$ [1]. The final read-out signal is calculated by integrating the filtered power flow reaching the upper boundary of the calculation domain (Fig. 1.10).

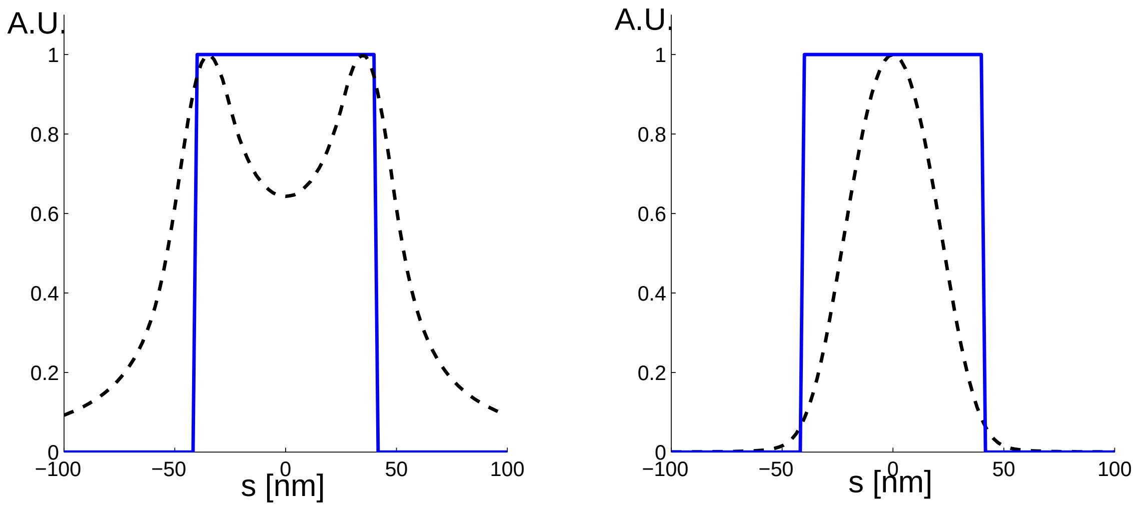

Figure 1.10: Slit profile as scanned by a 20 nm wide collection aperture at a distance of 5 nm: (a) TM-polarized and (b) TE-polarized illumination. The object (solid line) is superposed to the read-out signals (dashed lines) for comparison purposes.

The probe can actually map the two different field distributions associated to different polarization states of the field. The detected field does not represent necessarily the image of the investigated structure, but the image of its near-field distribution. As long as the probe does not introduce non-linearities in collection, a detailed recovery of the near-field distribution is, in principle, possible.

1.3 Conclusions

In this chapter we introduced the concept of super-resolution starting from a far-field approach. We stress that super-resolution in scanning systems is achieved as long as the impulse response functions associated to whether the illumination or the collection part of the imaging system are narrower than $\lambda/2$. We showed that this condition can be satisfied by considering the evanescent field components of the illumination aperture or the illuminated sample.

A 2-dimensional scalar model has been built-up for a tutorial explanation of near-field scanning systems in illumination and collection-mode. On this basis, we concluded that the two systems are equivalent and capable of super-resolving features. Moreover, we demonstrated that a scalar approximation is not anymore satisfactory if polarization-dependent phenomena are kept into consideration.

A rigorous electromagnetic model has been used for the exact simulation of the scan

[1]Lateral resolution of such a SNOM system is weakly dependent on the numerical aperture of the collection optics.

of a metallic slit (illuminated by a TE or a TM polarized plane wave) by a metallic probe-aperture. As long as the probe shows a linear response with respect to the collected field, we showed that it is possible to map the near-field of the illuminated structures. Nevertheless, in a more general case, we cannot neglect the possibility of a depolarization effect played by the probe itself during the scan. In this case, the detected image must be carefully interpreted with the help of rigorous calculation tools.

In the next chapters of this thesis, the polarization-dependent behavior of fully metal-coated SNOM probes are investigated. Particular attention will be paid to those cases where the optical field is not anymore paraxial, and both the electric and the magnetic field vectors are three-dimensionally distributed with respect to the optical axis.

Chapter 2

Collection-mode SNOM system

Controlling of the probe-sample distance is a crucial aspect in near-field microscopy. The use of Synge's planar surface with the nano-sized hole as a probe can not efficiently accomplish to this task. Retro-reaction control systems based on Proportional-Integral-Differential filters (PID) cannot guarantee an accurate sample-probe distance control if they are based on the optical signal detection only, since many factors, other than the change of the scanning distance, may affect the amount of collected light during the scan (e.g. inhomogeneities in the sample optical properties). The use of sharp probes represents a good solution to this problem: the tip apex mechanically interacts with the sample within a very small and localized region, thus allowing a topographic map of the sample. Such an interaction is detectable only in close proximity to surfaces and is related to short-range and long-range forces between sample and probe. Scanning microscopes sensitive to the mechanical interactions of a local probe are called Scanning Force Microscopes (SFM) [24]. In order to exploit mechanical forces for a scanning distance control, SNOM devices are typically equipped with a SFM system mounting sharp probes.

One of the best known implementations of SFM is represented by the Atomic Force Microscope (AFM), invented by Binnig *et al.* in 1986 [25]. In an AFM setup, the probe is constituted by a tip deposited on the bottom face of a thin silicon cantilever. As the probe interacts with the sample, the cantilever experiences a deflection that can be detected. Nowadays, AFM devices are robust and highly performing as they relay on highly reproducible microfabricated probes with well-defined physical characteristics.

The most widely used probe for collection/illumination-mode SNOM are probably constituted by metal-coated tapered optical fibers with an aperture at the apex. Mass fabrication of SNOM probes has not a satisfactory level at the moment. Most of the commercial products are still costumer-based and the reproducibility of the probe is not reliable. For this reason, in the last decade, many research groups tried to develop microfabrication processes aimed at mass producing cantilever-based SNOM probes [26, 27, 28, 29, 30, 31].

In this chapter, the description of a collection-mode SNOM mounting microfabricated cantilever-based probes is presented. In addition, some test results of the microscope imaging standard samples will be shown and commented.

2.1 Atomic Force Microscope

Monitoring of the cantilever deflection can be carried out interferometrically or via piezoelectric, piezoresistive or capacitance measurements. In the present setup we decided to implement the beam deflection method, that is one of the most widely used technique for the cantilever deflection evaluation. As shown in Fig. 2.1, a laser beam ($\lambda = 870$ nm) is split, then reflected downward by a 45° dichroic mirror. Subsequently, the beam is focused on the upper surface of the cantilever by means of an achromat lens having NA=0.3 (Fig. 2.2).

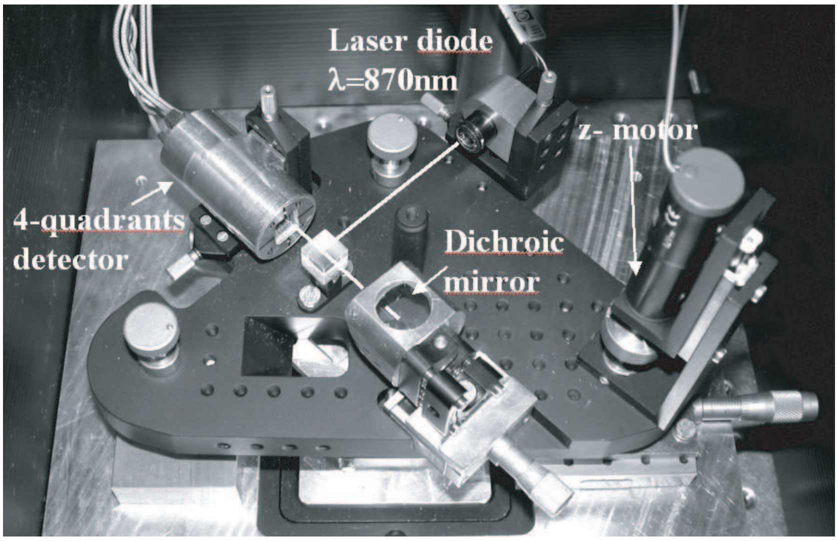

Figure 2.1: Top view of the AFM device.

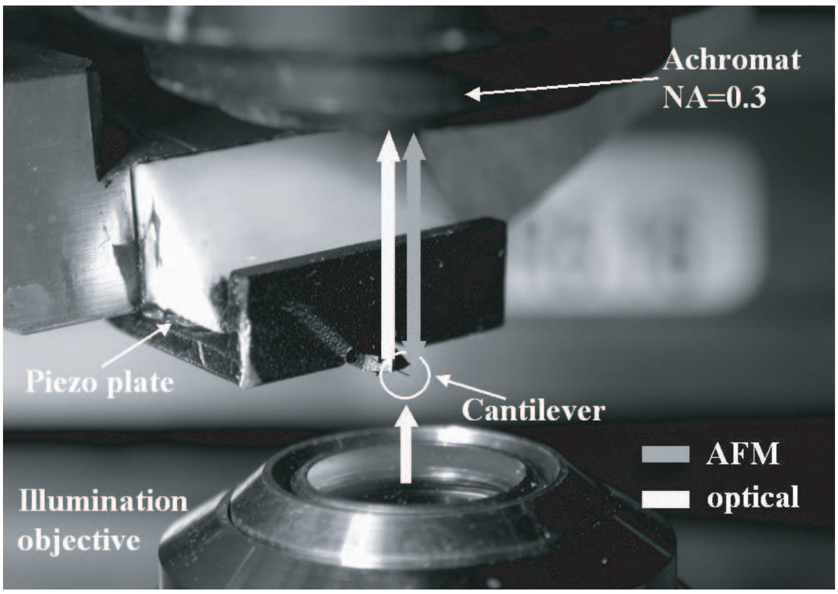

Figure 2.2: Bottom view of the AFM device. Cantilever holder and achromat lens.

The reflected light is re-collected by the achromat and then detected by a 4-quadrants photosensitive diode. The read-out signals of the 4 detectors are processed electronically (AFM Control Unit, APE Research, Trieste, Italy) in a way that vertical and lateral deflections of the cantilever can be measured.

The AFM is also equipped with a piezo plate placed underneath the cantilever chip holder providing a dithering excitation for non-contact operation mode.

In an AFM operating in contact-mode, the tip experiences a soft physical contact with the sample. At such small interaction distances -a few Å-, the force between tip and sample is repulsive (positive van der Waals force). A typical scanning technique consists of performing the scan while keeping the interaction force constant. This can be done with the help of a feedback loop, after evaluating the force acting on the cantilever by measuring its deflection. A constant-height scan is also possible by switching off the feedback loop.

If the oscillations of the cantilever are small compared to the beam width, there is a linear relationship between the vertical displacement of the probe Δz, the vertical displacement of the spot on the 4-quadrant detector and the read-out signal ΔV_z corresponding to the cantilever deflection

$$\Delta V_z = \Delta z \cdot V C_{opt} = \frac{F}{K} \cdot V C_{opt} \ , \tag{2.1}$$

where V is the read-out signal integrated over the 4 quadrants, F is the exerted force, K is the spring constant of the cantilever and C_{opt} represents the normalized detector response slope with respect to vertical displacement. The value of ΔV_z is obtained by a proper algebraic sum of each quadrant signal. After calibration with known samples, the constant C_{opt} can be evaluated. We reached the optimal working conditions with an overall vertical error of 2 nm in contact.

2.2 Microfabricated fully metal-coated probes

The micromachined SNOM probes we used in this setup have been developed at IMT, Neuchâtel by L. Aeschimann [32]. They are constituted by a 12μm-long amorphous SiO_2 tip integrated on a silicon cantilever (Fig. 2.3). The tip is completely coated with a polycrystalline aluminium film having a thickness up to 60 nm. At the tip apex there is no mechanical aperture.

A spring constant can be associated to the cantilever. Moreover, physical parameters are directly connected with the resonance frequency f of the cantilever, accordingly to the following formula [24]

$$t = \frac{2\sqrt{12}\pi}{1.875^2}\sqrt{\frac{\rho}{E}} f l^2 \ , \tag{2.2}$$

where $\rho = 2330$ kg/m^3 is the silicon density, $E = 1.69 \times 10^{11}$ N/m^2 is the silicon Young's modulus and $l = 420$ μm and $t = 3$ μm are the cantilever length and thickness respectively estimated with the aid of a SEM. The calculated resonance frequency is $f_{calc} = 23.4$ KHz. The resonance frequency can also be estimated by directly measuring the oscillation

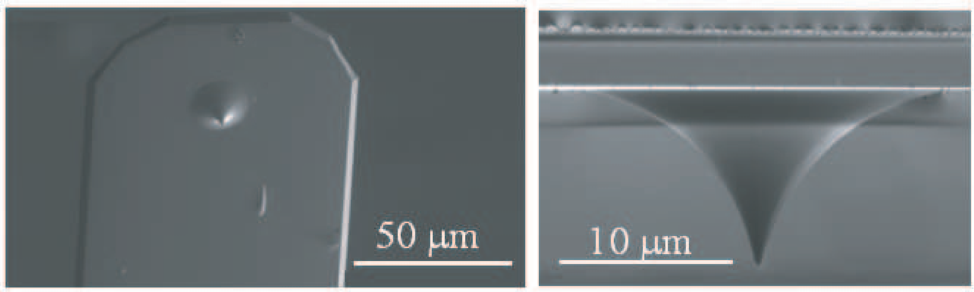

Figure 2.3: SEM pictures of the cantilever-based SNOM probe. A hole (not visible) in the back surface of the cantilever is placed beneath the tip base, allowing light transmission.

amplitude of the cantilever. The mechanical excitation is provided by a dithering piezo plate, driven by a sinusoidal frequency ramp signal. The result, shown in Fig. 2.4, gives a resonance frequency $f_{meas} = 18.8$ KHz.

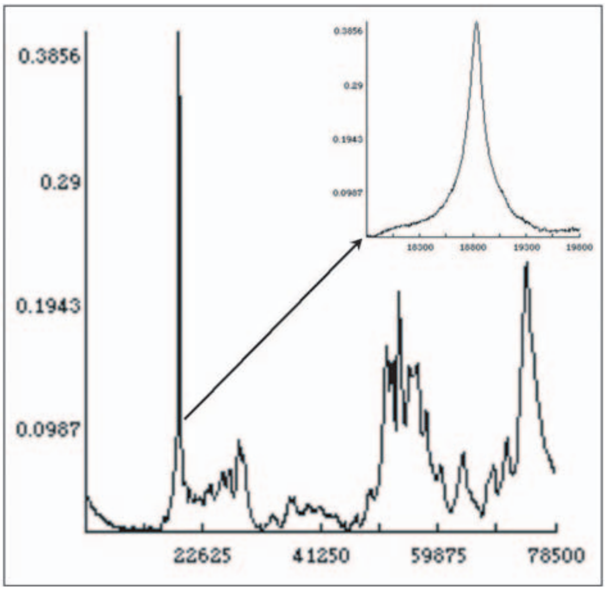

Figure 2.4: Cantilever frequency response to dithering excitation. Resonance frequency peaked at 18.8 KHz (inset).

2.3 Collection-mode SNOM

The Scanning Near-field Microscope we developed is a collection-mode SNOM working in transmission. A schematic diagram of the apparatus is shown in Fig. 2.5. The device has been obtained by complementing the AFM described in the previous section (Fig. 2.6) with suitable collection optics.

The laser source is an Ar^+ laser of 514.5 nm wavelength. The beam is firstly expanded and collimated and then focused on the sample by a microscope objective mounted on the xyz-translator stage. Scans are performed by moving the piezo scanner (PiezoFlexure

StageP-517.3CL) hosting the sample with respect to the probe. Transmitted light is collected by the probe and re-radiated in free-space from the hole on the backside of the cantilever. A confocal collection lens system constituted by an achromat lens (NA=0.3), two objectives (NA=0.4 and NA=0.7, optimized for ∞) and a diaphragm collects the optical signal and focuses it on the detector photosensitive area. The use of such a collection optics assures a satisfactory magnification of the cantilever hole, allowing an efficient spatial filtering with the diaphgram. The detector we used is a photomultiplier (Perkin Elmer MD-952), allowing a tunable gain (up to 10^8). A CCD camera is also employed to align the cantilever hole with the diaphragm.

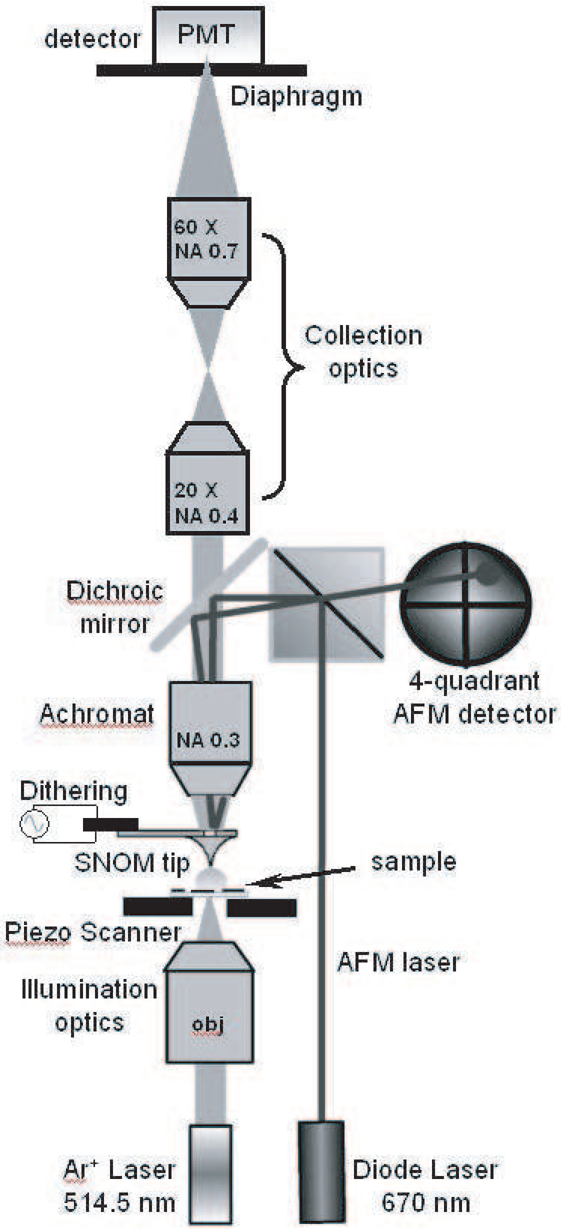

Figure 2.5: Schematic draw of the collection-mode SNOM using microfabricated, cantilever-based tips.

The use of a fully free-space detection system presents some advantages with respect to the standard fibred SNOM. The most important is probably the possibility of performing near-field spectroscopic measurements. On the other hand, the drawback is represented by the large amount of straylight detected during the scan, that constitutes the main source of background during measurements.

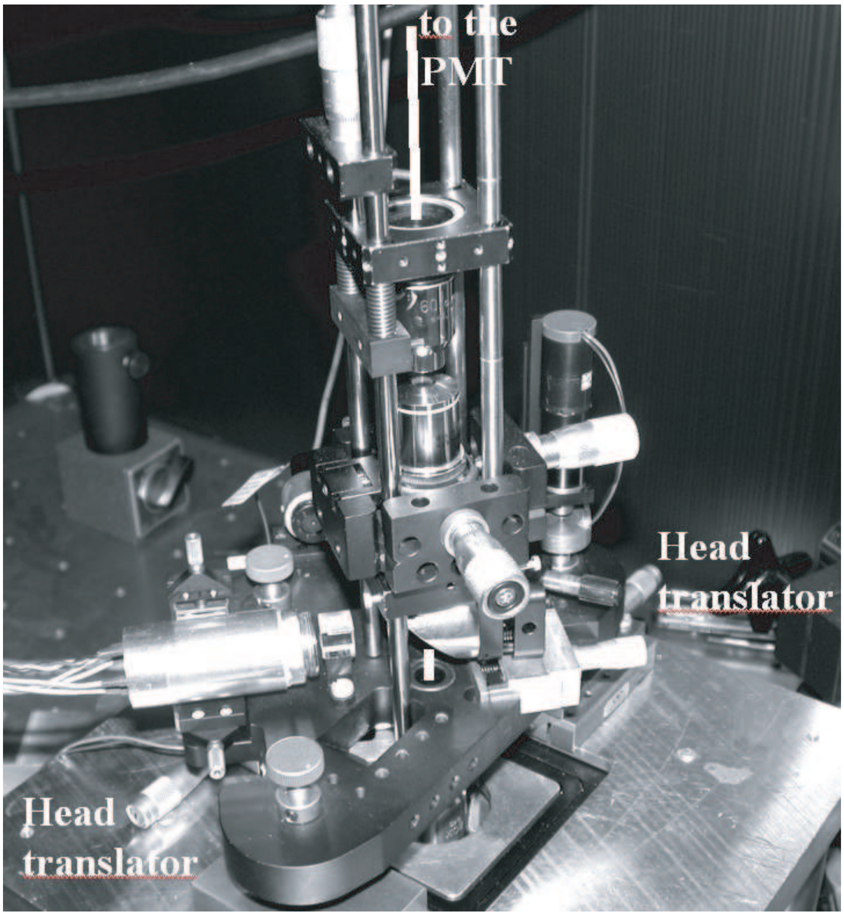

Figure 2.6: Picture of the collection-mode SNOM mounted on the AFM head.

The imaging capabilities of the presented collection-mode SNOM have been studied by performing the following scan tests: scan of Fischer pattern and metallic grating illuminated by focused beam (in transmission) and scan of a stationary optical field in Total Internal Reflection conditions.

2.3.1 Fischer Pattern

The so-called Fischer patterns have been realized by Fischer in 1981 [33]. Nowadays they are commonly used as microscopy test samples. Fischer patterns are produced by an initial deposition of a monolayer of small spheres arranged in an hexagonal latex. The spheres act like a mask for metal vapor deposition. After evaporation of 15 nm of Al, the spheres are dissolved and the resulting structure is a pattern of triangular metallic islands as shown in Fig. 2.7.

The sample is illuminated from the bottom by a focused beam (NA=0.4). Topographic scans are performed in contact-mode, while optical scans are performed in contact-height mode (feedback loop off) at a distance $\lesssim$ 10 nm from the sample. A typical result is shown in Fig. 2.8. Metallic islands are clearly visible in the optical image, meaning that a lateral resolution $\lesssim$ 150 nm has been achieved. Metallic features are absorbing and therefore, they appear opaque (solid circle) as expected. Nevertheless, it is interesting to observe that some triangles in the same image are contrast-reversed (dotted circles in Fig. 2.8(a)). This effect might be caused by asymmetries in illumination or perhaps by multiple reflections tip-sample-tip.

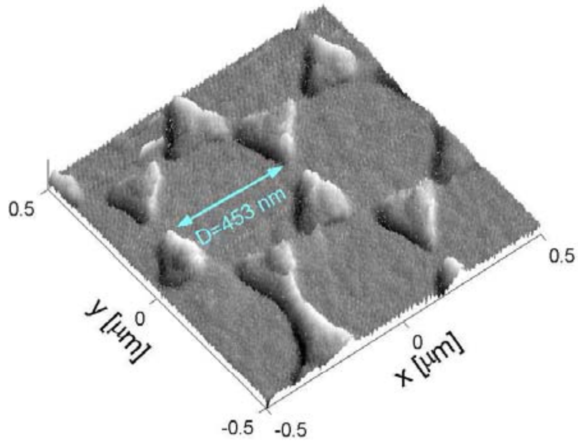

Figure 2.7: Topographic map of a Fischer pattern (Kentax, Seelze, Germany). Sphere diameter 453 nm, structure height 15 nm.

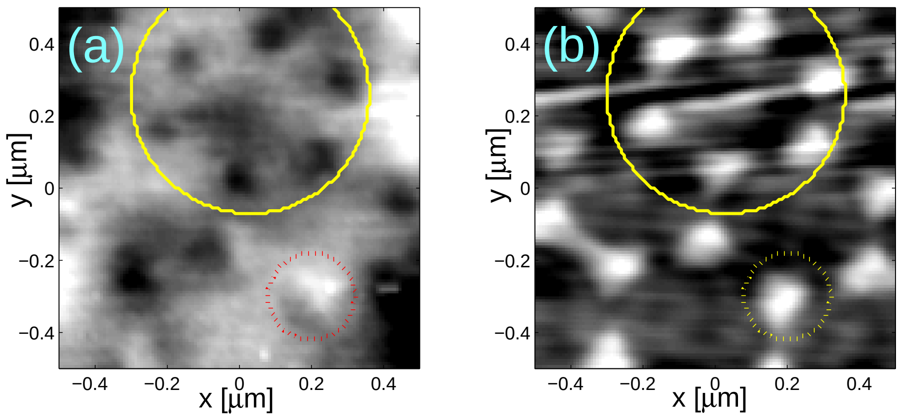

Figure 2.8: Scans of a Fischer pattern: (a) optical near-field image at $\lesssim$ 10 nm from the sample, (b) topography. The circles underline two cases of contrast inversion in the optical image. In one case the metallic island is bright (dotted circle) while in the other case triangles are opaque (solid circle).

2.3.2 Metallic binary grating

A metallic grating of period $\Lambda = 7$ μm, fill-factor $f = 1/7$ and height $h = 70$ nm (Fig. 2.9) has been scanned in contact-height mode (distance probe-sample $\lesssim$ 10 nm). Illumination is provided from the bottom, as in the previous case, by means of a NA=0.4 microscope objective.

Thanks to the straight edges, such a structure is particulary suited for the determination of the topographical and the optical lateral resolution of the microscope.

In Fig. 2.10 the images resulting from a 3μm $\times$ 3μm scan performed with a 60 nm apex diameter probe are reported. The metallic bar is imaged as an opaque zone in the optical image (Fig. 2.10(a)). The sharpness of the edges is highly dependent on the illumination angle with respect to the sample normal. As a tilt is introduced, asymmetric ripple effects appear at the borders.

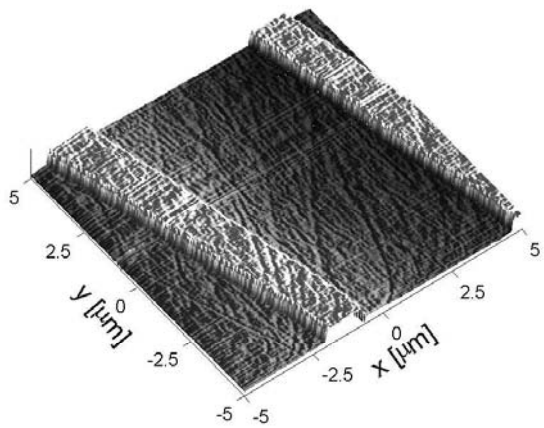

Figure 2.9: Topographic map of a metallic grating. Period 7 μm, fill-factor 1/7, height 70 nm.

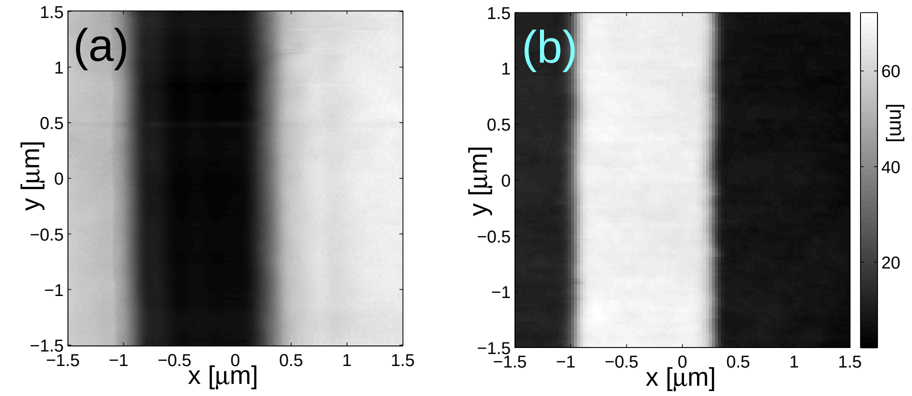

Figure 2.10: In-contact scan of a metallic grating: (a) near-field optical image, (b) topography.

The topographic and optical grating profiles can be obtained by averaging the 2-dimensional distributions of Fig. 2.10 along the y direction. The resulting normalized curves S^{top} and S^{opt} are presented in Fig. 2.11. We can estimate the topographic and optical lateral resolution of the scanning system by considering the lateral extension δx of the structure edge in the two measurements:

$$\delta x^{top} = c_{top}^{-1}\,\delta S^{top} = c_{top}^{-1} \cdot \left[0.9(S^{top}_{max} - S^{top}_{min}) - 0.1(S^{top}_{max} - S^{top}_{min})\right] , \tag{2.3}$$

$$\delta x^{opt} = c_{opt}^{-1}\,\delta S^{opt} = c_{opt}^{-1} \cdot \left[0.9(S^{opt}_{max} - S^{opt}_{min}) - 0.1(S^{opt}_{max} - S^{opt}_{min})\right] , \tag{2.4}$$

where c_{top} and c_{opt} represent the angular coefficients of the straight lines interpolating the measured edges between the limits $\left[0.9(S^{top}_{max} - S^{top}_{min}),\, 0.1(S^{top}_{max} - S^{top}_{min})\right]$ and $\left[0.9(S^{opt}_{max} -\right.$

S^{opt}_{min}), $0.1(S^{opt}_{max} - S^{opt}_{min})$] respectively. The estimated topographical resolution is $\delta^{top}_x \simeq 80$ nm (Fig. 2.11(b)). The optical image presents an asymmetry in the two edges. The sharpest one shows a lateral shift $\delta^{opt}_x \simeq 170$ nm (Fig. 2.11(a)).

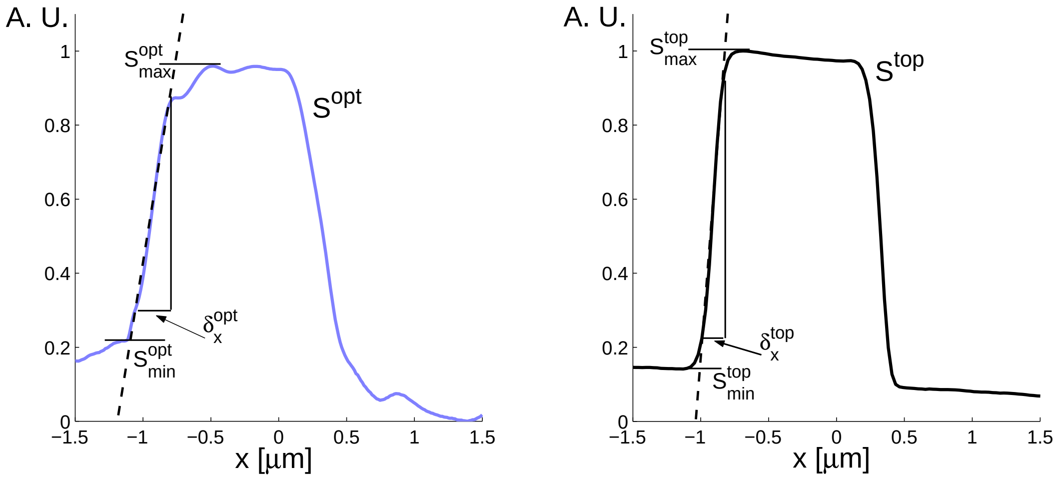

Figure 2.11: Normalized profiles of a metallic grating: (a) reversed optical, (b) topographic.

2.3.3 Stationary evanescent field

The ability of the collection-mode SNOM in detecting a pure evanescent field has been tested by performing a scan of a stationary evanescent wave generated by Total Internal Reflection (TIR) at a glass-air interface of a dove prism. In Fig. 2.12 the schematic of the experimental arrangement is shown.

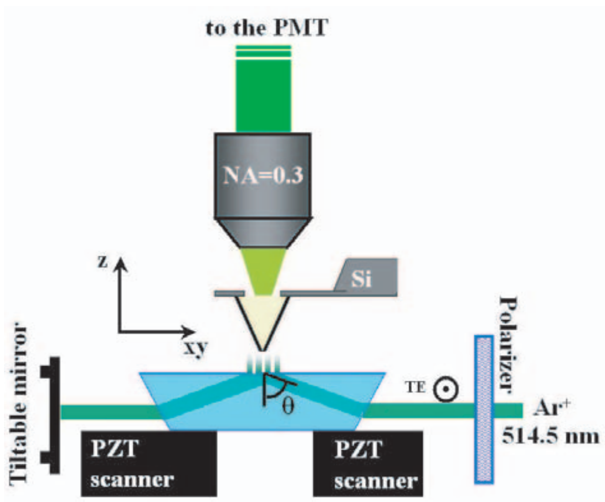

Figure 2.12: Schematic of the experimental setup for the evanescent stationary wave measurement ($\theta \geq 41.5^{o}$).

The stationary evanescent field is created by making two TE-polarized beams interfere at the horizontal interface of a glass ($n = 1.5$) prism at an incidence angle $\theta \geq \theta_c$ (critical angle $\theta_c = 41.5^{\circ}$). With the help of a tiltable mirror, a good alignment of the two interfering beams can be achieved.

The squared amplitude of the interference pattern produced by two evanescent waves of equal amplitude hitting a glass-air interface with the same angle θ is given by the following expression [35]

$$I(x;z) = \frac{1}{2}\exp\Big[-2\frac{z}{z_d}\Big]\cdot\Big[1+\cos(2nk\sin\theta\, x)\Big]\ , \tag{2.5}$$

where $z_d = \lambda/\big(2\pi\sqrt{n^2\sin\theta - 1}\big)$ is the penetration depth of the field in air, and $k = 2\pi/\lambda$. An interference pattern with period $\Lambda \simeq 256$ nm is expected at an incidence angle $\theta = 42^{\circ}$.

In Fig. 2.13(a) the detected interference pattern is shown. An evaluation of the pattern period can be performed by means of spatial frequencies (Fourier) analysis. In Fig. 2.13(b), the modulus of the Fourier Transformation of the image in Fig. 2.13(a) is presented. The zero-order represents just an offset and has been set to zero. We remark that the image has two important frequency contributions, associated to the frequencies $\mathbf{p}^{(1)} = \big(-p_x, p_y\big) = \big(-1.389\,\mu\text{m}^{-1}, 1.389\,\mu\text{m}^{-1}\big)$ and $\mathbf{p}^{(2)} = \big(p_x, -p_y\big) = \big(1.389\,\mu\text{m}^{-1}, -1.389\,\mu\text{m}^{-1}\big)$. They represent two waves propagating in opposite directions. The spatial period can be obtained from the following expression

$$\Lambda = \Big(2\sqrt{p_x^2 + p_y^2}\Big)^{-1} = 254.5\ \text{nm} \pm 20\ \text{nm}\ , \tag{2.6}$$

which is in good agreement with the expected value. The evaluation of the error has been performed by propagating the uncertainty $\delta p = \sqrt{\delta p_x^2 + \delta p_y^2}$ in the frequency domain. This measurement demonstrates that fully-coated near-field probes can couple purely evanescent optical fields.

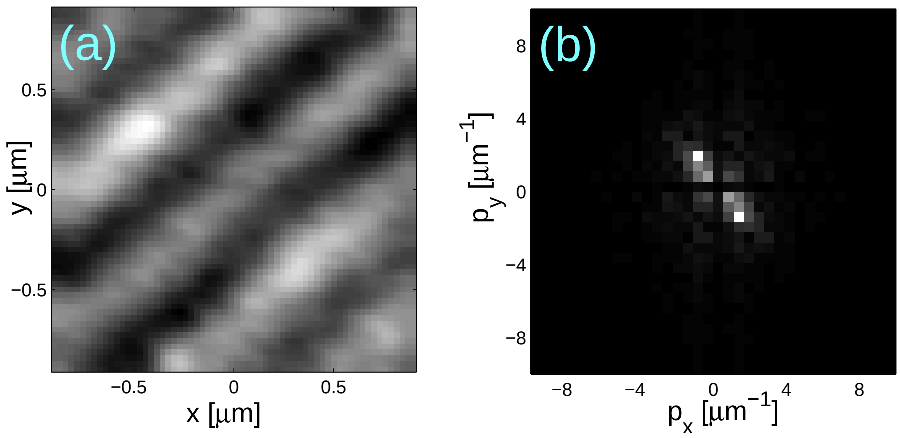

Figure 2.13: Scan of a stationary evanescent field at a distance of $\lesssim 10$ nm from a glass-air interface. (a) optical image of the interference pattern, (b) modulus of the Fourier Transformation of the interference pattern. The zero-order frequency has been set to zero.

2.4 Conclusions

In this chapter we described the experimental setup of a collection-mode SNOM mounting cantilever-based microfabricated probes. A set of tests aimed to evaluate the imaging capabilities of such a device have been presented.

We performed scans of microscopic and subwavelength structures and we were able to resolve their features with a lateral resolution beyond the classical diffraction limit. Nevertheless, the problem of artifacts might arise. In a remarkable paper, Hecht *et al.* [34] suggest several hints to distinguish a "good", artifacts-free near-field image:

- the image is obtained in a constant-height or constant-intensity scan mode
- the image is obtained in a constant-distance mode but:
  - topographic and optical images are uncorrelated
  - the spatial shift between topographic and optical images is constant
  - the lateral resolution of the two images is clearly different

Accordingly to Ref. [34], our investigations have been conducted on "good" near-field images, little or not influenced by artifacts due to the probe z-motion. This conclusion is supported by the following considerations: scans have been performed at constant-height, the optical and topographic lateral resolution are clearly different and poorly correlated.

The super-resolving ability of a SNOM relies on the collection of evanescent fields. In order to check if the fully metal-coated probes are sensitive to evanescent fields, we scanned an evanescent interference pattern at a glass-air interface. An optical image presenting interference fringes has been recorded. If the probe is moved away from the glass surface, the image loses contrast, till it completely disappears at distances $\geq 1\mu$m. We noticed that the fringe contrast is highly sensitive to the polarization state of the incoming beam. The best contrast is obtained for TE-polarized interfering waves. This effect suggests a selective coupling of non-paraxial field into the probe. The particular polarization-dependent collection properties of fully metal coated quartz probe will be studied and discussed in the chapter 3.

Chapter 3

Collection of transversely and longitudinally polarized optical fields

Apertureless scanning near-field optical microscopy (A-SNOM) probes were first proposed by Wickramasinghe and Williams [36] and subsequently developed by Zenhausern [37], where the probe was a standard silicon atomic force microscope (AFM) tip scattering the light transmitted through an illuminated sample. Subsequently, metal probes have also been employed for the same purpose. It was found that metallic tips scatter transversely and longitudinally polarized fields with different relative strengths [38]. This finding underlined that the understanding of the coupling mechanism of non-paraxial polarized optical fields with metallic or fully metalized tips is a crucial topic in SNOM imaging. In a recent paper [39], a phenomenological description of a similar effect, taking place in the collection of light by apertureless microfabricated quartz probes [31, 40] has been reported.

In the present chapter, a study of the optical properties of microfabricated, fully-metal-coated quartz probes in collecting longitudinal and transverse optical fields is presented. In order to obtain information on the probe response to the two polarization directions, an experimental situation where the transverse and the longitudinal fields to be scanned are distributed over different regions of space is highly desirable. There are several ways of producing a longitudinally polarized field having little overlap with a transversely polarized field. One of the most elegant methods consists of focusing a radially polarized beam. In this case, a narrow on-axis longitudinally polarized peak arises on the optical axis, while a transversely polarized field surrounds it over an annular region [41, 42]. The strength of the longitudinal field depends on the numerical aperture of the focusing lens and on the shape of the lens entrance pupil [43]. A focused azimuthally polarized beam is also exploited for comparison purposes: in the focal plane it has no longitudinal field component and the transverse field is distributed in a ring-shaped pattern similar to that of the focused radially polarized beam. The collection of transverse and longitudinal fields is performed by raster scanning the focal plane of focused radially and azimuthally beams with the probe.

A quantitative estimation of the collection efficiencies and spatial resolutions in imaging both longitudinal and transverse fields is made. It is found that the roughness of the metal coating plays an important role in the coupling strength of transverse fields into the probes: the relative coupling efficiency for transverse fields diminishes with a rough metal coating, while that of longitudinal fields does not. Longitudinally polarized fields are collected with a resolution approximately 1.5 times higher as compared to transversely polarized fields and this behavior is almost independent of the roughness of the probe metal coating.

3.1 Generation of axially symmetric beams

Longitudinally and transversely polarized fields can be generated by focusing radially and azimuthally polarized beams. Their main feature is a space-variant polarization distribution with rotational symmetry around the propagation axis.

In this section the generation and far-field characterization of the axially symmetric beams used in the experiment is described. Such beams can be produced in several ways (see for example [44, 45, 46, 47, 48, 49]). In the present setup, two liquid-crystal (LC) cells are used.

3.1.1 Liquid Crystal elements

The θ-cell

The first element is the *θ-cell* polarization converter described in [50, 51, 52]. The entrance and the exit plates of the cell are linearly and circularly rubbed, respectively. The direction of the linear rubbing on the entrance plate determines the cell axis. Each LC molecule chain is characterized by a twist angle (i.e. the angle between the orientation of the molecules at the entrance and at the exit plates) that is a function of the angular position with respect to the cell axis. When the polarization-guiding conditions are met [53], a linearly polarized beam incident on the entrance plate, propagating parallel to the θ-cell normal and with electric field vector parallel or perpendicular to the cell axis [54] experiences a rotation of its polarization direction by the twist angle. This phenomenon occurs for a broad range of wavelengths. However, in this case, a defect line running along the diameter parallel to the cell axis arises. The defect line is caused by the destructive interference of two opposite field contributions of equal amplitude over the same spatial region, as illustrated in Fig. 3.1. The defect line width is mainly determined by fabrication processes. In the following, the definitions of *uncompensated* radially and *uncompensated* azimuthally polarized beams will be used to indicate the two configurations displayed in Fig. 3.1(a) and Fig. 3.1(b), respectively. Note that in this particular case, the input polarization is parallel to the θ-cell axis for the azimuthally polarized beam and perpendicular to it for the radially polarized one.

The axially symmetric beams generated by the θ-cell are focused with an objective lens (NA=0.65). The focal plane intensity distributions are imaged on a CCD by means of another microscope lens (NA=0.65). The uncompensated radial and uncompensated azimuthal configurations give rise to the same far-field pattern. As shown in Fig. 3.2, the transverse intensity distribution shows two reflection symmetries.

By placing an analyzer in front of the CCD oriented either parallel or perpendicular to the input polarization, either a four-fold or three-lobed pattern, respectively, is found.

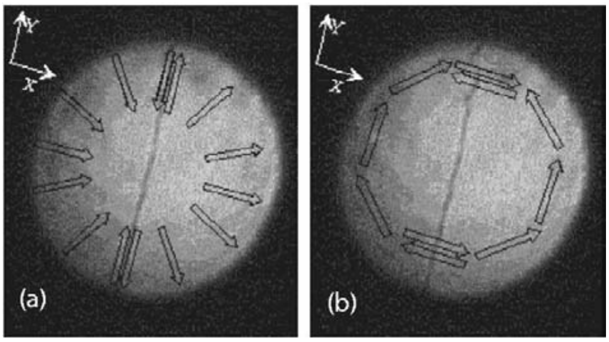

Figure 3.1: Images of the incoming laser beam after passing through the θ-*cell*, producing (a) an uncompensated radially polarized and (b) an uncompensated azimuthally polarized beam. The defect line is due to the destructive interference of the opposing polarization orientations in the two halves of the beam, as indicated schematically by the arrows.

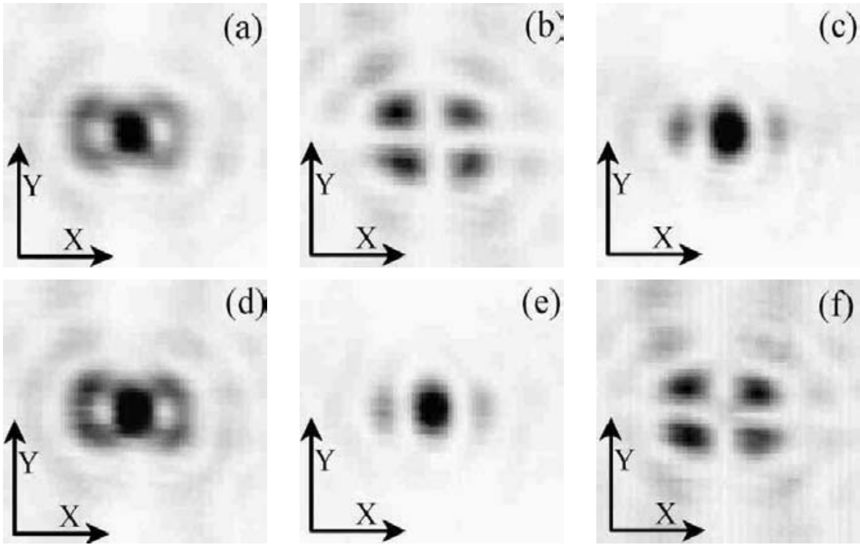

Figure 3.2: Measured focal plane images of uncompensated axially symmetric beams focused by a NA=0.65 objective. Azimuthally polarized beam: (a) total intensity, (b) intensity of the field x component, (c) intensity of the field y component. Radially polarized beam: (d) total transverse field intensity, (e) intensity of the field x component, (f) intensity of the field y component.

In conclusion, although the electric field vector lies along the radial or azimuthal directions, the θ-cell does not provide the proper phase distribution for obtaining a circularly symmetric pattern in the focal plane of the lens. For this reason, the θ-cell alone cannot be used in our setup and a second element compensating this effect is required.

The π-phase shifter

In order to have axially symmetric beams with the desired phase distribution, we use a second LC plate. It is a *phase shifter cell* providing a tunable phase delay between the two halves of the beam passing through it. It is placed in the setup as shown in Fig. 3.3.

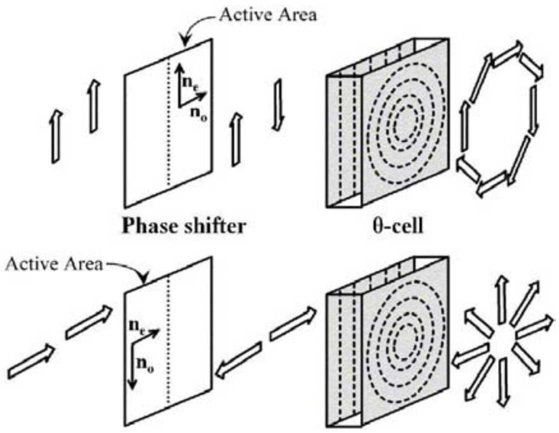

Figure 3.3: Schematic drawing of the Liquid-Crystal elements generating axially symmetric polarized beams.

This LC element is composed of two glass substrates with a rubbed polyimide alignment layer. Structured transparent ITO electrodes define an active area of 1 cm×1 cm. With a thickness of 6 μm and filled with the liquid crystal mixture BL006 the cell gives a retardation of 1772 nm at room temperature for parallel alignment. If voltage is applied, the retardation can be switched off. Since only the extraordinary index (n_e) is modulated, the input linear polarization should be aligned along this direction. As suggested in the drawing in Fig. 3.3, if a π-phase delay is applied to one half of the beam, then the output will be either a radially or an azimuthally polarized beam.

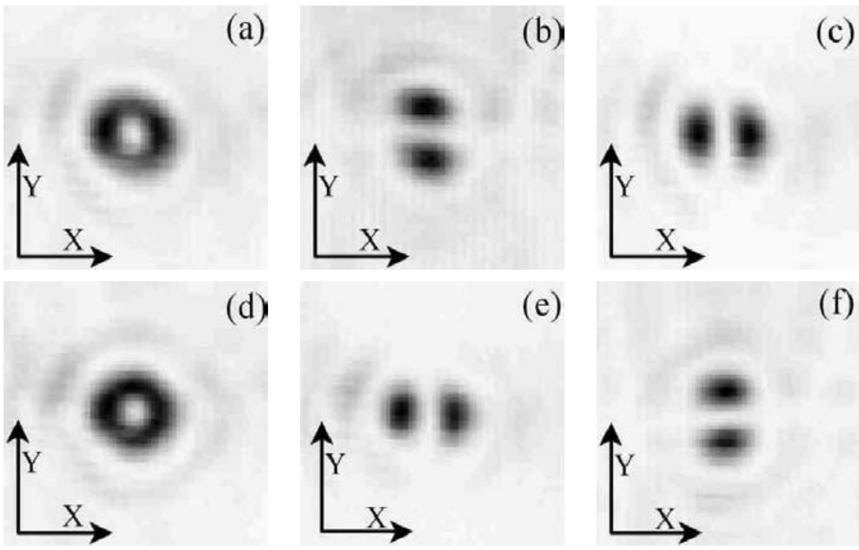

Figure 3.4: Measured focal plane images of compensated axially symmetric beams focused by a NA=0.65 objective. Azimuthally polarized beam: (a) total intensity, (b) intensity of the field x component, (c) intensity of the field y component. Radially polarized beam: (d) total transverse field intensity, (e) intensity of the field x component, (f) intensity of the field y component.

By focusing these beams, intensity distributions having complete circular symmetry are found in the focal plane (Fig. 3.4). Rotational symmetry is also expected in the polarization distribution. If an analyzer oriented along an arbitrary direction θ with respect to the cell axis is placed in front of the CCD, the observed pattern is a two-lobed intensity distribution. The orientation of the lobes follows the polarization state of the beam as shown in Fig. 3.4. In general, axially symmetric linearly polarized beams can be described by the following Jones vector [55]:

$$\mathbf{J}_P = \begin{pmatrix} \cos(P\,\theta + \phi_0) \\ \sin(P\,\theta + \phi_0) \end{pmatrix} \qquad P = 1, 2, 3, \ldots \tag{3.1}$$

In particular, the two beams produced as described above can be described by a Jones vector having $P = 1$. In the following they will be called compensated axially symmetric beams.

3.1.2 Comparison with calculations

Calculations of the optical field distribution in the focal region of a thin perfect aplanatic lens have been performed. Based on the method described in [56, 57], the implemented algorithm separately calculates each component of the **E**-field vector associated with a converging spherical wave as it propagates along the optical axis.

The following images present the results of calculations in which a NA=0.65 lens focuses a uniform field passing through an ideal θ-cell and a lens pupil. In Fig. 3.5 the case of the uncompensated beams is presented.

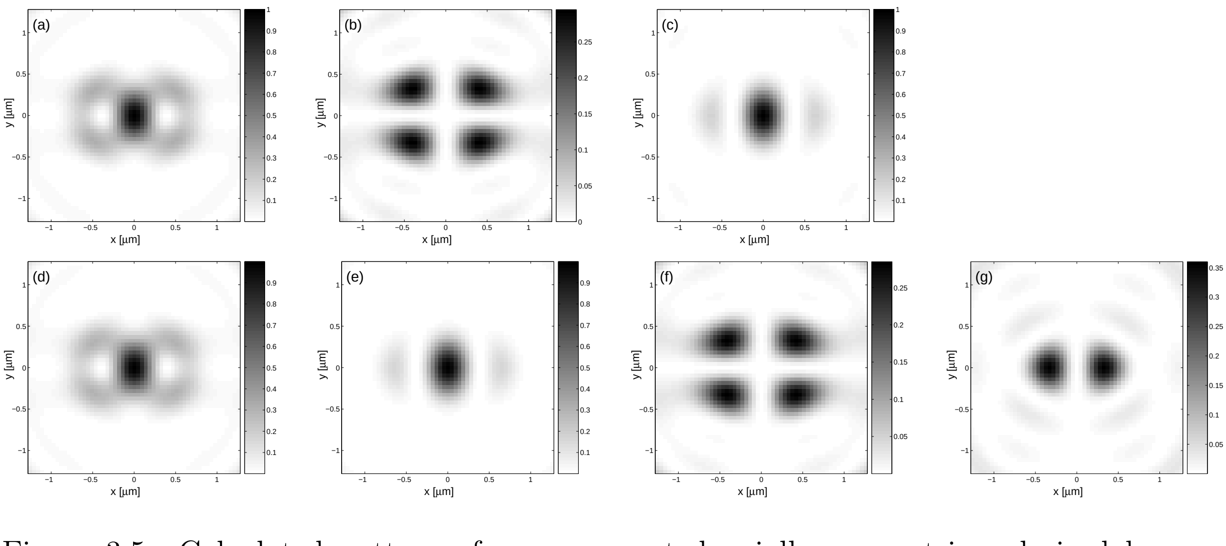

Figure 3.5: Calculated pattern of uncompensated axially symmetric polarized beams produced by an ideal θ-cell, in the focal plane of a NA=0.65 lens. Azimuthally polarized beam: (a) total intensity, (b) intensity of the field x component, (c) intensity of the field y component, (z component is zero). Radially polarized beam: (d) total transverse field intensity, (e) intensity of the field x component, (f) intensity of the field y component, (g) intensity of the field z component.

The intensity patterns are normalized to the maximum value of the total intensity as the sum of all three cartesian field components. An analogous set of calculations for the compensated cases, where a π-phase delay is introduced in one half of the beam by an ideal phase shifter plate, are shown in Fig. 3.6.

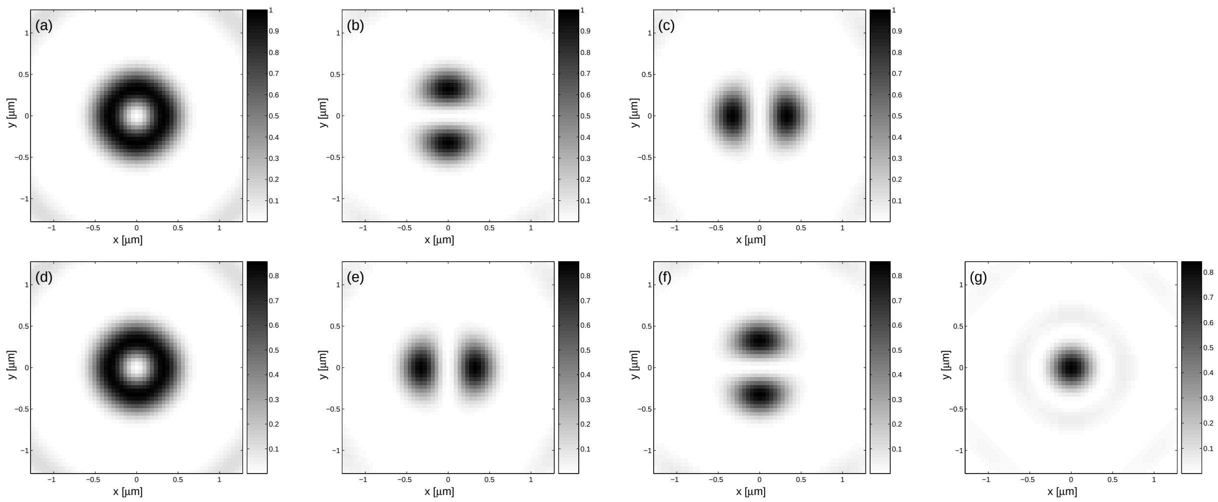

Figure 3.6: Calculated pattern of compensated axially symmetric polarized beams produced by an ideal θ-cell and focused with a NA=0.65 lens. Azimuthally polarized beam: (a) total intensity, intensity of the field x component, (c) intensity of the field y component, (z component is zero). Radially polarized beam: (d) total transverse field intensity, (e) intensity of the field x component, (f) intensity of the field y component, (g) intensity of the field z component.

Calculations demonstrate that the transverse field (given by the sum of the x and y electric field components) for the two axially symmetric beams show similar patterns. This result is also confirmed by the far-field measurements shown previously. As already stated, only a focused radially polarized beam gives rise to a non-zero field z-component. Since no significant difference is found between the collected focal plane images of focused azimuthally and radially polarized beams, it is clear that the longitudinally polarized field is strongly attenuated in the image formation process. This effect is quite well known and can be explained with simple geometrical considerations [58]. The calculated intensity patterns associated with the z-component of the field will be further employed in the following sections for comparison with near-field images collected using the SNOM probes.

3.1.3 Phase characterization of the radially polarized beam

The phase distribution of the focused radially polarized beam has been mapped with the use of a high-resolution interference microscope (HRIM) based on a Mach-Zehnder interferometer.

Experimental setup

The experimental setup used for the measurements is depicted in Fig. 3.7. A similar configuration has been used to measure phase singularities generated by sub-wavelength optical micro-structures [104], micro-lenses [60] and computer-generated holograms [61].

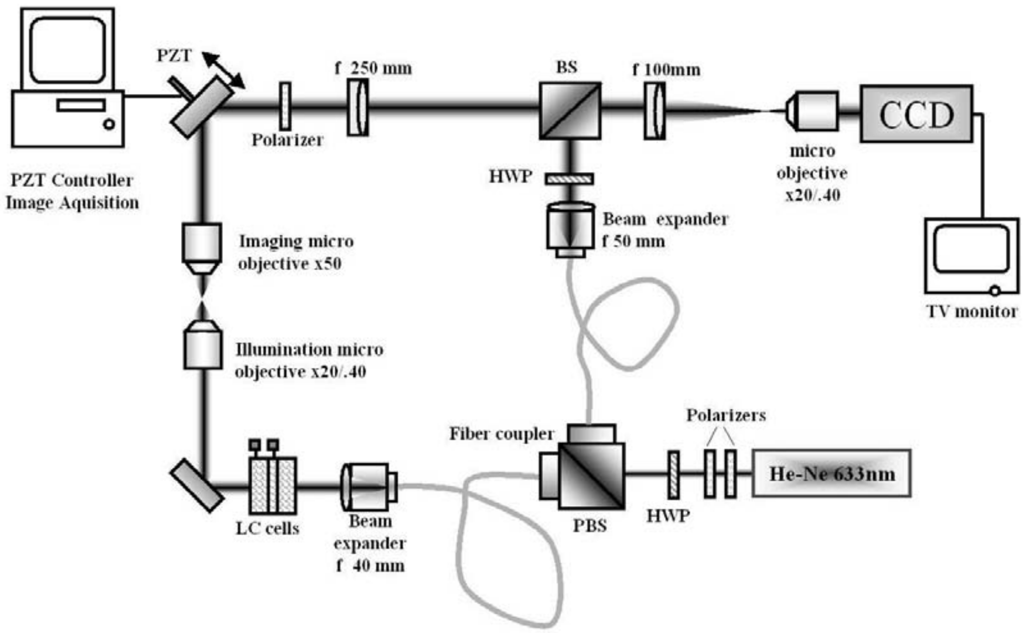

Figure 3.7: Schematic of the high-resolution interference microscope based on a Mach-Zehnder used for the phase characterization of the focused radially symmetric beam.

The light source is a linearly polarized He-Ne laser emitting at $\lambda = 633$ nm. The beam is split by a splitting group consisting of a polarizing beam-splitter (PBS) and a half-wave plate (HWP). With the employed setup, an accurate intensity balance between reference and object beam can be achieved. The (linear) polarization state of light in the two arms is kept constant by the use of polarization-maintaining fibers. Two polarizers placed in front of the HWP allow the overall beams intensity to be varied. After being expanded, the two beams are superposed by means of a standard beam-splitter: the interferogram obtained on the image plane is then recorded by a 8-bit CCD camera. With the help of a second HWP and a polarizer positioned on the reference arm it is possible to select which polarization component of the object field is phase-mapped. Two telescopic magnification stages are cascaded in order to obtain high lateral magnification. The first stage, placed on the object arm, consists of a 50× microscope objective followed by a $f = 250$ mm lens. After the superposition of the two beams, a second stage consisting of a $f = 100$ nm and a 20× microscope objective is added. With proper calibration, the estimated overall magnification is such that each CCD pixel corresponds to ≈ 33 nm in the object plane. The phase distribution is calculated with the help of a classical five-frame error-compensation algorithm [62]. By using a mirror mounted on a computer-controlled piezo (PZT) stage, 5 phase shifts, $\pi/2$ each, are introduced in the object beam. The corresponding 5 interferograms are recorded by the CCD and the calculation of the phase distribution is then carried out.

Measurements

In our case, the object field is constituted by a focused radially polarized beam generated by LC elements and collected by a 50× microscope objective. Such a beam is focused using a NA=0.4 objective as shown in Fig. 3.7.

The x component of the electric field is first considered. With the help of the polarizer, the two-lobes pattern shown in Fig. 3.8 is mapped.

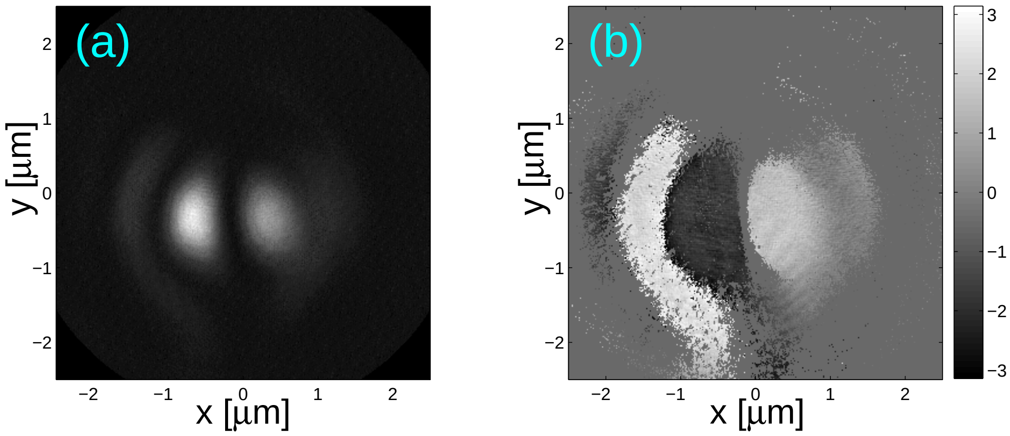

Figure 3.8: Intensity (a) and phase (b) map of the electric field x component of a focused radially polarized beam. A vertical edge singularity in the center of the pattern is found as expected.

The edge singularity [63] between two field regions having opposite phase is clearly visible. A similar measurements has been performed on the electric field y component, selected by rotating the polarizer placed on the object arm by 90°. The reference beam polarization is also rotated by 90° and set parallel to the object field polarization by using the HWP. The result is presented in Fig. 3.9.

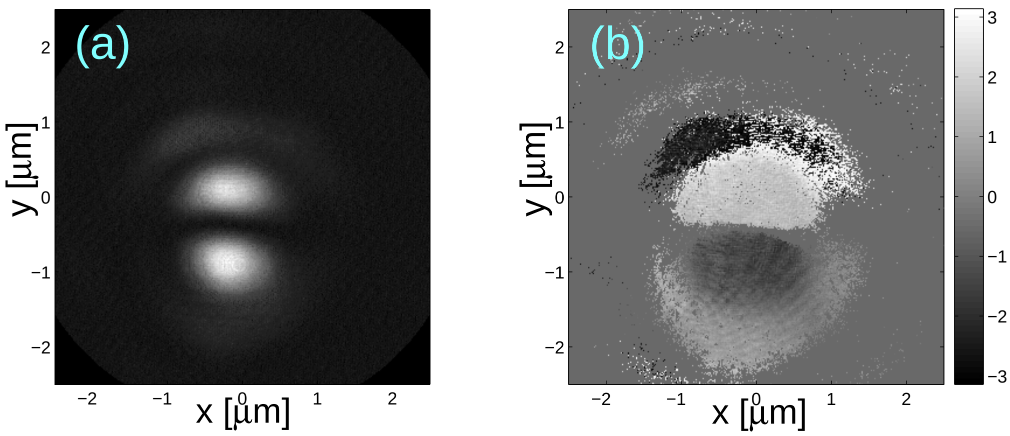

Figure 3.9: Intensity (a) and phase (b) map of the electric field y component of a focused radially polarized beam. A horizontal edge singularity in the center of the pattern is found as expected.

Since the polarization state of the object field is not uniform, it is not possible to map the phase distribution with one single measurement with the present setup. The strongest limitation comes from the linear polarization of the reference beam, allowing interference and phase retrieval with one single polarization component of the object beam at once. Nevertheless, interesting results have been obtained by making a fully radially polarized beam interfere with a linearly polarized reference beam. For this purpose, the polarizer placed along the object arm has been taken off, and the reference beam polarization oriented in the y direction. The result of this measurement is reported in Fig. 3.10.

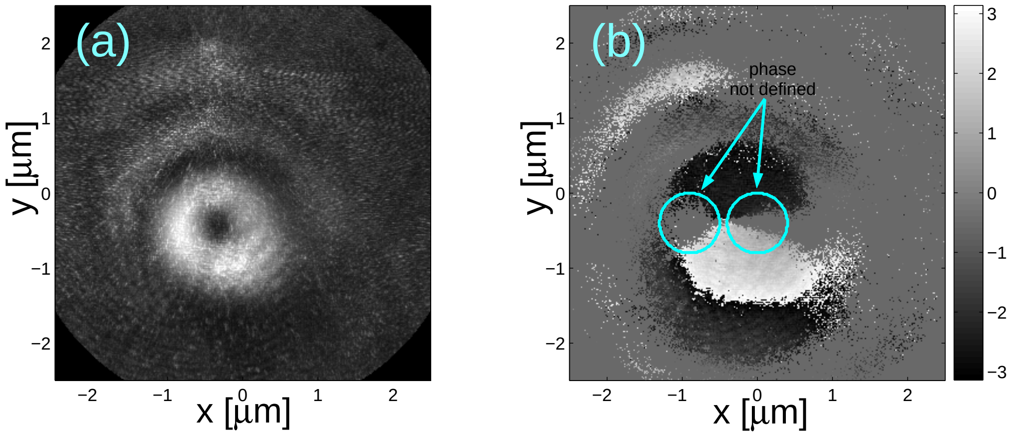

Figure 3.10: Intensity (a) and phase (b) map of the electric field of a focused radially polarized beam. The phase is not defined in those regions where the object field has polarization perpendicular to the reference beam.

The intensity distribution recalls the ring-shaped pattern that has been previously found in 3.1.1. The phase map refers only to the y component of the object field. No information about the phase of the x component of the field can be accessed: in fact, along the horizontal diameter of the radially polarized beam (where the field is fully x-polarized) the phase is not defined and an edge dislocation arises.

We conclude this section with some general remarks on axially symmetric beams. It is well known that, in the paraxial limit, the vectorial Helmoltz equation admits a family of beam-like solutions describing the transverse vectorial field with an inhomogeneous polarization state [64, 65]. Such solutions are called Bessel-Gauss modes: in particular, the two lowest-order solutions represent azimuthally and radially polarized beams. In our experiment, since the two axially symmetric beams are created by a space-variant phase modulation of an incoming TEM_{00} mode, we cannot define them as pure Bessel-Gauss modes. Nevertheless, we underline that the ultimate aim of producing such beams is to focus them in order to obtain a certain polarization-dependent field distribution suitable for our investigation.

3.2 Probe-field interaction

Once the axially symmetric beams are generated and focused, scans of the focal plane are performed using the collection-mode SNOM described in Chapter 2. A similar experiment has been conducted by Rhodes *et al.* to investigate the electromagnetic field in the focal region of a NA=0.95 lens by means of a metalized tapered fiber probe with aperture [66]. The collection properties of two different apertureless SiO_2 probes having different metal coating characteristics are presented and compared.

3.2.1 Focused axially symmetric beams mapped with standard tip

The first kind of probe employed in the experiment (called *standard* probe) is presented in Fig. 3.11.

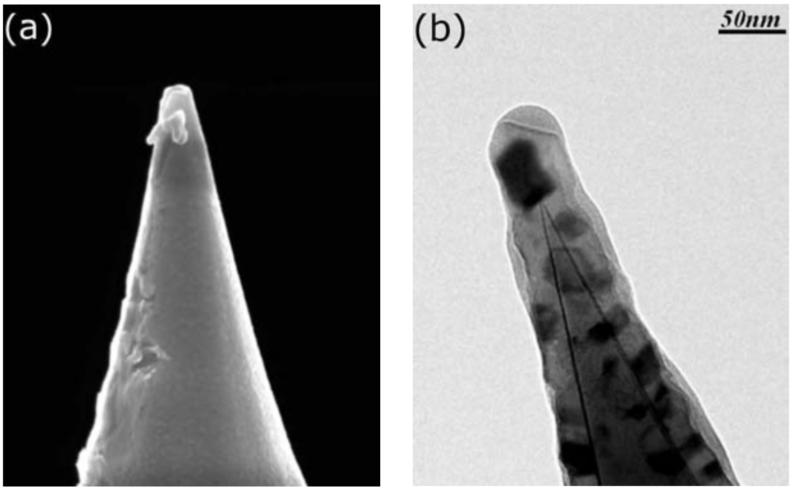

Figure 3.11: Scanning Electron Microscope (a) and Transmission Electron Microscope (b) images of a SiO_2 tip coated with aluminum in the step-coverage mode (standard probe). *TEM image courtesy of L. Aeschimann.*

The aluminum coating is deposited in the step-coverage mode [67] : i.e. a method consisting of a rotation of the wafers in the planetary wafer holders in such a way that the metal is evaporated under a constantly varying angle. By evaporating 100 nm of aluminium on the wafer, a uniform layer of about 60 nm thickness covers the tip entirely. Metal grains are formed during the deposition process, but they are contained in the coating layer. The estimated roughness of the metal layer is 1.9 nm $\pm$ 0.5 nm.

Uncompensated beams

In Fig. 3.12 the intensity distributions of focused uncompensated azimuthally and radially polarized beams as imaged by the SNOM using a standard probe are shown.

In the case of the focused uncompensated azimuthally polarized beam, the recorded image (Fig. 3.12(a)) is very similar to the calculated one, shown in Fig. 3.5(a). As expected, the tip has collected the transverse field, the only field present in the focal plane. For the focused radially polarized beam, the total field intensity distribution is given by the sum of the transverse and the longitudinal fields shown in Fig. 3.5(d) and Fig. 3.5(g) respectively. However, if the relative collection efficiency of the two fields into

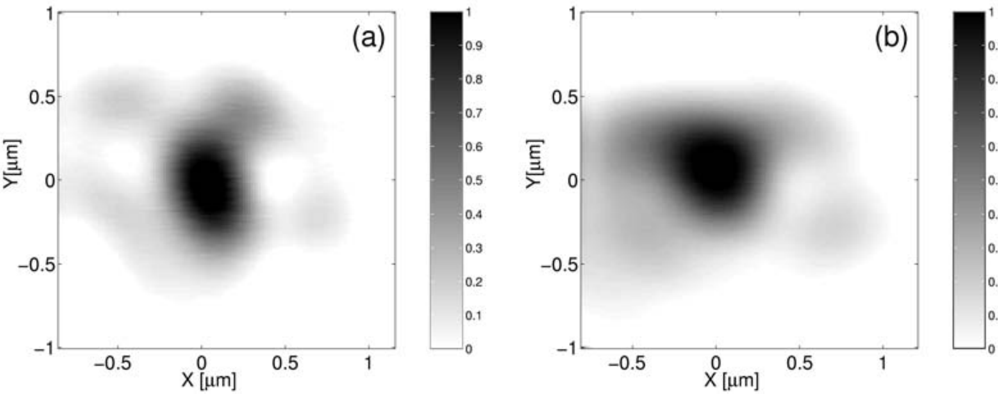

Figure 3.12: Intensity distribution of a focused uncompensated (a) azimuthally polarized beam and (b) radially polarized beam as imaged by the SNOM with a standard probe

the tip is significantly different, then the measured image would be closer to one of the two patterns. Fig. 3.12(b) clearly shows that this is the case: the detected field is more similar to the transverse field distribution than the longitudinal one. It can be noted that the central spot is a bit broader as compared to the azimuthal case, suggesting that the contribution of the two lobes of the longitudinal field are weak but present. This indicates that there is a much stronger transmission of the transverse field into the probe, but the present measurements do not permit an exact determination of the relative strength of this coupling.

Compensated beams

A better quantification of the effect observed with the uncompensated beams can be performed by mapping a more symmetrical pattern. The focused compensated azimuthally polarized beam as imaged by the SNOM system using a standard probe is shown in Fig. 3.13(a). In Fig. 3.13(b) the recorded pattern of a focused compensated radially polarized beam is shown.
The two measurements have been done in sequence, after the polarization of the input beam has been turned by 90°. The inhomogeneities in the intensity distribution are mainly due to the quality of the beam. The most important difference between the two images is in the amount of light detected in the neighborhood of the center of the annular pattern. This effect is attributed to the contribution of the longitudinal field present only in the case of the focused radially polarized beam. Therefore, a portion of the longitudinal field component must be collected by the probe. In order to investigate this coupling effect more quantitatively, the intensity profiles measured along the dashed lines of Fig. 3.13 are analyzed. Along the chosen directions, the measured distributions display the best symmetry. A comparison with calculations is then performed as follows.

The azimuthally polarized case is considered first. In this case, a focal plane field distribution whose polarization state is essentially transverse is expected. In order to take into account the finite resolving power of the probe, the theoretical profile of the transverse field $\mathcal{I}_T$ is convoluted with a gaussian-shaped function $f_T = \exp\Big[-\frac{x^2}{2\sigma_T^2}\Big]$.

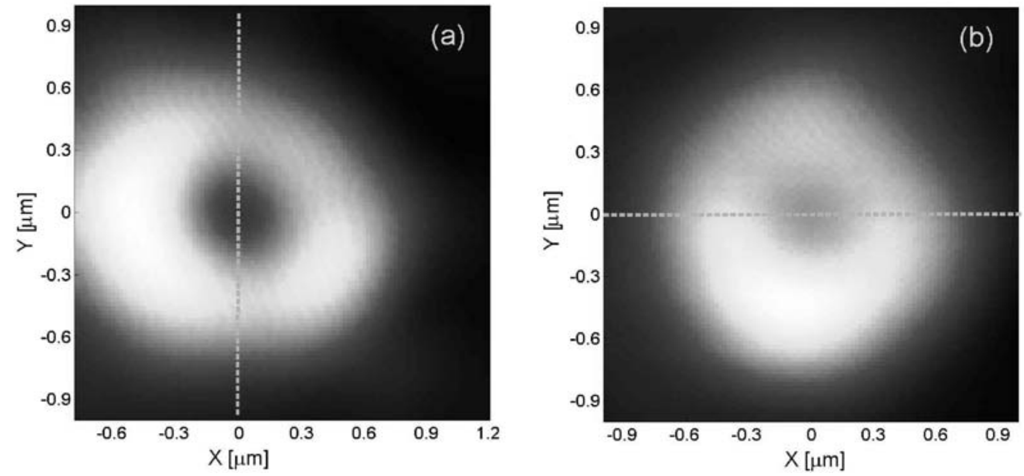

Figure 3.13: Intensity distribution of a focused compensated (a) azimuthally polarized and (b) radially polarized beam scanned by the SNOM using a standard probe.

The gaussian is taken as the instrumental function of the microscope. This procedure is commonly applied in cases where the details of the probe-field interaction cannot be modeled in an accurate way (an example is found in Ref. [68]). The parameter σ_T is determined by a Least-Squares fit of the measured data I^{azi} with the function $\mathcal{I}_T \circ f_T$. The best fit is obtained for σ_T=153 nm. In Fig. 3.14 the measured data I^{azi}, the normalized theoretical profile $\mathcal{I}_T$ and the result of the convolution $\mathcal{I}_T \circ f_T$ are shown. In the case of the radially polarized beam, since the polarization state of the pattern is not homogenous, the longitudinal and the transverse field contributions must both be taken into account, the total intensity being the sum of the two.

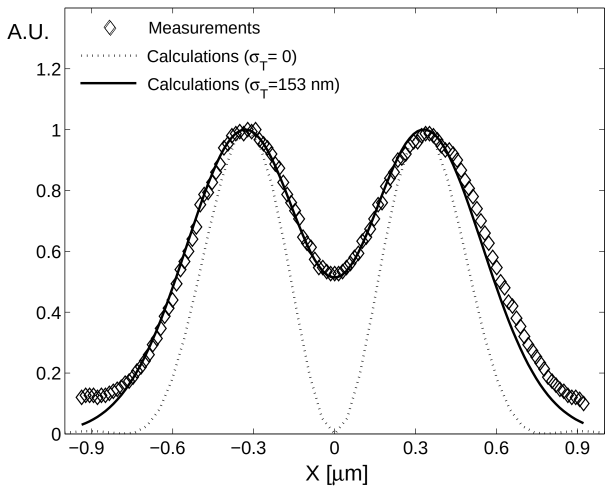

Figure 3.14: Intensity profile of a compensated focused azimuthally polarized beam. The curves show the measured data I^{azi} (diamonds), the theoretical distribution $\mathcal{I}_T$ (dotted line) and the convolution $\mathcal{I}_T \circ f_T$, with $\sigma_T = 153$ nm (solid line). The measured profile is taken along the dashed line shown in Fig. 3.13(a)

In our analysis, the following assumptions are made:

- the theoretical transverse $\mathcal{I}_T$ and longitudinal $\mathcal{I}_L$ components are individually convoluted with two different gaussian functions, $f_T = \exp\left[-\frac{x^2}{2\sigma_T^2}\right]$ and $f_L = \exp\left[-\frac{x^2}{2\sigma_L^2}\right]$ respectively

- the detected total intensity is given by a weighted sum of the longitudinal and transverse field contributions $I^{rad} = I_T^{rad} + C \cdot I_L^{rad}$. The value of C gives an indication on the ratio of the probe collection efficiency for longitudinally polarized fields to that one for transversely polarized fields.

Furthermore, since in this particular case the images of the focused azimuthally and radially polarized beams are collected using the same probe, we assume that the collection behavior of the tip with respect to the transverse component of the field is the same in both measurements. Thus, we apply the same value of σ_T in both the radial and azimuthal cases. A two-parameter Least-Squares fit of data with the function $\mathcal{I}_T \circ f_T + C \cdot (\mathcal{I}_L \circ f_L)$ is performed, searching for the best values of σ_L and C. The results are reported in Fig. 3.15, where the measured points I^{rad}, the theoretical profile$\mathcal{I}_T + \mathcal{I}_L$ and the weighted sum of the convoluted profiles $\mathcal{I}_T \circ f_T + C \cdot (\mathcal{I}_L \circ f_L)$ are shown.

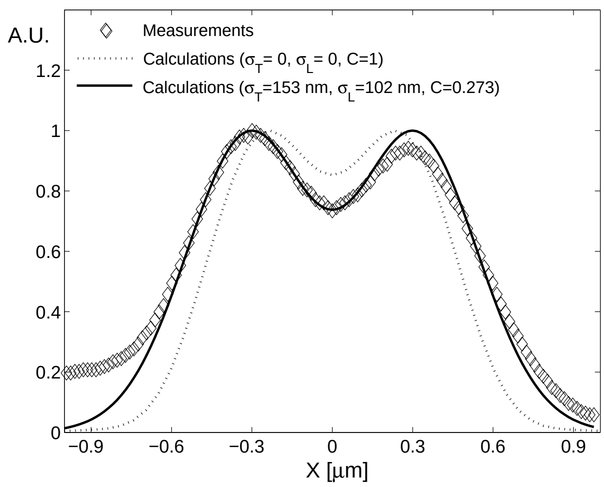

Figure 3.15: Intensity profile of a compensated focused radially polarized beam. The curves show the measured data (diamonds), the theoretical distribution $\mathcal{I}_T + \mathcal{I}_L$ (dotted line) and the weighted sum of the convoluted distributions $\mathcal{I}_T \circ f_T + C \cdot (\mathcal{I}_L \circ f_L)$ with $C = 0.273$ (solid line). The measured profile is taken along the dashed line shown in Fig. 3.13(b).

The optimal values are $\sigma_L = 102$ nm and $C = 27.3\%$. We note that the RMS of the microscope instrument functions for the two field orientations are significantly different, with the transverse gaussian f_T ($\sigma_T = 153$ nm) being significantly broader than the longitudinal gaussian f_L ($\sigma_L = 102$ nm).

3.2.2 Focused axially symmetric beams mapped with rough tip

The second kind of probe used in the experiment is coated using a different process. In this case, the aluminium has been deposited in the normal mode: the wafers are not rotated during the evaporation procedure, so the metal is deposited normally to the wafer surface. The result is a chaotic distribution of small metal grains and a much higher roughness (5.5 nm ± 0.5 nm) than in the case of a standard probe. This kind of probe will be called *rough* probe in the following (Fig. 3.16).

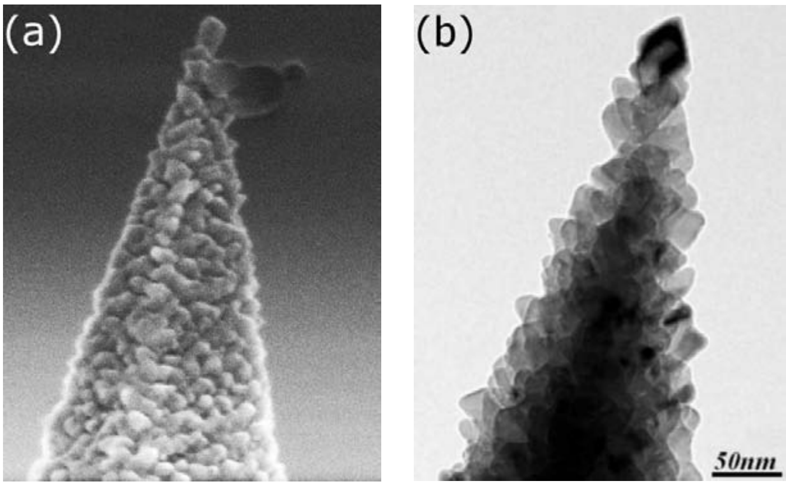

Figure 3.16: Scanning Electron Microscope (a) and Transmission Electron Microscope (b) images of the apex of a SiO_2 tip coated with aluminum in the normal mode (rough probe). *TEM image courtesy of L. Aeschimann*

Uncompensated beams

In Fig. 3.17(a) the image of the focused azimuthally polarized beam is shown.

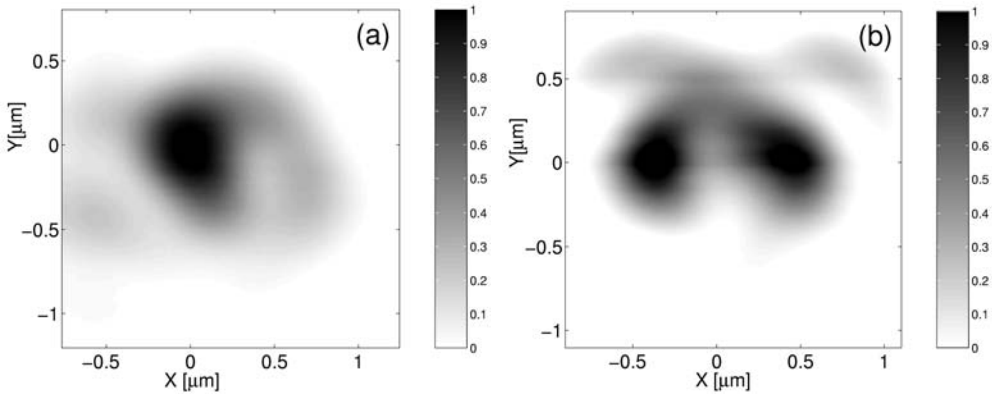

Figure 3.17: Intensity distribution of focused uncompensated (a) azimuthally polarized beam and (b) radially polarized beam as imaged by the SNOM with a rough probe

In this case the field is purely transverse and the recorded pattern is similar to the one obtained with a standard probe. The image of the focused radially polarized beam is depicted in Fig. 3.17(b). This pattern is clearly not similar to either the transverse field intensity of Fig. 3.5(b) or the total field intensity given by the sum of the patterns in Fig. 3.5(d) and Fig. 3.5(g). Rather, the detected image is most similar to the intensity distribution of the longitudinal component only. By comparing the dimensions and the positions of the lobes in the measured image with the calculations, it is possible to conclude that the rough probe has mainly transmitted the longitudinally oriented component of the field while the transverse component has been blocked.

Compensated beams

We consider again the focused compensated azimuthally polarized beam. The detected image is shown in Fig. 3.18(a), and shows a pattern similar to the calculated one. The intensity distribution of the radially polarized beam, shown in Fig. 3.18(b), is then considered. As expected from the previous experience, the longitudinal component of the field has been coupled and a single spot rather than a ring-shaped pattern is found.

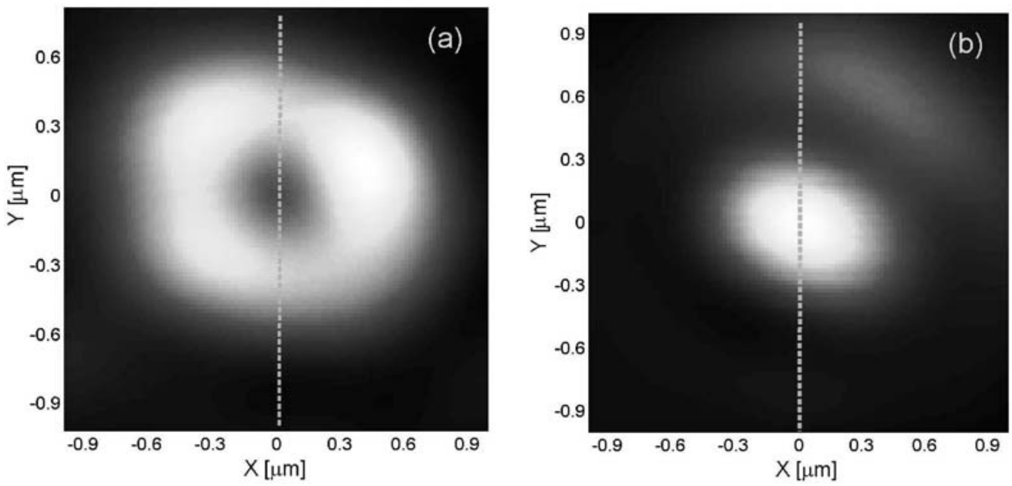

Figure 3.18: Intensity distribution of a focused compensated (a) azimuthally polarized and (b) radially polarized beam as imaged by the SNOM using a rough probe.

By taking the intensity cross section along the dashed lines in Fig. 3.18, we obtain the profiles shown in Fig. 3.19 and Fig. 3.20.

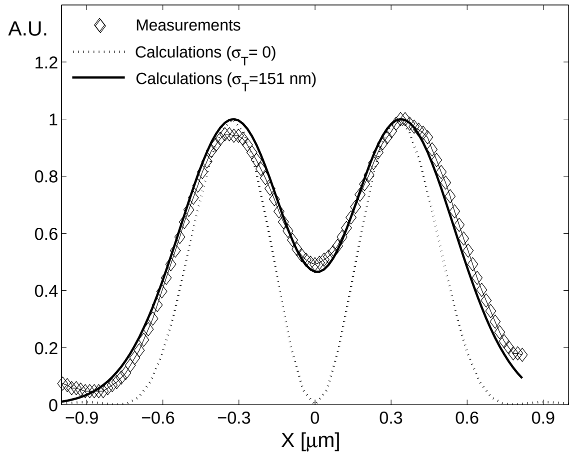

Figure 3.19: Intensity profile of a compensated focused azimuthally polarized beam. The curves show the measured data I^{rad} (diamonds), the theoretical distribution $\mathcal{I}_T$ (dotted line) and the convolution $\mathcal{I}_T \circ f_T$, with $\sigma_T = 151$ nm (solid line). The measured profile is taken along the dashed line shown in Fig. 3.18(a).

In the azimuthal case a convolution with a gaussian function f_T having σ_T as a free parameter is performed. The best fit is given by $\sigma_T = 151$ nm, a value very close to the one obtained for the standard probe. This indicates that the behavior of the two kinds of probe in collecting transverse fields is almost the same.

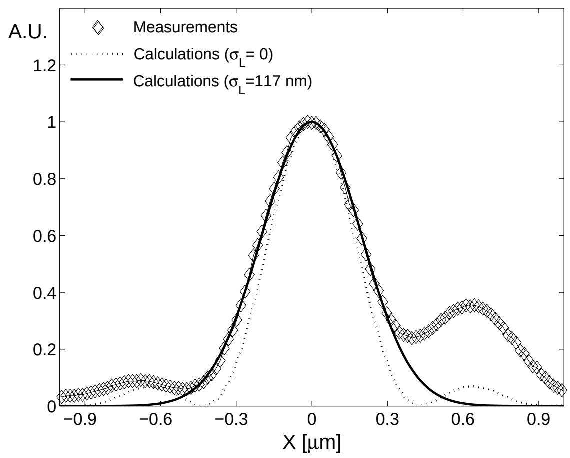

Figure 3.20: Intensity profile of a compensated focused radially polarized beam. The curves show the measured data I^{rad} (diamonds), the theoretical distribution $\mathcal{I}_L$ (dotted line) and the convolution $\mathcal{I}_L \circ f_L$, with $\sigma_L = 117$ nm (solid line). The measured profile is taken along the dashed line shown in Fig. 3.18(b).

In the radial case, for comparison purposes, we assume that only the longitudinal component has been collected by the probe. Consequently, the theoretical profile $\mathcal{I}_L$ of the longitudinal field distribution is only convoluted with an instrument gaussian function f_L characterized by a σ_L to be determined by fitting the experimental data I^{rad}. The results of the fitting processes gives $\sigma_L = 117$ nm. Once again we find a narrower probe instrument function for the collection of longitudinal fields versus transverse fields.

3.3 Discussion of results and conclusions

The Near-field Optical Microscope is nowadays one of the most promising tools for the investigation of the interaction of light with objects on a nanometric scale. It is known that, in such a situation, the description of optical fields in the paraxial approximation is clearly unsatisfactory and the electromagnetic field must be considered in its whole vectorial nature. As a consequence, an understanding of the probe response with respect to the three-dimensional electromagnetic field becomes crucial. By considering the conical shape of the SNOM probe, we identify two main polarization states that are of some interest to this end: parallel (longitudinal polarization) and perpendicular (transverse polarization) to the probe axis. In this chapter there are presented an experimental determination of the relative collection efficiency and the relative spatial resolution that are obtained when these two fields are scanned and imaged by means of apertureless microfabricated quartz probes.

As the measurements performed with the rough probe demonstrate, we found that the value of $C = 27.3\%$ obtained for the standard probe is dramatically changed by altering the roughness of the metal coating. This effect can be explained by taking into consideration the light guiding mechanism in the microfabricated probes as described in Ref. [39]. In that work it was suggested that the coupling of transversely polarized light would take place at the probe sidewalls, as guided linearly polarized modes reach cutoff in the taper well before arriving at the probe apex. In the rough probe, the roughness of the metal-coated sidewalls would then play a significant role in impeding the coupling of transversely polarized fields, resulting in a change of the collection efficiency ratio.

Another important collection property of microfabricated apertureless probes is the polarization-dependent resolving power. The gaussian instrumental function used in the data fits is in principle related to the whole microscope system. Nevertheless, even if its value cannot be strictly considered as a direct estimation of the spatial resolution of the probe, comparisons between different measurements performed with the same system can indeed be used to describe relative resolution performances. With the standard probe, we found a larger value of σ_T as compared to σ_L, and this trend is also found with the rough probe, where the values of σ_T and σ_L are very close to the standard probe case.

The previous results can be summarized in the following three points: (1) the probe metal coating roughness can dramatically affect the collection efficiency of transversely polarized fields, but (2) has only slight influence on the resolution with which the two field orientations are imaged; (3) longitudinally polarized fields are imaged with a higher resolution with respect to the transversely polarized fields. It is also interesting to note that although the two kinds of probe used in the experiment clearly show different morphological characteristics, both of them possess a large metal grain (diameter $\sim$40 nm) at the apex of the tip. This observation,together with the results found in our experiment, suggests that this large grain could be primarily responsible for the collection of longitudinally polarized fields, which would be consequently coupled at the very probe apex.

Chapter 4

Emission properties of apertureless microfabricated probes

Well-established operation modes of Near-field Optical Scanning Microscope (SNOM) rely on the generation of local nano-sources at the end of narrow probes brought in proximity of the sample to illuminate. There are basically two kinds of probes that can be employed for this purpose: metallic STM (or AFM) or metalized dielectric probes. Confined fields can be created by properly illuminating metallic probes with an external beam [69], or by opening a nano-aperture at the apex of a metal-coated tapered fiber [21]. Another possibility was suggested in 1999 by Keilmann, who proposed the use of Surface Plasmon Polaritons modes (SPP) coupled on a fully metal-coated dielectric probe [70] and excited by the radially polarized TM_{01} mode guided in the probe. Moreover, in a recently published work it has been pointed out that the TM_{01} mode can produce an enhanced field confined at the apex of microfabricated fully Aluminum-coated SNOM probes even at optical frequencies far from the metal plasma resonance [71]. On the other hand, Novotny *et al.* underlined the importance of coupling the HE_{11} mode into a fully metal-coated probe for the improvement of power throughput at its apex [72]. The necessity of operating a selection of guided modes into the probe constitutes, then, a crucial issue.

In the present work, the problem of mode selection into microfabricated fully aluminum-coated quartz probes [32] is considered. We choose to focus our attention on the HE_{11} and the TM_{01} guided modes and study the possibility of selectively control the coupling into the probe by operating on the injection conditions. With the help of a Mach-Zehnder interferometer implemented on an optical microscope, far-field patterns emitted by the probe after controlled injection are characterized in intensity and phase. By comparing measurements with calculations based on a simplified numerical model of the very end part of the tip, we find that the far-field characterization of the emitted patterns reveal the type of mode coupled into the probe. In addition, near-field scans (performed with a collection-mode SNOM in a tip-on-tip configuration [73]) show that a localized longitudinally polarized spot is produced at the probe apex when a TM_{01} is coupled into the probe.

4.1 3D computational model

A realistic study of light propagation into microfabricated fully Aluminum-coated quartz probes involves a rigorous solution of three-dimensional Maxwell's equations. The complexity of the boundary conditions imposed by the tip geometry suggests the use of numerical methods for this purpose, even if analytical solutions can also be employed in some particular cases [74]. The computational investigations reported in this work have been conducted with the help of a commercial software (Microwave Studio, CST, Darmstadt, Germany) based on the Finite Integration technique.

In order to carry out an accurate analysis of the interaction of the electromagnetic field with the considered SNOM probes, the calculation domain must be discretized in mesh cells having linear dimensions of almost few tens of nanometers. This requirement is very large-memory demanding, and makes the calculation of the whole structure impractical if not impossible at the moment. Following previously published works [71, 72], we choose to take into consideration only the very end part of the probe. The calculation domain is a 3D rectangular air box having dimensions 1 μm$\times$1 μm$\times$1.7 μm.

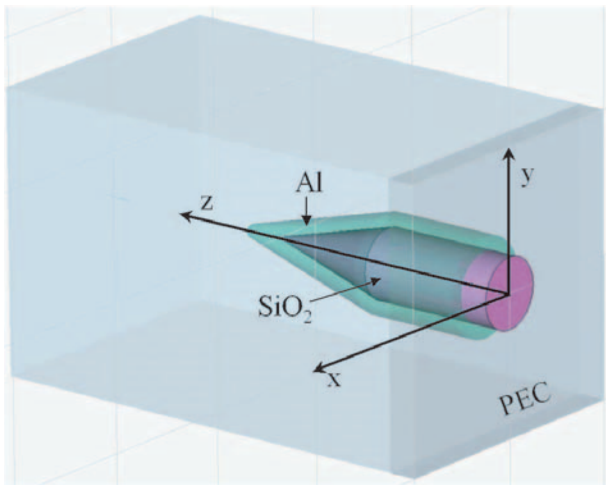

Figure 4.1: Three dimensional model of the fully-coated quartz SNOM probe. The apex angle of the tip is 34^o, the Aluminum coating thickness is 60 nm and the cylindrical waveguide has a cross-sectional diameter of 250 nm. The dimensions of the calculation domain are 1μm$\times$1μm$\times$1.7 μm. The PEC plate surrounding the entrance waveguide is also visible.

As shown in Fig. 4.1, the probe is composed by two parts: a tapered region and a cylindrical waveguide serving as input port. The taper is constituted by a quartz cone characterized by an apex angle of 34^o. The quartz cone is coated with an Aluminum layer having a constant thickness of 60 nm. Because of the tip geometry, the metal thickness at the very apex results slightly larger, as it happens in the real case. The apex of the probe is represented by a metallic hemisphere of 30 nm radius. The cylindrical waveguide region is 500 nm long and is constituted by a quartz core of a 250 nm diameter, coated with an Aluminum layer, 60 nm thick. The core lateral size allows the cylindrical HE_{11} and TM_{01} modes be guided to the taper [75]. The waveguide quartz core is surrounded, at its very beginning, by a plate made of a Perfectly Electric Conducting (PEC) material, 100 nm thick. In this region, the waveguide behaves like a loss-free ideal metallic waveguide.

The electromagnetic field distribution in the near-field of the tip apex is mainly determined by the guiding properties of the metal-coated taper. Within this structure it is not possible to describe the field propagation in term of guided modes in a strict sense. Nevertheless, Hecht *et al.* [76] pointed out that it can still be possible to interpret the taper as a metallic cylindrical waveguide having a gradually decreasing diameter acting like a smooth filter for bulk and surface modes. With this assumption, we numerically calculate the spatial distribution of the eigenmodes supported at the entrance of the cylindrical waveguide and propagate them through the modeled probe. The presence of PEC plate allows us to consider modes that are neither TE nor TM polarized [77] and whose analytical expressions are known [78]. Because of the critical lateral dimensions of the waveguide, only few low-order modes can reach the tapered region, thus contributing in a non-negligible way to the emitted field close to the probe apex. In the following, we focus our attention on the TE_{11} and TM_{01} modes at the optical frequency $\omega = 3.543 \cdot 10^{15}$ s^{-1} ($\lambda = 532$ nm).

4.1.1 TE_{11} mode

Among all the supported modes, the TE_{11} is particularly important to study because it reaches the cut-off condition at the smallest waveguide diameter, thus presenting the highest transmission coefficient. Numerical calculations show that the fundamental modes supported by the waveguide are represented by two TE_{11} modes having orthogonal polarizations. For both modes, the polarization is not homogeneous and both transverse components of the field $E_{x,y}$ are non-zero. In the following we will refer to TE^x_{11} as the TE_{11} mode with polarization mainly oriented along the x direction. In Fig. 4.2 the real part of the electric field components E_x and E_y associated to the TE^x_{11} mode in the quartz core of the waveguide are shown.

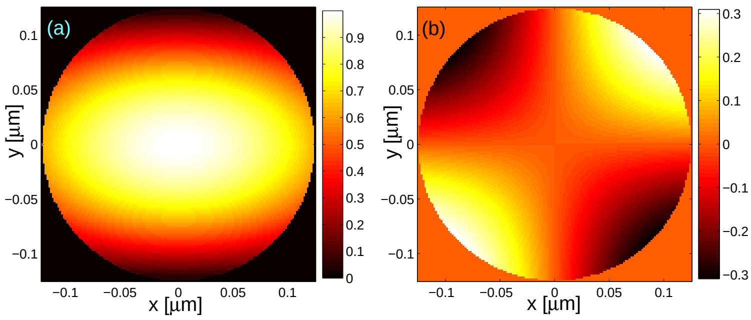

Figure 4.2: Real part of the normalized electric field associated to a TE^x_{11} mode at the entrance of the loss-free metallic waveguide: (a) $\mathrm{Re}\{E_x\}$ and (b) $\mathrm{Re}\{E_y\}$

Field distributions are normalized to the maximum value of the total electric field amplitude $max\{\sqrt{|E_x(x,y)|^2 + |E_y(x,y)|^2}\}$. During propagation through the structure, the electric field does not maintain a transverse polarization: the initial TE^x_{11} transforms into an hybrid HE^x_{11} mode because of the taper geometry and the real lossy metallic coating.

A detailed description of the energy transfer involved in this transition is difficult to carry out as the definition of a HE_{11}^{x} mode in a tapered structure is ambiguous.

As shown in Fig. 4.3, when the cutoff diameter is reached, the mode starts to decay exponentially, allowing a very small amount of light to reach the tip apex.

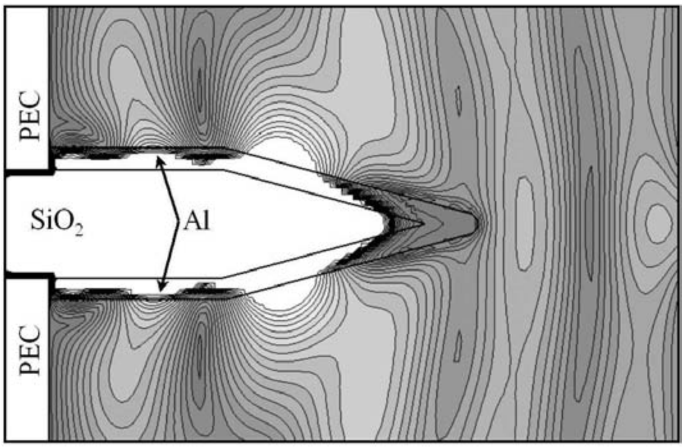

Figure 4.3: TE_{11}^{x} electric field amplitude distribution in the yz plane of the calculation domain. The linear color scale reaches saturation (white color) in the probe core and in the metallic cladding.

In fact, at cutoff, energy is mainly absorbed by the Aluminum coating or radiated outside the taper through the metallic sidewalls.

This behavior has important consequences on the probe emission characteristics in the near-field. Since the polarization of the HE_{11}^{x} mode is not circularly symmetric, polarization-dependent near-field patterns are expected to be found.

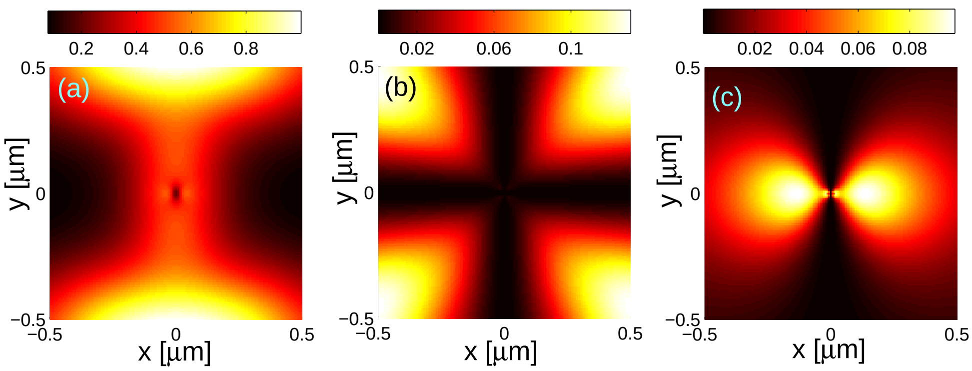

Figure 4.4: Tip emission of the HE_{11}^{x} mode: normalized squared amplitude distributions of the electric field cartesian components in a transverse plane at 10 nm from the tip apex. (a) $|E_x|^2$, (b) $|E_y|^2$ and (c) $|E_z|^2$

In particular, in a transverse plane at 10 nm from the tip apex, the calculated electric field components have the three different distributions shown in Fig. 4.4. As usual, the plot are normalized to the maximum value of the total electric field amplitude $max\{\sqrt{|E_x(x,y)|^2 + |E_y(x,y)|^2 + |E_z(x,y)|^2}\}$. We observe that the emitted field is mainly

x-polarized and distributed in two lobes oriented orthogonally to the field polarization direction (Fig. 4.4(a)). The E_y and E_z components are sensibly weaker. The four-lobed distribution of the E_y component is due to the y-component of the electric field of the guided mode, while the two peaks (x- oriented) of the longitudinal field are generated by a known depolarization effect [23]. A similar, but much stronger depolarization effect is also reported in aperture SNOM probes [79].

In a plane placed at a distance of 250 nm from the tip apex, the calculated field distribution starts to become comparable to the far-field pattern. In Fig. 4.5 squared amplitudes and phases of the three cartesian components of the electric field are shown.

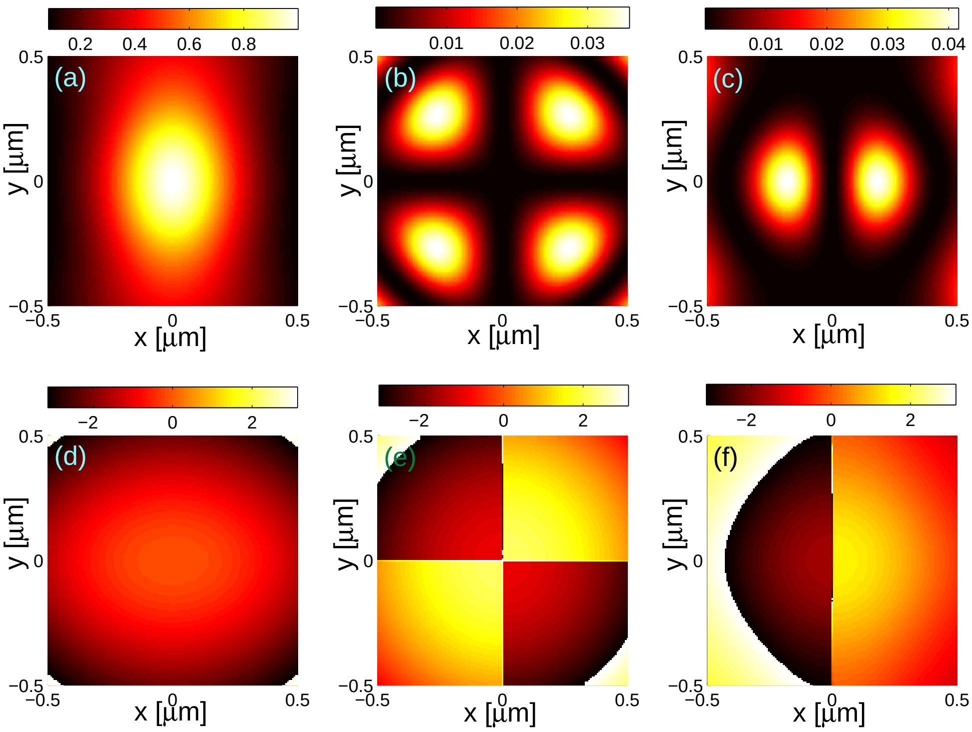

Figure 4.5: Tip emission of the HE_{11}^{x} mode in a transverse plane 250 nm from the tip apex: (a,b,c) amplitude and (d,e,f) phase distributions of the E_x, E_y and E_z electric field components respectively.

As it happens in the near-field region, the electric field is mainly oriented in the x direction, but distributed in an ellipsoidal region $\sim$ 440 nm $\times$ 500 nm (Fig. 4.5(a)). The phase map reported in Fig. 4.5(d) shows a parabolic profile indicating a curvature of the wavefront: because of the large divergence of the emitted field, the wavefront appears particularly curved as the observation plane is very close to the probe apex. Superposed to the spot we find two weaker patterns: a four-lobed distribution linearly y-polarized (Fig. 4.5(b)) and a two-lobed distribution with longitudinal polarization (Fig. 4.5(c)). The phase associated to these two last field components is particularly interesting because of the presence of defect lines (Figs. 4.5(e) and 4.5(f)). Since only the transverse field contributes to the radiative energy flow in the z-direction, the longitudinal field is expected to vanish as soon as the observation plane is moved away from the near-field region.

4.1.2 TM_{01} mode

The second mode we considered is the radially polarized TM_{01} mode. The eigenmode calculated at the entrance of the loss-free cylindrical metallic waveguide is characterized by the electric field distribution reported in Fig. 4.6.

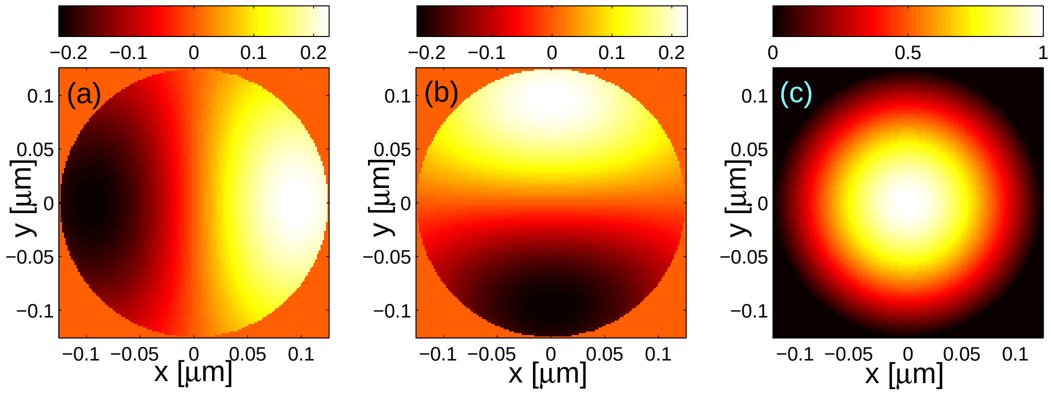

Figure 4.6: Real part of the normalized electric field associated to a TM_{01} mode at the entrance of the loss-free metallic waveguide: (a) $\mathrm{Re}\{E_x\}$, (b) $\mathrm{Re}\{E_y\}$ and (c) $\mathrm{Re}\{E_z\}$.

Analytical solutions of the Maxwell's equations in loss-free metallic cylindrical waveguide show that the TM_{01} mode has a larger cut-off diameter with respect to the TE_{11} mode. Nevertheless, although the TM_{01} mode experiences a stronger attenuation at the very end of the taper, it provides an important field enhancement at the tip apex (Fig. 4.7).

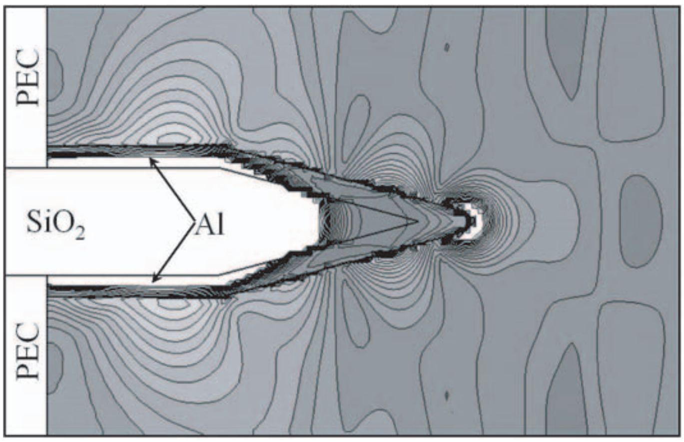

Figure 4.7: TM_{01}^x electric field amplitude distribution in the yz plane of the calculation domain. The linear color scale saturates in the probe core, in the metal cladding and at the very tip apex. Along the taper, surface modes at the metal-air interface are visible.

Bouhelier *et al.* explained the generation of enhanced fields at the apex of a tapered fiber probe as a phase-matching effect of surface modes at the metal-air interface with guided modes in the waveguide [80]. Guided radially polarized mode allows a particularly efficient achievement of this condition: in Fig. 4.7 the surface waves excited by the guided TM_{01} mode and propagating along the taper are visible. Surface modes excited at the metallic sidewalls interfere constructively at the tip apex and a localized spot is generated.

In a transverse plane placed at 10 nm from the apex, it is possible to observe a weak ring constituted by two two-lobed transversely polarized patterns (Fig. 4.8(a,b)) surrounding the z-polarized hot-spot. The lateral extension of the longitudinal enhanced field is ~ 40 nm (Fig. 4.8(c)).

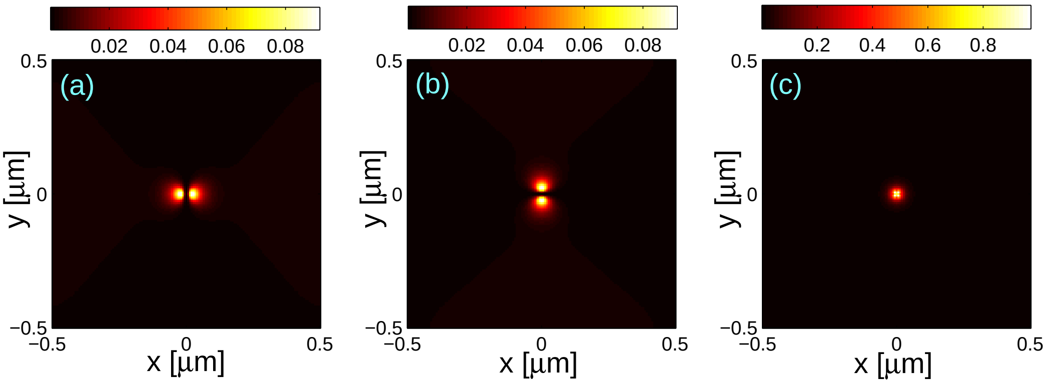

Figure 4.8: Tip emission of the TM_{01}^{x} mode: normalized squared amplitude distributions of the electric field cartesian components in a transverse plane at 10 nm from the tip apex. (a) $|E_x|^2$, (b) $|E_y|^2$ and (c) $|E_z|^2$.

The possibility of using an ultra-small spot at the apex of a metalized transparent probe opens attractive perspectives in illumination-mode near-field microscopy. The knowledge of the distribution of electromagnetic energy as it radiates from the apex becomes, therefore, an important topic to investigate. In a plane placed at a distance of 250 nm from the tip apex, the electric field is distributed as shown in Fig. 4.9. We remark that the relative amplitude of the transverse field components E_x and E_y has been increased to the detriment of the longitudinally polarized E_z, that spreads over a larger area. Similarly to the HE_{11}^{x} case previously described, the longitudinal field vanishes completely in the far-field region of the probe, the energy flow in the z direction being dependent on the transverse electric and magnetic fields only. As a consequence, the far-field emitted by fully metal-coated probes guiding a TM_{01} mode will be constituted by a radially polarized annular pattern. The phase of such a field can only be referred to a single radial component at once. For example, we present the phase map of the E_x and E_y components in Fig. 4.9(a,b), showing the π-step lines perpendicular to the electric field orientation and the lobes position.

We numerically showed that the emitted far-field patterns are characterized by phase distributions strongly linked to the phase of the E_x and E_y components of the corresponding guided modes. This particular feature represents the interpretation key we will use in the following for the understanding of the mode coupling mechanism into the considered probes.

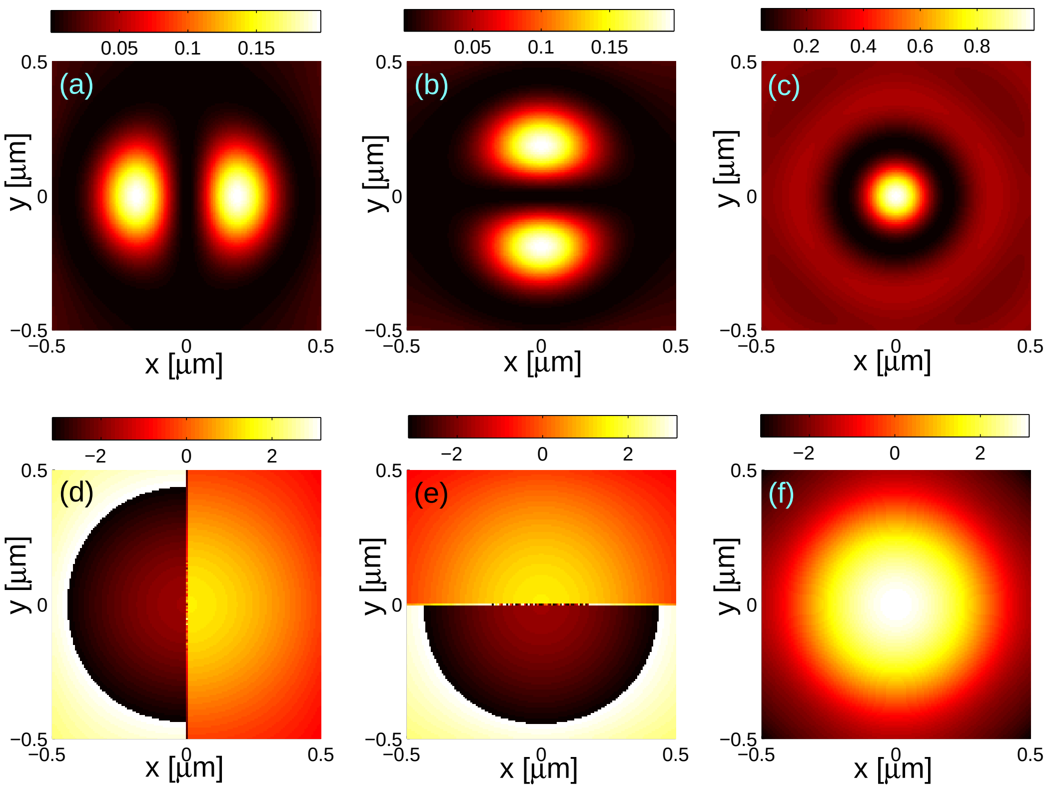

Figure 4.9: Tip emission of the TM^x_{01} mode in a transverse plane at 250 nm from the tip apex: (a,b,c) amplitude and phase (d,e,f) distributions of the E_x, E_y and E_z electric field components respectively.

4.2 Interferometric microscope measurements

A first characterization of fully metal-coated quartz probes is conducted with the help of a Mach-Zehnder interferometer mounted on a high-magnification optical microscope. The phase information contained in the emitted patterns gives us a direct insight on the coupling mechanism between the optical field injected into the probe and the modes excited in the structure. In this section we will show that HE_{11} and TM_{01} modes can be selectively coupled into the probe by injecting focused beam having suitable polarization states.

4.2.1 Experimental setup

High Resolution Interference Microscope

The device we use for the phase characterization of optical fields emitted by apertureless probe is depicted in Fig. 4.10. Its working mechanism has been already described in section 3.1.3. A sample holder hosting the silicon chip with the cantilevered probes has been added to the setup. The laser beam ($\lambda = 633\ nm$) is injected into the probe from the back side hole by means of a NA=0.4 microscope objective mounted on a xyz translation stage.

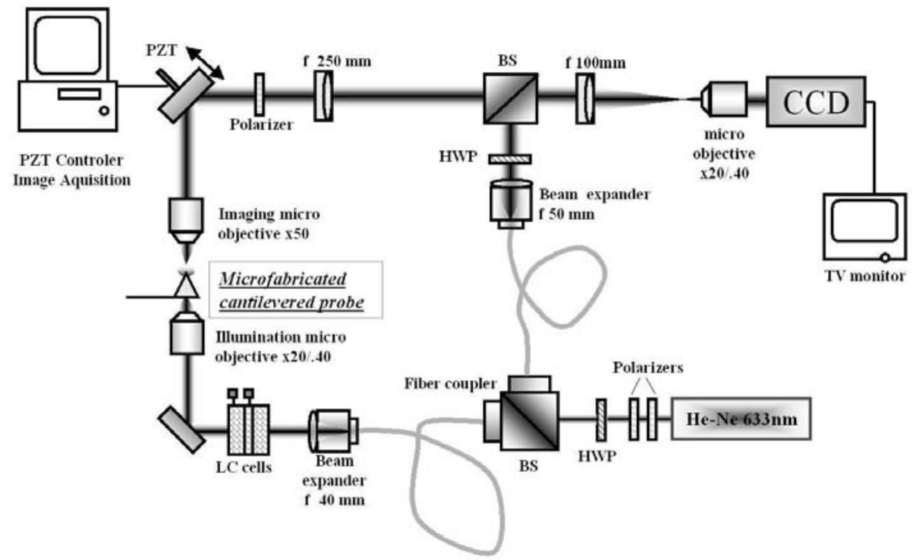

Figure 4.10: Schematic of the high-resolution interference microscope based on a Mach-Zehnder used for the phase characterization of optical field emitted by apertureless probes.

Liquid Crystal elements

In section 3.1.3 we demonstrated that axially symmetric beams can be generated with the help of suitable Liquid Crystal plates. In this experiment we employed the same device concept upgraded with a new feature. In fact, a third LC element, the *polarization rotator* cell, is introduced between the π-phase shifter and the θ-cell.

If a potential (10 V at $\nu = 1$ KHz) is applied to the *polarization rotator* cell, then the polarization state of the outgoing light is unchanged, but if no voltage is applied, the cell behaves like a $\lambda/2$ plate rotating the polarization by 90°. With this arrangement, it is possible to electrically switch between azimuthally and radially polarized output beams without moving any optical elements. The risk of malicious misalignments in the optical setup are, therefore, avoided. All the three LC elements are assembled together into a single compact device and mounted on a moving stage allowing transverse displacement with respect to the beam.

4.2.2 Coupling of the HE_{11}^{x} mode

Controlling the injection of light into cantilevered microfabricated SNOM probe is not a straightforward task. In fact, the large base opening diameter (6 μm) allows many electromagnetic modes to be coupled into the probe. As the guided modes reaches cutoff, a part of their energy is absorbed or reflected back by the metallic coating, and a part is released outside the probe. For this reason, as light is injected into the probe, a multi-modal far-field pattern is, in general, observed.

A number of published works have demonstrated that the coupling of HE_{11} mode in metalized tapered fibers provides the largest optical power throughput. It is quite intuitive to try coupling the HE_{11}^{x} mode by focusing a linearly x-polarized beam into the tip base opening. A quantitative description of modes excitation within the probe is hard to carry out. In fact, although the estimation of the coupling efficiency between the focused beam and the eigenmodes supported in a 6 μm wide metallic cylindrical waveguide can be performed by means of well-known overlap integrals, the intermode conversions taking place in the taper can be evaluated only in some particular cases [81]. As a result, it is difficult to theoretically predict how much power is actually coupled to the HE_{11}^{x} mode at the cutoff diameter. In Fig. 4.11 we present the calculated electric field distribution in the focal plane of a NA=0.4 lens focusing a x-polarized gaussian beam ($w_0 = 1.5$ mm). Calculations are performed by using the FFT-based method proposed by Mansuripur [56].

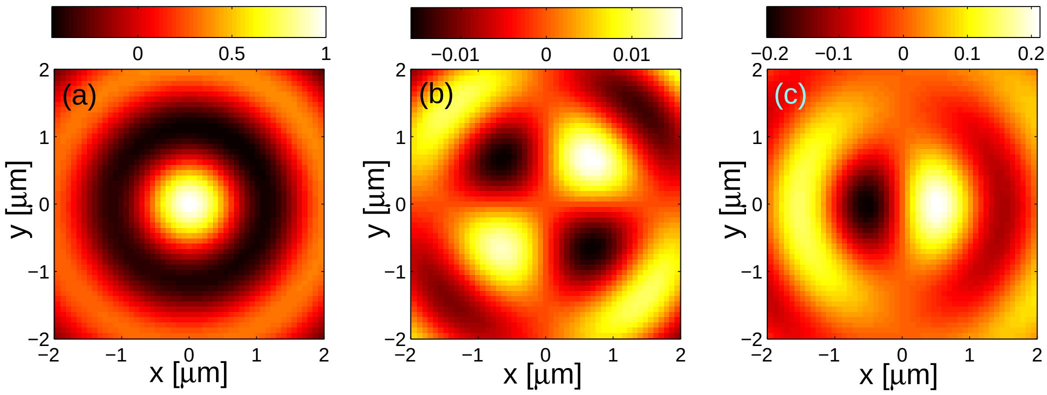

Figure 4.11: Real part of the normalized electric field in the focal plane of a focused linearly polarized beam (NA=0.4): (a) Re$\{E_x\}$, (b) Re$\{E_y\}$ and (c) Re$\{E_z\}$.

Since the patterns of the E_x and E_y components look very similar to those of the TE_{11}^{x} eigenmode calculated at the waveguide entrance (Fig. 4.2), we expect a selective excitation of the HE_{11}^{x} mode into the probe. Results from measurements confirm this prediction (Fig. 4.12). Far-field measurements are limited to the transverse x and y components of the field, because the longitudinal component cannot be imaged without the use of some kind of probes [82, 83]. In Ref. [58] a convincing explication of the limitation of far-field imaging systems in detecting longitudinally polarized fields is presented.

We find that two different patterns having orthogonal polarizations are imaged at the probe exit. A bright spot polarized in the x-direction (the same polarization of the injected beam) is superposed to a less intense four-lobe pattern, y-polarized. The phase characterization of the two field distributions is performed consequently, by selecting one pattern at once with the help of the polarizer in the interferometer object arm. In order to make the reference beam interfering with the object beam, the $\lambda/2$ plate (the HWP in the drawing of Fig. 4.10) placed on the reference arm is rotated by 45°. Intensity patterns are collected by simply blocking the reference beam and recording the object image on the CCD camera.

If we look at Fig. 4.12(b) we notice that the phase map of the spot is well defined only over a rather small area. This effect is due to the difficulty of obtaining a system of fringes with uniform contrast with the interference of a plane wave (reference) and a high-contrast object field. Although the wavefront curvature is not as evident as in the calculated plot, we remark that the phase distribution corresponding to the central region

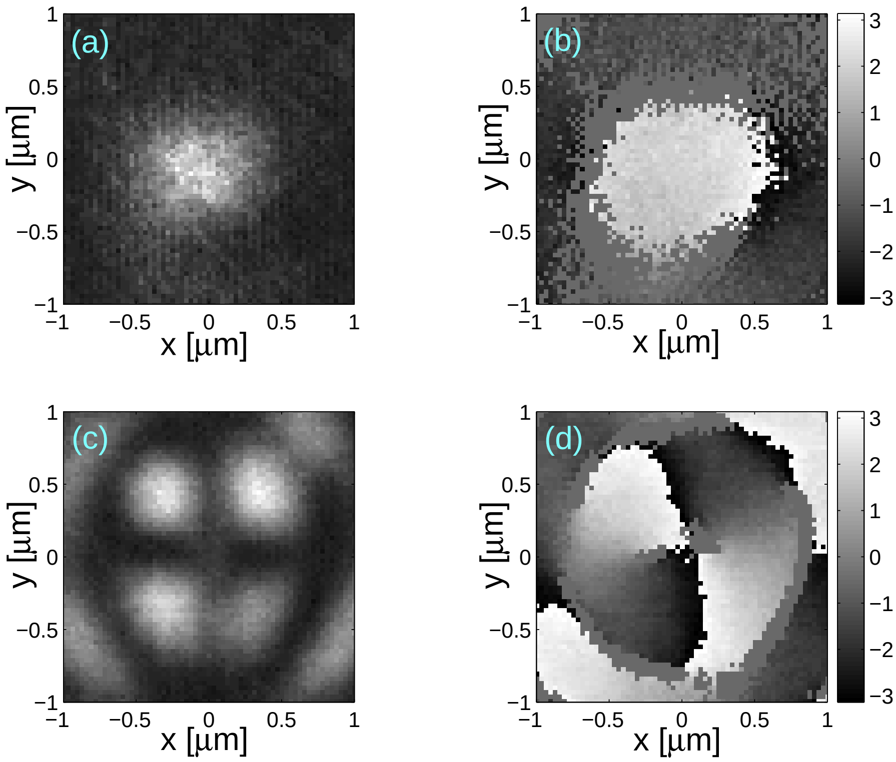

Figure 4.12: Far-field emission pattern of microfabricated fully metal-coated probe after injection of a focused linearly polarized beam. Intensity and phase distribution of (a,b) x component and (c,d) y component of the optical field respectively. *Measurement in collaboration with P. Tortora*

of the pattern is in good agreement with calculations (Fig 4.5). A good agreement is also found for the y-polarized four-lobe pattern of Fig. 4.12(d), revealing the two well-defined edge dislocations between adjacent lobes.

4.2.3 Coupling of the TM_{01} mode

We couple the TM_{01} mode by focusing a radially polarized beam into the probe base opening. In the focal plane, a focused radially polarized beam presents the electric field components distributed as in Fig. 4.13: a comparison with Fig. 4.6 suggests that injecting a radially polarized beam is one of the most suitable way to efficiently couple the TM_{01} mode into the probe.

A preliminary check of the beam quality is performed by imaging the focal plane distribution of the focused beam. The characteristics of radially and azimuthally polarized beams produced by means of LC elements are well known [84]. Particular care is taken in the voltage settings and the alignment of the LC device, in order to provide a ring-shaped pattern as homogeneous as possible. The polarization state of the beam is checked with the help of a rotating polarizer. The injection of a focused radially polarized beam is highly sensitive to misalignments. The most delicate step consists of bringing the optical axis of the focusing system as close as possible to the probe axis: if the focused beam

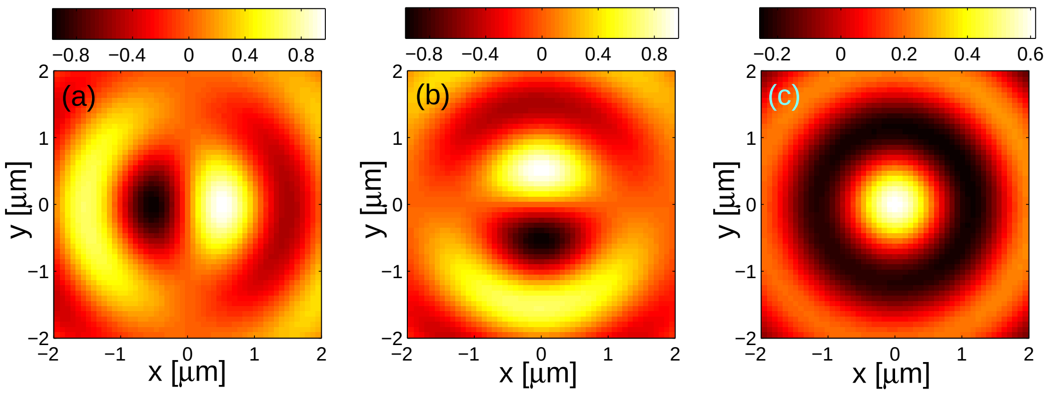

Figure 4.13: Real part of the electric field in the focal plane of a focused radially polarized beam (NA=0.4): (a) Re$\{E_x\}$, (b) Re$\{E_y\}$ and (c) Re$\{E_z\}$.

has not a fully circular symmetry at injection, the dominant linear field component will couple to other modes in a non controlled way. Injection is successfully achieved when an annular pattern is imaged in correspondence to the probe tip. If the mode coupled into the probe is the TM_{01}, the emitted ring-shaped far-field pattern must also have a radial polarization state, as the calculations reported in the previous section show.

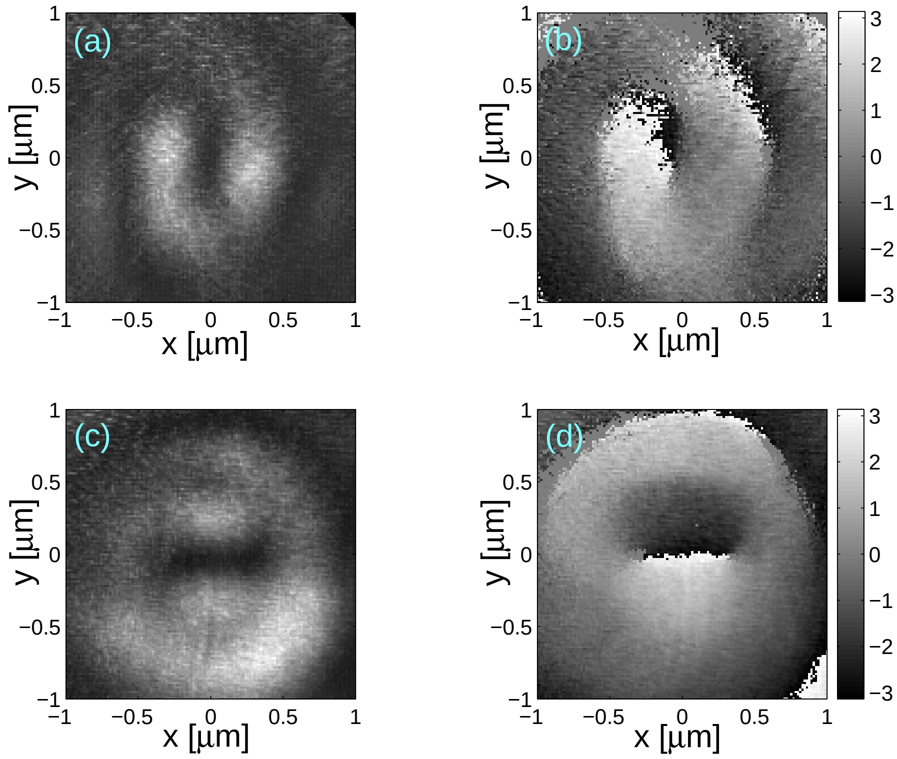

Figure 4.14: Far-field emission pattern of microfabricated fully metal-coated probe after injection of a focused radially polarized beam. Intensity and phase distribution of (a,b) x component and (c,d) y component of the optical field respectively. *Measurement in collaboration with P. Tortora*

With the help of the polarizer placed on the object arm of the interferometer, we can select the x and y components of the pattern and map their intensity and phase distributions. Results of measurements are presented in Fig. 4.14. Two lobes oriented parallel to the field polarization are obtained when the polarizer is rotated. The corresponding phase distributions show a well defined π-phase step line between the two lobes as predicted by calculations (see Fig. 4.9). This line represents an example of edge dislocation [63]. In addition, it is interesting to show the measurement obtained without polarizer. In Figs. 4.15(a) and 4.15(b) we respectively show the intensity and the phase distribution of the field emitted by the probe.

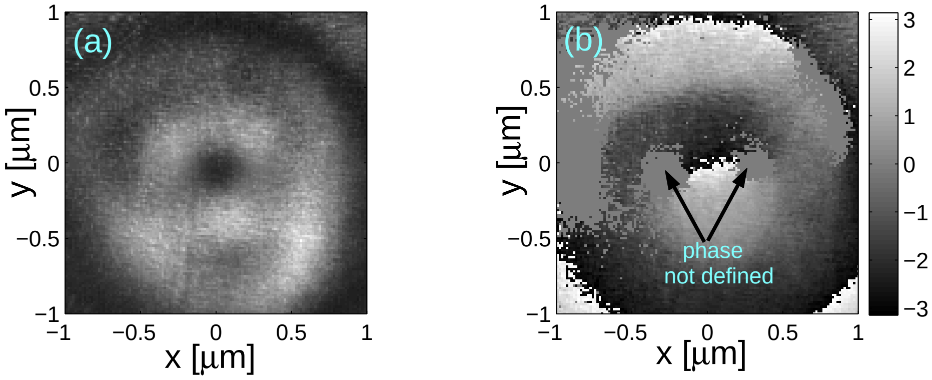

Figure 4.15: Far-field emission pattern of microfabricated fully metal-coated probe after injection of a focused radially polarized beam: (a) overall intensity distribution of the optical field and (b) phase distribution of the y component only. *Measurement in collaboration with P. Tortora*

The interferogram is obtained by interfering a linearly y-polarized reference beam with the object. In this way, the phase map of the y-component of the object field is obtained, as the horizontal defect line demonstrates. Moreover, we remark that the phase retrieval algorithm fails to calculate the phase distribution along the horizontal diameter of the annular patter, where the object field is perpendicularly polarized with respect to the reference beam, thus giving no interference at all.

4.3 SNOM measurements

In this section, the emission patterns of microfabricated probes are imaged by means of a collection-mode SNOM. The tip-on-tip setup is depicted in Fig. 4.16.
The laser source is an Ar^+ laser emitting at 514.5 nm. The scan is performed by moving the sample with respect to the collecting probe. The sample tip is placed on a piezo scanner. In order to maintain the injection as stable as possible during the scan, the injection system is connected to the moving part of the scanner. Scans are performed in transverse planes at fixed distances from the sample tip apex. Thanks to the cantilever-based collecting probe, the sample-probe distance can be controlled by using a static AFM control system, implemented in the setup. The position of the tip apex is determined after performing a "in-contact" topographic scan at constant force (Fig. 4.17). The "contact"

condition is reached when a force of 0.1 nN is exerted by the probe on the sample. Once the position of the tip apex is determined, the feedback system is switched off. A known voltage is then applied to the scanner in order to carry out a controlled vertical displacement of the sample. If not explicitly specified, the measurements shown in the following are performed on a plane 10 nm from the sample tip apex.

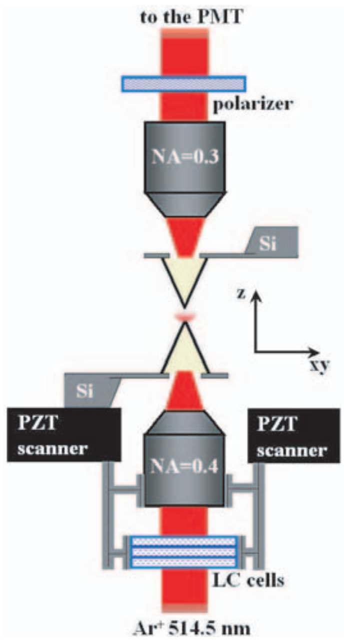

Figure 4.16: Experimental arrangement used for the near-field scan of emission patterns of microfabricated fully metal-coated SNOM probes.

Collection properties of fully-coated quartz probe have been investigated in some recent works [39, 84]. In particular, from these papers it turns out that the collection efficiency of transversely polarized fields is strongly affected by the roughness of the probe metallic coating: a rough coating impedes the coupling of transverse fields, while a smooth coating favors it. Longitudinally polarized fields are almost unaffected by the probe roughness. This characteristics can be usefully exploited for a selective mapping of transverse and longitudinal field components. In the present case, it would be interesting to map all the three cartesian components of the field emitted by the sample tip. For this purpose, collection is performed by using alternatively probes with rough metallic coating (*rough probes*) and probes with smooth and homogeneous metallic coatings (*standard probes*). Light coupled into the collecting probe is sent to the photomultiplier by means of the collection optics described in chapter 2. A polarizer placed after the collection objective allows polarization filtering of the scanned field. Nevertheless, because of the inter-mode conversions and depolarization effects taking place inside the collecting probe, the original polarization state of the object field is not conserved during the point-by-point image formation process. Therefore, the use of such a polarizer can provide only a low-accuracy mapping of the transverse components of the object field.

4.3.1 HE^x_{11} mode

In the previous section we demonstrated that far-field observations can provide useful information on the modes coupled into the microfabricated probe. Since the HE^x_{11} mode can be coupled by injecting a linearly x-polarized beam, the LC elements producing axially polarized beams are not used in this particular case. The sample under investigation is constituted by the standard probe shown in Fig. 4.17. The measured apex diameter is 70 nm.

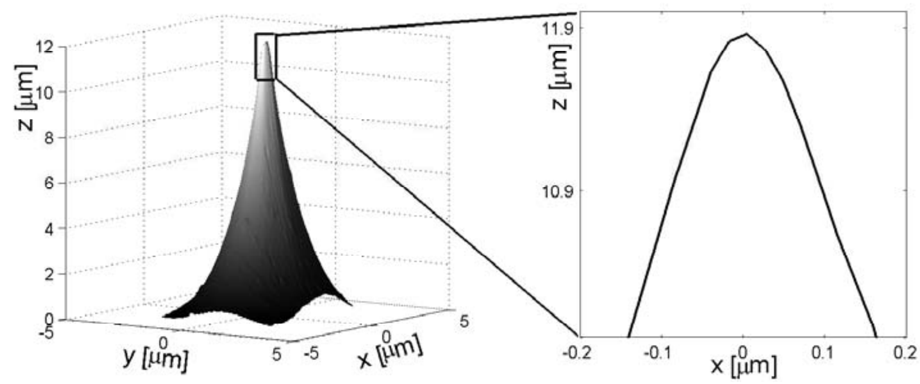

Figure 4.17: Topography of the sample tip. In-contact AFM scan.

After light injection, scans of the tip with a standard probe are firstly performed. Depending whether the polarizer is oriented parallel or perpendicular to the polarization of the injected beam, patterns reported in Fig. 4.18(a) and Fig. 4.18(b) are, respectively, obtained. If we assume that the calculated field shown in Fig. 4.4 represents a realistic description of the physical field emitted by the sample probe, then the discrepancy between measurements and calculations must be accounted to the collection mechanism of the collecting probe. It can be observed that the detected images are very close to the transverse components of the electric field in a plane 250 nm above the sample tip apex (Fig. 4.5).
This indicates that the collected signal comes form the (transversely polarized) light coupled in a region ~ 240 nm above the apex of the collecting probe. Therefore, a positive "vertical offset" is added to the position of the transverse plane where the scan is performed. At a distance of 240 nm from the apex, a probe characterized by a 34^o apex angle has a diameter of ~ 147 nm. This value represents the effective width of the probe and is directly connected to the lateral resolution in imaging transverse fields. A lateral resolution of $\sigma_T \simeq 150$ nm for the collection of transverse fields has also been measured in the previous section. It is particularly interesting to underline that the two estimations of lateral resolution of the probe in collecting transversely polarized fields are in good agreement with the cutoff diameter of the guided HE_{11} mode (160 nm at $\lambda = 488$ nm [75]).

When the scan is performed using a rough probe (and no polarizer), we obtain the image showed in Fig. 4.18(c)). The rough probe filters the transverse field components. The result consists of an apparent enhanced detection of the longitudinal field. If we

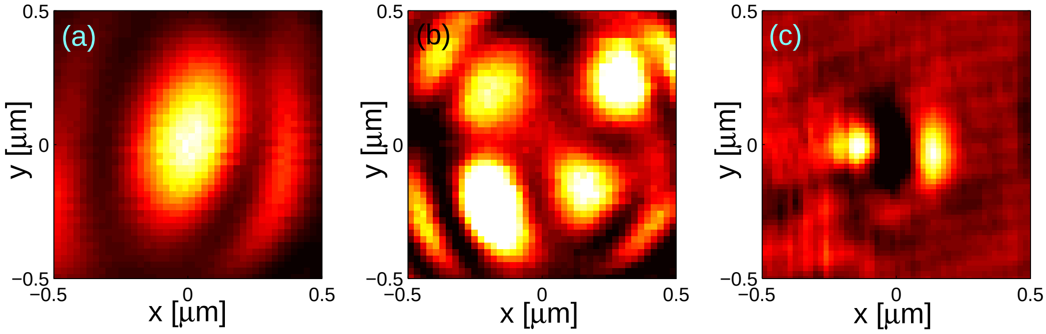

Figure 4.18: Tip emission of the HE_{11}^{x} mode: near-field intensity distributions in a plane 10 nm from the probe apex. Scan performed with a standard probe: (a) polarizer parallel to the injected beam polarization, (b) polarizer perpendicular to the injected beam polarization. (c) Scan performed with a rough probe and no polarizer.

compare measurement and calculations, it is difficult to refer the detected pattern to the calculated field distributions either at 10 nm (Fig. 4.4(c)) or at 250 nm (Fig. 4.5(c)) from the sample tip apex. In fact, lobes extension and distance between the lobes suggest that the measured distribution represents an intermediate situation between the two calculated cases. Therefore, the "vertical offset" effect is still present but less important as compared to the measurements of transversely polarized fields previously presented. As a consequence, the z-oriented electric field collected during the scan couples to the collecting probe in a region closer to the apex, corresponding to a smaller probe diameter. The lateral resolution of $\sigma_T \simeq 110$ nm for the collection of longitudinal fields estimated in the previous section supports this conclusion.

4.3.2 TM_{01} mode

The interest of coupling the TM_{01} mode into the probe relies on the possibility of generating an ultra-small "hot-spot" confined at the tip apex. Due to its longitudinal polarization the "hot-spot" cannot be imaged with far-field imaging systems [58]. To our knowledge, no direct measurements of such a confined field have been carried out so far. Nonetheless, we cite the remarkable work of Yatsui *et al.* [85] who managed to measure the localized field enhancement generated via plasmon excitation (in the infrared region) at the end of a pyramidal microfabricated silicon probe fully aluminum coated.

With the help of a collection-mode SNOM using cantilever-based probes, we were able to access this field. In the following we report the result of the scans performed with a fully metal-coated rough probe. In Fig. 4.19(a) we present the image obtained by scanning the sample probe at 10 nm from the apex. We observe a strongly localized spot whose HWHM does not exceed 100 nm. The detected image is the result of the convolution of the probe function with the actual object field. If we assume a probe lateral resolution of ~ 110 nm, the actual dimensions of the deconvolved spot are within 40 nm, as predicted by calculations (Fig. 4.8(c)).

As the scanned plane is brought far away from the tip, the longitudinally polarized hot-spot vanishes. In fact, at a distance of 1.5 μm from the apex a second scan reveals the presence of the ring-shaped distribution (Fig. 4.19(b)) similar to the far-field emission pattern measured with the HRIM.

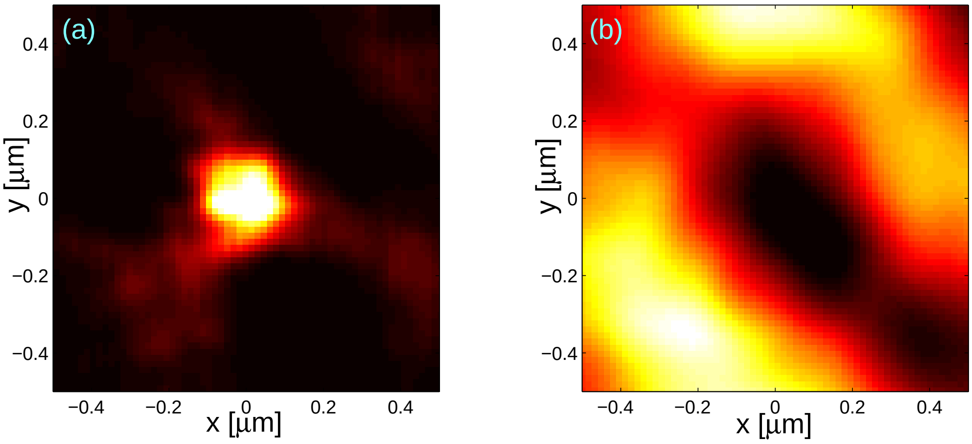

Figure 4.19: Tip emission of the TM_{01} mode: (a) intensity distributions in a transverse plane 10 nm from the sample tip, (b) intensity distribution in a transverse plane 1.5 μm from the sample tip. Measurements are performed with a rough probe.

4.4 Conclusions

Investigations on the guiding properties of microfabricated, fully metal-coated quartz probes have been conducted. The most widely accepted approach for studying metalized fiber-based SNOM tips relies on the assumption that they behave like tapered metallic cylindrical waveguides. Following this model, we studied light propagation within the probe in terms of guided modes. In particular, two modes are considered: the HE_{11} and the TM_{01}. Compared to all the guided modes, the former provides the highest power throughput, while the latter generates an enhanced field confined in an ultra-small region at the probe apex.

Far-field measurements conducted by means of a Mach-Zehnder interferometer implemented on an optical microscope allowed us to map phase and intensity distributions of the field emitted by the probes after proper light injection. We demonstrate experimentally that a selective and controlled coupling of the HE_{11} and the TM_{01} modes can be carried out by injecting focused linearly and radially polarized beams respectively.

The selective coupling of the TM_{01}^{x} mode into fully metal-coated quartz probes is particularly attractive because of the longitudinally polarized ultra-small spot produced at the end of the tip. Near-field scans of the probe apex have been carried out with a collection-mode SNOM. We give a direct experimental evidence that, after injection of a radially polarized beam, a single spot confined in a region < 100 nm is actually produced.

Chapter 5

Towards a nanoscopic virtual probe

One of the basic requirements of many super-resolving imaging systems is to illuminate the sample with a highly confined optical field. Well-established Scanning Near-field Optical Microscopy (SNOM) techniques can accomplish this in different ways. For example, it is possible to obtain a localized field by tightly focusing higher-order Hermite-Gaussian beams on metal tips, which can be employed as nano-sources [86]. Another possibility is to use metal-coated tapered monomode optical fibers having a subwavelength hole at the apex [87] or microfabricated fully metal-coated probes [88]. Some investigations based on numerical calculations (see, for example, Ref. [71]) and experimental measurements [38, 39, 84] revealed that the strongest localization of the emitted field is connected to the presence of a longitudinally polarized field. Nonetheless, the main drawback in the exploitation of such a field is the necessity of the probe itself, which is, in general, fragile and difficult to reproduce on a large scale.

One solution to this problem was suggested by Grosjean *et al.* [89, 90], who proposed the use of virtual (or immaterial) tips, in near-field microscopy. In those papers, the authors describe the concept of a virtual tip as a purely evanescent pattern obtained by suitable interference of radially polarized Bessel-Gauss beams at the hemispherical surface of an axicon element. The experimental setup allowed the generation of an evanescent, non-diffracting and longitudinally polarized field confined over a circular region of diameter $\sim \lambda/5$, to be used for sample illumination. Another realization of a non-radiating source is presented in Ref. [91], where the combined use of interfering waves and filtering masks produced a virtual optical probe having FWHM $= 0.42\lambda$.

In this chapter, we consider an innovative solution for a non-radiating and highly spatially confined light source. Such a source is obtained by a proper excitation of Surface Plasmon Polaritons (SPP). In particular, the field enhancement produced by SPP excited in a suitable Distributed Feedback System (DFS) can be used as a virtual optical probe. During the few last years, optical phenomena linked to SPP have attracted attracted gaining interest, mainly due to the possibilities of applications such as plasmonic crystals and photonic surfaces [92, 93, 94, 95], plasmonic band gap lasers [96] and two-dimensional optics [97, 98]. A number of different types of metallic micro-cavities for SPP have also been considered in the past: most of them being buried in the metal film [99] or placed out-of-plane with respect to the propagation direction of SPP [100, 101, 102]. In the present work we consider the possibility of using a plasmonic field as a nano-source for near-field microscopy. This choice is particularly interesting for several reasons. Most importantly, as will be shown, the proposed device couples the benefits of highly-sensitive, plasmon-based sensors [103] and strongly confined, non-radiating sources.

SPP can be coupled on metallic nano-particles or metallic surfaces. A strong field localization effect can be observed with metallic nano-particles [104], but it is hard to exploit it because of the practical difficulty of handling small objects. Alterantively, SPP localization can be achieved by structuring planar metallic surfaces. We propose a flat surface surrounded by a pair of sinusoidal gratings acting as Distributed Bragg Reflectors (DBR) for surface waves. With this configuration, as SPP are trapped in the flat region by the DBRs, they show a cavity-like resonating behavior. The field enhancement associated with the lowest order mode is then used as a plasmonic virtual probe.

In order to perform our numerical analysis, we implemented the differential method of Chandezon, the C-method, (see, for example, Ref. [105]) and its extension to multi-layered periodic gratings proposed in Ref. [106]. This method is particularly suited for studying this kind of problem since it allows smooth grating profiles to be considered without performing any multi-layer structure discretization [93, 107, 108, 109].

5.1 Excitation of surface plasmon polaritons on flat and corrugated surfaces

Surface Plasmon Polaritons are associated with strong electromagnetic fields confined at metal-dielectric interfaces, where the real part of the permittivities of the two media have opposite signs. SPP can be excited under specific illumination conditions: in the following we will consider the two-dimensional Kretschmann configuration, as shown in Fig. 5.1.

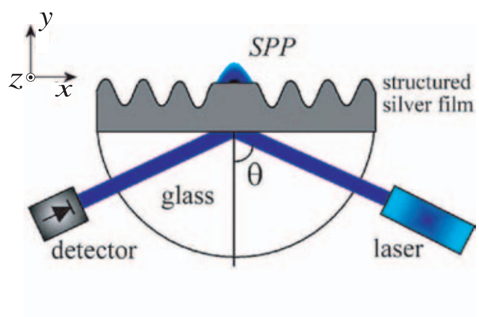

Figure 5.1: Excitation of Surface Plasmon Polaritons in the Kretschmann-Raether configuration. Light incident at angle θ with respect to the surface normal, hits the silver film deposited on the flat surface of a cylindrical glass lens and is then reflected. The reflected light is used to monitor the coupling of photons with plasmon polaritons at the metal interface.

A thin film of silver is deposited on the flat surface of a semi-cylindrical glass lens. The incident radiation is a p-polarized plane wave passing through the glass and then impinging on the metal layer with a varying angle θ with respect to the surface normal. The illuminating plane wave is associated with a magnetic field vector having amplitude

$|H_0| = 1$ and orientation parallel to the z-axis. The coupling of photons to plasmon polaritons at the metal-air interface is monitored by means of the normalized coefficients R and T, defined as the sum of the reflected and transmitted order efficiencies (η_i^r and η_i^t, with $i = 0, \pm 1, \pm 2, \ldots$) as shown in Eq. (5.1):

$$R = \sum_i \eta_i^r \quad , \qquad T = \sum_i \eta_i^t. \tag{5.1}$$

The values of the permittivities of Silver $\epsilon_{Ag}(\lambda)$ used in the calculations are taken from Johnson and Christy [110].

In order to realize a DBR, we first determine the conditions under which SPP can be coupled on a flat silver film surface and subsequently calculate the SPP wave vector associated with the propagation along the silver-air interface. The spatial periodicity of SPP is determined by the real part $Re\{k_\parallel\}$ of the wave vector component parallel to the interface. Once $Re\{k_\parallel\}$ is calculated, a suitable corrugation of the silver film is introduced in order to make a one-dimensional DBR for SPP [111].

First we consider a flat silver film of thickness $t = 50$ nm. The parameter R is calculated for different illumination wavelengths λ and different incidence angles θ, according to the setup of Fig. 5.1. The map of the reflection coefficient $R(\lambda, \theta)$ is shown in Fig. 5.2 (linear color scale).

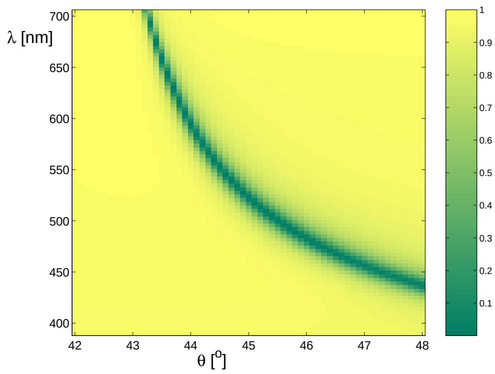

Figure 5.2: Calculated map of the reflection coefficient $R(\lambda, \theta)$ of a flat thin silver film ($t = 50$ nm) illuminated in the Kretschmann-Raether configuration at different wavelengths λ and incidence angles θ. Dark zones (low reflectivity) correspond to the excitation of SPP.

The dark region corresponds to diminished reflected light intensity, where an efficient transfer of radiative energy to SPP modes occurs. If we restrict our attention to $\lambda = 470$ nm and $\theta = 45.4°$ we can excite a SPP having wave vector $Re\{k_\parallel\} = 14.248\ \mu\text{m}^{-1}$. Since the simplest Bragg mirror couples the incident and the reflected light via its first harmonic component, we structure the metal-air interface of the silver film with a purely sinusoidal profile having period $\Lambda \approx \pi/Re\{k_\parallel\} = 220.5$ nm. Consequently, a frequency band gap in the SPP excitation curve is expected to open [112, 107]. We consider the case of a sinusoidal corrugation having a period of $\Lambda = 220$ nm and an amplitude of $h = 10$ nm. The result is reported in Fig. 5.3. The SPP-coupling region of Fig. 5.2 is split into two arms by the presence of the periodic modulation of the surface. The center of the band gap can be tuned to different wavelengths along the SPP excitation curve, depending on the period of the modulation Λ and on the illumination angle θ. The two standing SPP waves excited at the edges of the gap present the same spatial periodicity while having different energies as shown in Ref. [108].

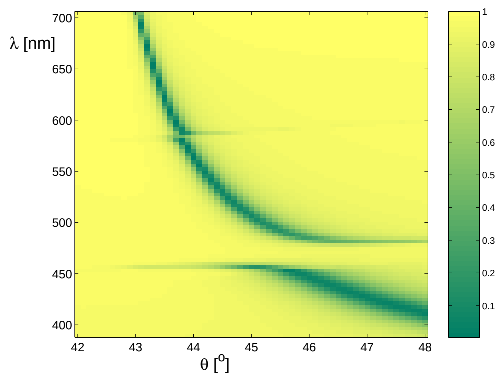

Figure 5.3: Calculated map of the reflection coefficient $R(\lambda, \theta)$ of a thin silver film illuminated in the Kretschmann-Raether configuration at different wavelengths λ and incidence angles θ. The metal-air interface is corrugated with a sinusoidal profile of period $\Lambda = 220$ nm. A band gap at $\lambda \approx 470$ nm emerges due to the presence of the corrugation.

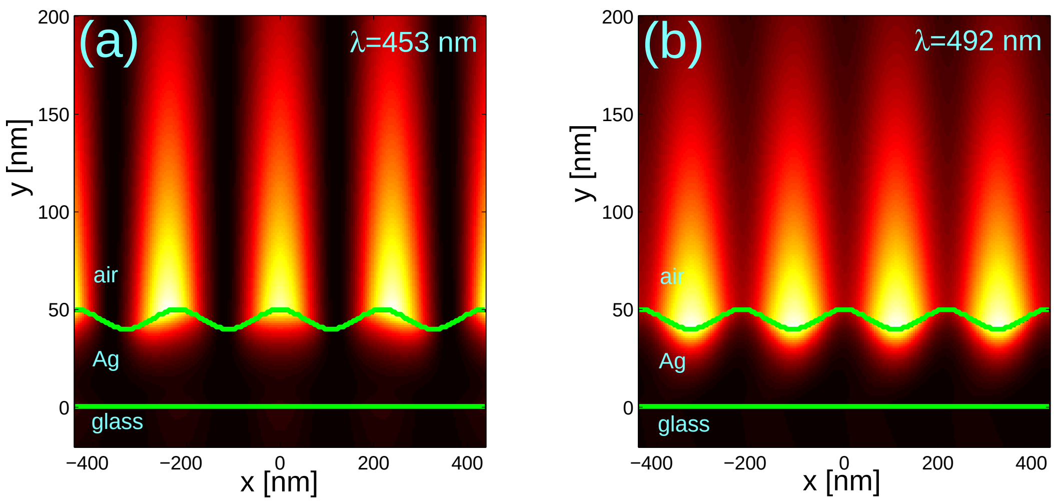

Figure 5.4: Near field distribution of the magnetic field squared amplitude associated to surface plasmons coupled on a sinusoidal silver surface. SPP's wavelengths lie at the lower (a) and at the upper (b) border of the band-gap opened by the grating.

5.2 Microcavities for surface plasmon polaritons

The cavity we propose consists of a flat surface region surrounded by DBR on both sides. Two possible arrangements are considered, as shown in Fig. 5.5. In the case of Fig. 5.5(a) the modulation is a raised profile on the surface of the metal layer, while in the case of

Fig. 5.5(b) the modulation is etched into the metal layer. In both cases, the silver film thickness corresponding to the flat region is $t = 50$ nm.

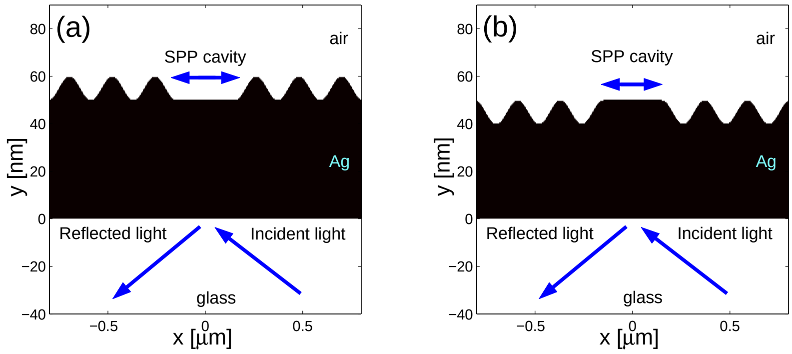

Figure 5.5: Topographic profiles of two possible configurations of the cavity. In case (a) the modulation is a raised profile on the surface of the metal layer, while in case (b) it is etched into the layer.

The C-method is a Fourier-based method for solving periodic diffraction problems. Therefore, the case of a single cavity surrounded by Bragg mirrors cannot be treated directly with such a method, since an infinite calculation domain should be considered. Nevertheless, approximate solutions are possible, for example by using a super-lattice of cavities. Each cavity is separated from its neighbors by a Distributed Bragg Reflector (DBR) of finite length. In such a situation, a critical parameter is the length of the DBR: too large DBRs are impractical, while too short DBRs allow strong cross-talk effects between cavities. Spurious cross-talks can be reduced using several approaches (see, for example, Ref. [113]). In our case, we performed a preliminary set of test calculations in order to find a reasonable value for the DBR length. We monitored the field enhancement factor associated with the SPP inside the cavity as a function of the number of DBR periods on each side of the flat region. The result is shown in Fig. 5.6.

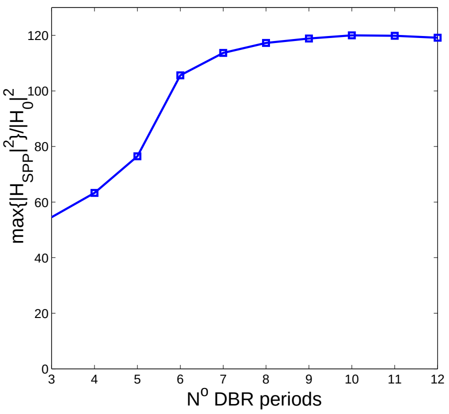

Figure 5.6: Convergence of the field enhancement factor as a function of the DBR period considered in the calculations.

The influence of the cross-talk has been evaluated by calculating the field enhancement factor $\max\left\{\left|H_{SPP}\left(x,y\right)\right|^2\right\}/\left|H_0\right|^2$. We observed that the field enhancement factor converges asymptotically as the length of the DBR increases. If the number of DBR periods is ≥ 16, the field enhancement factor shows small variations $\leq 1\%$. The compromise we adopted is to consider 10 grating periods on each side of the cavity.

In Fig. 5.7 the coefficients R and T are plotted as functions of the cavity length L. Data points associated with the minima of R and maxima of T correspond to the excitation of different modes in the cavity. The zero- and the first- order modes are found at $L_{n=0} = 112$ nm and $L_{n=1} = 330$ nm respectively. Calculations are in good agreement with the prediction of the well-known formula

$$Re\{k_{\parallel}\} \cdot L \sim (2n+1)\pi/2 \tag{5.2}$$

This result demonstrates the resonant behavior of the structure under investigation. Both configurations shown in Fig. 5.5 present the same behavior. The ripple effect present in the T profile is mostly liked due to a secondary resonance which has no significative impact on the performances of the device. It is interesting to remark that, close to the resonance points, the SPP is partially converted into free-space propagating photons, as the non-zero value of the transmission coefficient demonstrates. This phenomenon is attributed to the scattering performed by the surface discontinuities at the cavity boundaries. A similar effect is also frequently observed in the case of photonic crystals. In order to minimize this effect it has been demonstrated that it is possible to design modulated profiles to achieve adiabatic mode conversion between the topographically different regions of space [114].

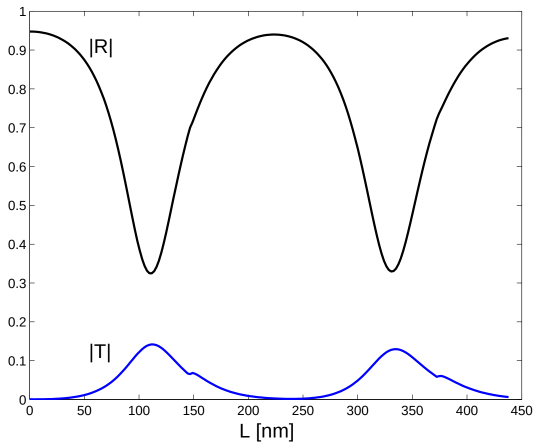

Figure 5.7: Reflection (R) and transmission (T) coefficients of a DFS for SPP for different lengths of the flat region. The two plots show a typical resonance profile.

Unfortunately, in our case, a smoother change between allowed (flat region) and forbidden (DBR) regions would present a drawback in terms of quality of the virtual tip as will be shown in the next section.

5.3 Plasmonic Virtual Probe

The goal of this work is to demonstrate that a localized, non-radiating light nano-source can be realized by coupling SPP onto a suitable resonant metallic structure. For this reason, we focused our attention on the lowest-order cavity mode. Calculations of the squared amplitude distribution of the magnetic field associated with the zero-order are shown in Fig. 5.8 for both of the considered configurations. At the metal-air interface, a field enhancement factor $\max\{|H_{SPP}(x,y)|^2\}/|H_0|^2 = 120$ is found.

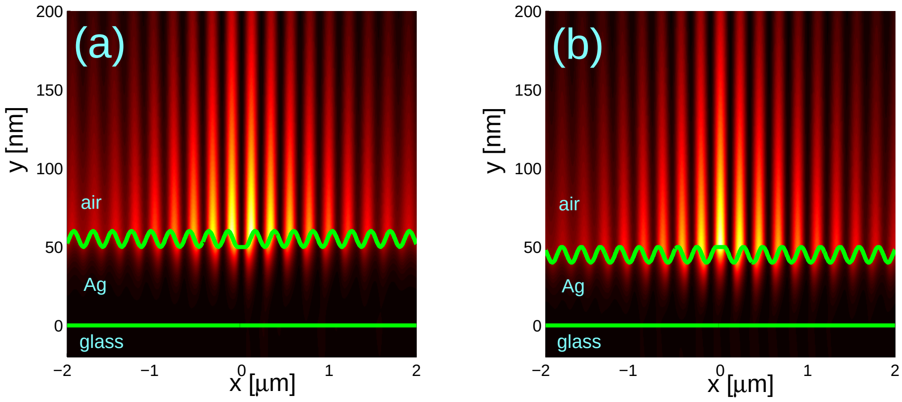

Figure 5.8: Squared amplitude of the magnetic field associated with the plasmonic zero-order mode excited in the two considered DFS configurations: (a) raised profile, (b) etched profile.

Although the lowest order modes are excited in both cases at the same cavity length $L_{n=0} = 112$ nm, their near-field distributions are significantly different. In fact, in the case (a), the $n = 0$ mode has a node in the center of the flat region, while in case (b) it shows a maximum of amplitude. The presence of the two lobes makes the configuration (a) unusable to generate a single, localized and non-radiating light source. On the other hand, configuration (b) is more interesting for our purposes because of the single central lobe confined to a region ≤ 100nm. In the following, the near-field distribution shown in Fig. 5.8(b) will be named a plasmonic virtual probe. Its electric field vector is oriented along the y-direction.

The presence of lateral lobes surrounding the virtual probe is undesirable for light nano-source applications. Sidelobe intensity is directly connected to DBR amplitude. As the modulation amplitude increases, the sidelobes are reduced, while the lateral extension of the SPP mode in the flat region remains unchanged. Unfortunately, a large modulation amplitude introduces strong perturbations of the SPP mode, leading to an increase in scattered light. We considered different modulation schemes in order to achieve an acceptable trade-off. An interesting result is reported in Fig. 5.9.
In this case, the first half-period of the DBR is etched with a much larger depth, which results in a more dramatic SPP damping and a consequent decrease of the sidelobe intensity. As expected, we found a larger diffraction efficiency ($T = 24\%$) for the transmitted light as compared to $T = 13.8\%$ calculated for the configuration of Fig. 5.8(b). The field enhancement factor at the metal-air interface is reduced to a value of

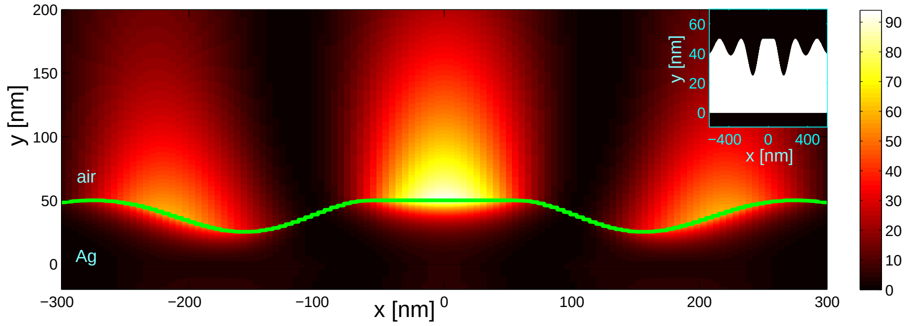

Figure 5.9: Virtual probe excited in a cavity surrounded by a modified Bragg mirror (see inset for a detail). The squared amplitude of the magnetic field of the virtual probe is enhanced by a factor of 94 with respect to the incident plane wave. The effect of the overetched modulation is to reduce the intensity of the lateral lobes.

$\max\{|H_{SPP}(x,y)|^2\}/|H_0|^2 = 94$. In this configuration, the squared magnetic field distribution of the virtual probe close to the metal surface is described by a gaussian profile having $\sigma = 40$ nm. In conclusion, a better quality of the virtual probe can be obtained to the detriment of a smaller SPP coupling efficiency and a larger amount of transmitted light.

5.4 Scan of a small defect in a glass plate

One of the possible applications of the proposed plasmonic virtual probe is as light nanosource in a Scanning Near-field Optical Microscope system. As the excitation of SPP is highly sensitive to perturbations at the metal-air interface, the behavior of the plasmonic virtual tip when a sample is brought into close proximity constitutes an important topic to investigate. For this reason, the scan of a small object has been numerically simulated. In particular, we are interested in evaluating the contrast of the detected signals as the sample is scanned through the virtual probe. The considered sample consists of a flat glass plate having a small defect, whose profile is given by:

$$f(x) = \begin{cases} h \cdot exp\left[-\frac{(x+w-\Delta)^2}{s^2}\right] & x < -w \\ h & -w \le x \le w \\ h \cdot exp\left[-\frac{(x-w-\Delta)^2}{s^2}\right] & x > w \end{cases} \tag{5.3}$$

where $h = 50$ nm, $s = 10$ nm and $w = 20$ nm. The scanning variable Δ tracks the object lateral position with respect to the system of reference of the virtual probe. The sample must be placed close enough to the metallic structure to perturb the SPP: to this end we choose a distance of 100 nm from the cavity. In Fig. 5.10, the squared magnetic field in the region between the cavity and the sample is shown.
We remark that the energy contained in the SPP mode is strongly decreased due to the presence of the sample. The light is scattered into the transparent sample or reflected back into the glass with diffraction efficiencies $T = 24.25\%$ and $R = 72.25\%$ respectively and almost all of the energy hitting the silver film is re-radiated ($R + T = 96.5\%$). During the

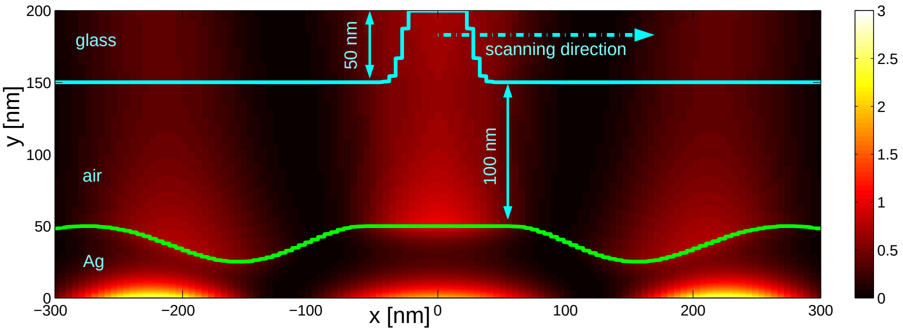

Figure 5.10: A glass plate with a small defect is scanned by the virtual probe. The sample introduces a strong perturbation in the neighborhood of the metal surface that gives rise to a dramatic loss in the photon-plasmon coupling efficiency.

scan, the interaction of the sample with the virtual probe can be monitored by collecting the light scattered by the sample (T) or the light reflected by the silver film (R). As the defect moves in the positive x-direction, the $R(\Delta)$ and $T(\Delta)$ coefficients are calculated and plotted as functions of the defect position Δ (Fig. 5.11).

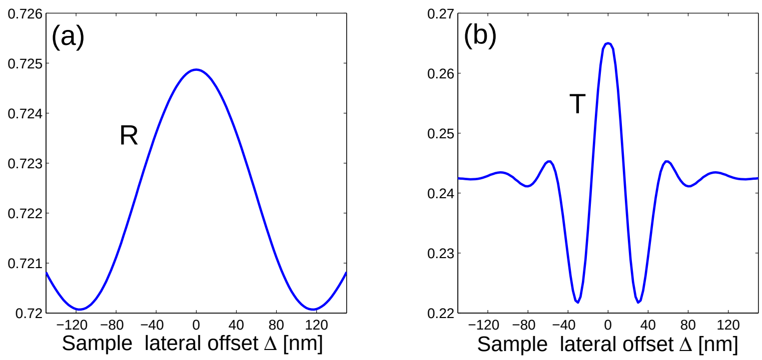

Figure 5.11: (a) Reflection coefficient R and (b) transmission coefficient T calculated for different positions of the defect in the glass plate during the scan.

The curve in Fig. 5.11(a) represents the reflected light as the defect moves through the virtual probe. The percentage of the reflected light gives an indication of the quantity of energy that is stored in the SPP mode. The overall modulation of the signal is very small ($\delta R \approx 0.5\%$) and its shape shows a central peak that is much broader than the extent of the defect. In particular, we observe that this curve is very similar to the squared field amplitude distribution of the SPP mode along the line $x = 150$ nm. We can argue that, as the lateral extension of the defect is smaller than the lateral dimensions of the virtual probe, the reflection coefficient profile represents the virtual probe squared field as probed by the defect itself. The profile shown in Fig. 5.11(b) represents the percentage of light that is transmitted into the glass plate. Here, the modulation is larger than in the previous plot ($\delta T \approx 4.2\%$) and its central peak much narrower. The profile shows the clear signature of the defect shape scanned through the virtual probe. Far away from the virtual probe, the modulation becomes negligible and the value of the transmission coefficient reaches the asymptotic value of $T = 24.25\%$. It is interesting to remark that the curves $R(\Delta)$ and $T(\Delta)$ are not directly correlated and the sum $R(\Delta) + T(\Delta)$ is not constant along the scan path. In order to explain this effect, absorption by the silver film must also be considered in addition to the radiative power (reflected and transmitted). Absorption is indeed proportional to the SPP coupling efficiency, that is highly sensitive to perturbations in close proximity of the metallic surface. In general we may say that, if perturbations are small, both reflected and transmitted power are small and viceversa, till a certain limit (depending on the kind of metallic structure) is reached. In the present case, as scatterer moves through the virtual probe, the plasmonic field is perturbed in a non-trivial way, leading the SPP coupling efficiency (and thus absorption) to vary significantly.

The simple situation considered here shows that objects having dimensions ≈ 50 nm can be detected with a relative contrast of $\delta T/T \approx 17.3\%$ by collecting the scattered light. On the other hand, the reflected light signal is weakly sensitive to objects smaller than the lateral extension of the virtual probe.

5.5 Conclusion

Computational investigations on the application of a plasmonic virtual probe as a non-radiating nano-source in near-field microscopy have been performed.

We first demonstrated that such a virtual probe can be generated by a properly corrugated thin metallic film supporting SPP modes. The two-dimensional configurations considered in this paper are suitable for the generation of longitudinally polarized fields localized in a region < 100 nm wide. We also demonstrated that, within certain limitations, it is possible to enhance the characteristics of the virtual probe in terms of SPP excitation efficiency, field enhancement and sidelobes intensity.

Such a device is very sensitive to environmental conditions because of the plasmonic nature of the excited field. When resonance conditions are met, the strength of the excited plasmon field is strongly sensitive to small changes in the refraction index at the metallic/dielectric interface. This effect is widely exploited in plasmon-based sensors. We demonstrated that it can also be usefully exploited in a near-field scanning system. The scan of a small defect in a flat glass plate has been numerically performed. Two outputs have been considered: the light reflected from the silver-glass interface and the light scattered by the sample. In particular, we observe a strong modulation of the scattered light as the defect is scanned through the virtual probe. Such a signal modulation is essentially due to the plasmon sensitivity to refractive index perturbations in close proximity of the metallic surface. With the combined use of these two signals, it is possible, in principle, to detected small objects with dimensions of few tens of nanometers.

Chapter 6

Summary and conclusions

In this thesis, some experimental and theoretical aspects of near-field and non-paraxial optical imaging are investigated. The main part of the work is focused on the resolution capabilities of microfabricated, fully aluminum-coated SiO_2 SNOM probes in collection and illumination-mode mountings.

Exploratory works performed at IMT-Samlab, Neuchâtel [115] opened a series of fundamental questions about the interaction of light with apertureless probes. The main topic is centered on the polarization-dependent coupling mechanism of light into such structures. Particular attention has been paid to the near-field region, where paraxial description of light is not valid anymore. In this situation, electromagnetic fields are not necessarily oriented perpendicularly to the average propagation direction, but distributed in all three dimensions. We manage to give some insights on the role played by longitudinally and transversely polarized fields in the image formation process performed with the considered SNOM probes.

Our findings on the interaction of longitudinal fields with metallic structures suggest interesting cross-over with plasmon optics. In this context, we propose a computational study on an original device providing a tightly confined, non-radiative light source: a plasmonic virtual probe. A preliminary work on the possible applications of the plasmonic virtual probe in near-field microscopy is also conducted.

Results are summarized in the following.

6.1 Apertureless $Si0_2$ SNOM probes in illumination-mode.

We consider the problem of light injection into microfabricated fully Aluminum-coated quartz probes. In particular, we show that a selective coupling of either the HE_{11} or the TM_{01} modes can be carried out by injecting focused linearly or radially polarized beams into the probe. Optical fields emitted by the probe after a controlled injection are characterized in intensity and phase with the help of an interferometric technique. We finally demonstrate, by means of near-field measurement, that a longitudinally polarized spot localized at the tip apex is actually produced when the TM_{01} mode is coupled into the probe.

6.2 Apertureless $Si0_2$ SNOM probes in collection-mode.

After demonstrating super-resolution capabilities in near-field imaging, the coupling and transmission of transverse and longitudinal fields into apertureless microfabricated near-field optical probes is investigated. The measurements are performed by raster scanning the focal plane of an objective focusing azimuthally and radially polarized beams using two metal-coated quartz probes with different metal coatings. A quantitative estimation of the collection efficiencies and spatial resolutions in imaging both longitudinal and transverse fields is made. Longitudinally polarized fields are collected with a resolution approximately 1.5 times higher as compared to transversely polarized fields and this behavior is almost independent on the roughness of the probe metal coating. Moreover, it is found that the roughness of the metal coating plays an important role in the coupling strength of transverse fields into the probes: the relative coupling efficiency for transverse fields diminishes with a rough metal coating, while that of longitudinal fields does not. This interesting effect allowed us to measure the purely longitudinally polarized field emitted by fully metal-coated SNOM probes in a tip-on-tip experimental arrangement.

6.3 Plasmonic virtual probe.

A confined, evanescent nano-source based on the excitation of Surface Plasmon Polaritons (SPP) on structured thin metal films is proposed. With the help of a suitable cavity, we numerically demonstrate that it is possible to trap SPP over a spatial region smaller than the diffraction limit. In particular, the enhanced plasmonic field associated with the zero-order cavity mode can be used as a virtual probe in near-field microscopy scanning systems. The proposed device shows both the advantages of a localized, non-radiating source and the high sensitivity of SPP-based sensors. The lateral resolution is limited by the lateral extension of the virtual probe. Results from simulated scans of small objects reveal that details with feature size down to 50 nm can be detected.

Appendix A

Vectorial modelization of converging high-NA optical fields

A FFT-based method for the calculation of optical field distributions in the focal region of high-NA lenses has been proposed in the second half of the eighties by Mansuripur [56, 57]. Within the Kirchhoff theory, such a calculation represents basically a field propagation problem: the only approximation is introduced in the interaction of the incident field with the lens, modeled as an infinitely thin object with ideal properties.

Given a general scalar field $\psi(x, y; 0)$ defined on the plane $z = 0$, we can calculate the field distribution at a distance z on the optical axis by solving the following integral:

$$\psi(x, y; z) = \lambda^{-2} \iint_{\sigma_x^2+\sigma_y^2\leq 1} \Psi(\sigma_x, \sigma_y) \cdot \exp\left\{\frac{2i\pi}{\lambda}\left[x\sigma_x + y\sigma_y + z\sqrt{1-\sigma_x^2-\sigma_y^2}\right]\right\} \mathrm{d}\sigma_x\, \mathrm{d}\sigma_y\,, \tag{A.1}$$

where Ψ is the Fourier transformation of ψ:

$$\Psi(\sigma_x, \sigma_y) = \iint_{-\infty}^{+\infty} \psi(x, y; 0) \cdot \exp\left\{\frac{-2i\pi}{\lambda}\left[x\sigma_x + y\sigma_y\right]\right\} \mathrm{d}x\, \mathrm{d}y\,, \tag{A.2}$$

and σ_x, σ_y are the normalized, dimensionless spatial frequency variables.

This formalism is not the only possibility. Alternatively, Luneberg equations [116], employing Hankel functions, can be used. In the present case, propagation is carried out in terms of a plane waves expansion of the field (angular spectrum representation): therefore the mathematical problem consists of calculate the Fourier transformation A.2 and use the result in the integral expression A.1. In the following, the case of an on-axis spherical lens is taken as a tutorial example to illustrate the method.

In the thin-element approach, the lens is a phase object transforming the (flat) wavefront of the incident field into a spherical wavefront converging in the lens focus. The lens is characterized by a entrance pupil of diameter D and a Numerical Aperture $NA = \sin\big(\mathrm{tg}^{-1} D/(2f)\big)$, where f is the lens focal length. The incident field has well defined polarization state: in order to simplify the formalism, we assume a linearly polarized field in the j direction. We can write the distribution of the j-component of the field in the lens plane as:

$$t^j(x,y) = \tau_0^j(x,y) \cdot \exp\Big\{ - i\frac{2\pi}{\lambda}\sqrt{f^2 + x^2 + y^2}\Big\} . \qquad (A.3)$$

The function $\tau_0^j(x,y)$ contains the incident field, the lens pupil function and possible lens aberrations. Wavefront curvature is provided by the exponential part of Eq. A.3. If $(f/\lambda)NA^2$ becomes large, the rapid oscillations of the field phase require huge spatial sampling rate, thus making the calculation impractical. Nonetheless, the fast-oscillating term can be factorized:

$$t^j(x,y) = \tau^j(x,y) \cdot \exp\Big\{ - i\frac{\pi\eta_0}{\lambda f}\Big[x^2 + y^2\Big]\Big\} , \qquad (A.4)$$

where

$$\tau^j(x,y) = \tau_0^j(x,y) \cdot \exp\Big\{ - i\frac{2\pi f}{\lambda}\Big[\sqrt{1 + \frac{x^2+y^2}{f^2}} - \frac{1}{2}\eta_0\frac{x^2+y^2}{f^2}\Big]\Big\} . \qquad (A.5)$$

The parameter η_0 is optimized in order to find out the minimum number of samples necessary in the lens plane. The optimum value η_0 is calculated by considering the exponent expression in Eq. A.5 and simply write it as:

$$\omega_\eta(r) = \sqrt{1+r^2} - \frac{1}{2}\eta r^2 , \qquad (A.6)$$

where $0 < r < R$ and $R = NA/\sqrt{1-NA^2}$. The value $\eta = \eta_0$ we are looking for minimizes the maximum value of the oscillation rate $|\omega'_\eta(r)|$. By imposing the second derivative $\omega''_\eta(r) = 0$, we find that the function $\omega'_\eta(r)$ reaches its relative maximum at $r_0 = \sqrt{\eta^{-2/3} - 1}$. Since $r \in [0, R]$, then

$$\Big(\sqrt{1 - NA^2}\Big)^3 \leq \eta \leq 1 . \qquad (A.7)$$

The curve

$$\omega'_\eta(r_0) = \big(1 - \eta^{2/3}\big)^{3/2} \qquad (A.8)$$

represents the relative maxima of the oscillation rate ω'_η for different values of η. Retrieve the absolute maximal point of a function defined over a finite interval requires that also the interval extremes must be considered. In the present case:

$$\omega'_\eta(0) = 0 \qquad (A.9)$$

$$\omega'_\eta(R) = -\eta \cdot \frac{NA}{\sqrt{1-NA^2}} + NA . \qquad (A.10)$$

In Fig. A.1, $\omega'_\eta(r_0)$ and $\omega'_\eta(R)$ for $NA = 0.65$ are plotted as functions of η. The crossing point of the two lines identifies the optimum value η_0 minimizing the maximum value of the oscillation rate of the function $\omega_\eta(r)$. Since we cannot identify η_0 analytically, approximated numerical methods are needed.

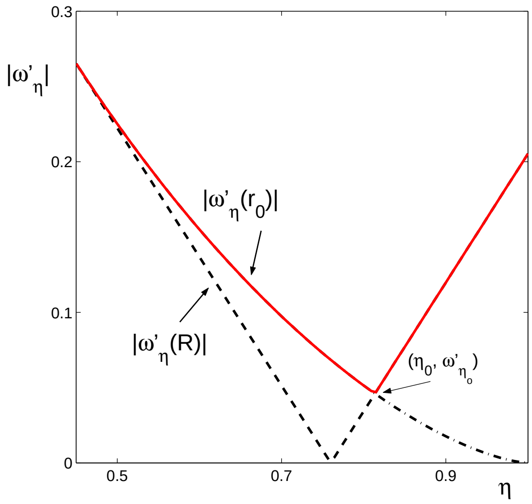

Figure A.1: Profile of the functions $\omega'_\eta(r_0)$ and $\omega'_\eta(R)$ over the interval $\eta \in \left[\left(\sqrt{1-NA^2}\right)^3, 1\right]$ for $NA = 0.65$. The solid line represents the absolute maxima points of the function ω'_η.

Once η_0 is calculated, the space domain can be properly sampled with a linear cell-size Δ given by

$$\Delta \leq \min\left\{\frac{R}{10\lambda}, \frac{1}{2\omega'_\eta 0}\right\} . \tag{A.11}$$

The Fourier transformation of the field $t^j(x,y)$ (Eq. A.4) can be expressed as a convolution of two Fourier-transformations. The Fourier-transformation of second term of expression A.4 can be carried out analytically, and the result is:

$$\begin{aligned}\lambda^{-2}\,T^j(\sigma_x,\sigma_y) = \; & -i\frac{f}{\lambda\eta_0}\exp\Big[\frac{i\pi f}{\lambda\eta_0}(\sigma_x^2+\sigma_y^2)\Big]\cdot \\ & \cdot\iint_{-\infty}^{+\infty}\mathcal{F}\{\tau^j(x,y)\}\cdot\exp\Big[i\frac{\pi\eta_0\lambda}{f}(u'^2+v'^2)\Big]\cdot \\ & \cdot\exp\Big[-i2\pi(u'\sigma_x+v'\sigma_y)\Big]\mathrm{d}u'\mathrm{d}v' \;,\end{aligned} \tag{A.12}$$

where $u = f(\lambda\eta_0)^{-1}\sigma_x$ and $v = f(\lambda\eta_0)^{-1}\sigma_y$. The previous expression can be simplified by defining:

$$h^j(u,v) = -i\frac{f}{\lambda\eta_0}\exp\Big[\frac{i\pi\eta_0\lambda}{f}(u^2+v^2)\Big]\cdot\;\mathcal{F}\{\tau^j(x,y)\}\;, \tag{A.13}$$

which gives

$$\lambda^{-2}\,T^j(\sigma_x,\sigma_y) = \exp\Big\{i2\pi\Big[\frac{f}{2\lambda\eta_0}(\sigma_x^2+\sigma_y^2)\Big]\Big\}\cdot\mathcal{F}\{h^j(u,v)\}\;. \tag{A.14}$$

The previous equation represents the angular spectrum of the field $t^j(x, y)$ and can be used directly in the integral of Eq. A.3. Nevertheless, as the incident light is focused, the corresponding electromagnetic field vector experiences a space-dependent tilt, in a way to maintain the tangential position with respect to the spherical wavefront. As a result, a converging field vector will have all the three cartesian components non-zero. In order to take this effect into account, the following functions must be involved in the calculation.

$$\Omega_{ji} = -\frac{\sigma_j \sigma_i}{1 + \sqrt{1 - \sigma_j^2 - \sigma_i^2}} \frac{1}{\sqrt{1 - \sigma_j^2 - \sigma_i^2}} \;, \tag{A.15}$$

$$\Omega_{jj} = \left(1 - \frac{\sigma_j^2}{1 + \sqrt{1 - \sigma_j^2 - \sigma_i^2}}\right) \frac{1}{\sqrt{1 - \sigma_j^2 - \sigma_i^2}}; , \tag{A.16}$$

$$\Omega_{jk} = \frac{-\sigma_j}{\sqrt{1 - \sigma_j^2 - \sigma_i^2}} \;, \tag{A.17}$$

They represent the normalized amplitudes of the field vector $\bar{t} = (t^i, t^j, t^k)$ resulting from the focalization of an incident j-polarized field. The case of an incident i-polarized light is obtained by a straightforward index permutation. The final expression of the angular spectrum to be used in Eq. A.3 is then given by

$$\lambda^{-2}\, T^j(\sigma_x, \sigma_y) \cdot \Omega_{jj} \;, \tag{A.18}$$

which allows the calculation of the j-component of a focused field having initial j-oriented polarization vector.

Appendix B

C-method for multilayered periodic structures

The innovative method (hereafter, the C-method) proposed by Chandezon *et al.* in the early eighties is a mode-matching differential method particularly suited for the rigorous analysis of corrugated periodic surfaces with smooth profiles. Over the last two decades, further development and extensions of the method have been proposed by many researcher. Among them, Popov and Mashev [117] considered the conical diffraction mounting, Inchaussandague and Depine [118] presented a generalization to anisotropic media and Preist*et al.* [119] an adaptation to overhanging profiles. Moreover, the method has been improved for the analysis of multilayered structures with constant and arbitrarily varying profiles [120, 121, 122, 123] . The extended C-method described in this appendix refers mainly to the work of Li in Ref. [106].

B.1 Notations and statement of the problem

The purpose of the proposed method is to analyze a typical 2D diffraction problem. As depicted in Fig. B.1, the periodic diffracting structure (period Λ) is composed by a stack of N media whose boundaries profiles are described by a set of $N-1$ functions $a_i(x)$, $i = 1, 2, \ldots N-1$. The structure is invariant along the z-direction. Each medium is optically characterized by a permittivity $\epsilon_i(x, y)$, $i = 1, 2, \ldots N$ that is a function of both cartesian coordinates x and y. The illuminating field is represented by a single plane wave ($k_0 = 2\pi\lambda^{-1}$ in vacuum) propagating in medium N and incident on interface $a_{N-1}(x)$ at an angle θ with respect to the y axis. In such a two-dimensional geometry, two polarization states are usually considered. In the first case, the electric field vector $\mathbf{E}$ of the electromagnetic wave has only one cartesian component, E_z, being always perpendicular to the xy plane (Transverse Electric -TE- configuration). In the second case, the magnetic field $\mathbf{H}$ is always perpendicular to the xy- plane (Transverse Magnetic -TH- configuration) and the electric field vector is described by the E_x and E_y components. In the following, the TH polarization will be considered, and the unknown field H_z to calculate will be generally indicated by $F(x, y; t)$.

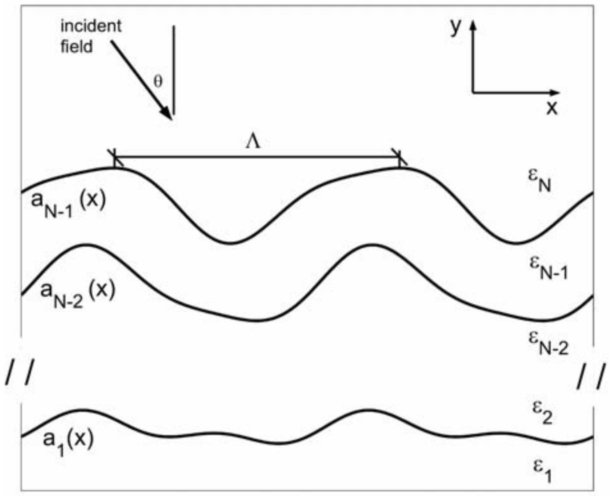

Figure B.1: Schematic of the multilayered structure considered with the C-method.

The Maxwell equations referred to a scalar, harmonic field $F(x, y; t) = F(x, y)\exp(-i\omega t)$ propagating in a inhomogeneous, non magnetic medium with no charges neither currents can be reduced to the Helmoltz equation:

$$\left(\frac{\partial^2}{\partial x^2} + \frac{\partial^2}{\partial y^2} + k_0^2\epsilon(x, y)\right) F(x, y) = 0 \tag{B.1}$$

or, more simply

$$L\left(\frac{\partial}{\partial x}, \frac{\partial}{\partial y}; x, y\right) F(x, y) = 0 \tag{B.2}$$

Solutions of equation B.2 can not be written using the well-known Rayleigh expansion formula [124] since the permittivity $\epsilon = \epsilon(x, y)$ is not space-invariant. Nevertheless, a simple form for these solutions can be obtained if the differential operator $L\left(\frac{\partial}{\partial x}, \frac{\partial}{\partial y}; x, y\right)$ is reduced to $L\left(\frac{\partial}{\partial x}, \frac{\partial}{\partial y}; x\right)$. There are at least two possibilities of reformulating the problem in such a way.

A first possibility is to split the equation B.2 into $n > N-1$ elementary problems where the permittivity can be locally considered as a function of the x coordinate only. This corresponds to cut the structure into n rectangular slices of thickness t_i $(i = 1, 2, \ldots n)$, in which the permittivity has constant value along the y direction. The accuracy of the method depends strongly on the quality of such a rectangular approximation to the real profile: better results are obtained as n increases and t_i decreases. Methods like the Fourier Modal Method (FMM) or the Rigorous Coupled Wave Analysis (RCWA) are based on this approach.

An alternative formulation requires the use of $N-1$ curvilinear coordinate transformations of the type:

$$\begin{cases} v = x \\ u_j = y - a_j(x) \qquad j = 1, 2, \ldots N-1 \end{cases} \tag{B.3}$$

In the new coordinate systems (v, u_j) , the j^{th} interface is described by a flat profile $u_j = 0$ and the two layers surrounding the interface have permittivities $\epsilon(v, u_j) = \epsilon_i \quad (i = j, j{+}1)$. We call $F^{(i,j)}$ the magnetic field H_z in medium i expressed in the coordinate system (v, u_j). The general problem B.2 is then simplified into the $2(N-1)$ elementary problems:

$$L_{i,j}\left(\frac{\partial}{\partial v}, \frac{\partial}{\partial u_j}; v\right) F^{(i,j)}(v, u_j) = 0 \qquad i = j, j+1; \quad j = 1, 2, \dots N-1 \tag{B.4}$$

As a final step, a proper mathematical connections between fields $F^{(j+1,j)}$ and $F^{(j+1,j+1)} \quad (j = 1, 2, \dots N-2)$ must be carried out. The C-method is based on this formulation of the problem.

B.2 The eigenvalue problem

Let us consider the interface $a_j(x)$ of the structure. If we apply the change of variables B.3, the $L_{i,j}$ operators become:

$$L_{i,j} = \frac{\partial^2}{\partial v^2} - 2\dot{a}_j \frac{\partial^2}{\partial v \partial u_j} - \ddot{a}_j \frac{\partial}{\partial u_j} + (1 + \dot{a}_j^2)\frac{\partial^2}{\partial u_j^2} + k_0^2 \epsilon_i \quad i = j, j+1 \tag{B.5}$$

and the Helmoltz equation B.4 in media j , $j+1$ can be rewritten as a double couple of differential equations of the first order:

$$\begin{bmatrix} k_0^2\epsilon_i + \frac{\partial^2}{\partial v^2} & 0 \\ 0 & 1 \end{bmatrix} \begin{pmatrix} F^{(i,j)} \\ f^{(i,j)} \end{pmatrix} = \begin{bmatrix} i\left(\frac{\partial}{\partial v}\dot{a}_j + \dot{a}_j \frac{\partial}{\partial v}\right) & 1 + \dot{a}_j^2 \\ 1 & 0 \end{bmatrix} \cdot \frac{1}{i}\frac{\partial}{\partial u_j} \begin{pmatrix} F^{(i,j)} \\ f^{(i,j)} \end{pmatrix} \quad i = j, j{+}1 \tag{B.6}$$

Let the fields $F^{(i,j)}(v, u_j)$ and $f^{(i,j)}(v, u_j)$ be expanded in Fourier series:

$$F^{(i,j)}(v, u_j) = \sum_{m=-\infty}^{\infty} F_m^{(i,j)}(u_j) e^{i\alpha_m v} \qquad f^{(i,j)}(v, u_j) = \sum_{m=-\infty}^{\infty} f_m^{(i,j)}(u_j) e^{i\alpha_m v} \tag{B.7}$$

where $\alpha_m = n_N k_0 \sin\theta + mK$, $n_N = \sqrt{\epsilon_N}$ and $K = 2\pi\Lambda^{-1}$. In a practical implementation, the summation over an infinite number of elements must be truncated. We will retain $2N_o{+}1$ orders, in such a way that $m \in [-N_o, N_o]$. Since the differential operators in equation B.6 do not depend explicitly on u_j, we can assume a dependence in the exponential form $\exp(i\rho u_j)$ for $F^{(i,j)}$ and $f^{(i,j)}$. As a consequence, the following transformations can be introduced:

$$\frac{\partial}{\partial v} \to i\boldsymbol{\alpha}, \qquad \frac{\partial}{\partial u_j} \to i\rho \tag{B.8}$$

and equation B.6 can be re-written in the following matrix form

$$\begin{bmatrix} \boldsymbol{\beta}^{(i)^2} & 0 \\ 0 & \mathbb{I} \end{bmatrix} \begin{pmatrix} \boldsymbol{F}^{(i,j)} \\ \boldsymbol{f}^{(i,j)} \end{pmatrix} = \rho \begin{bmatrix} -(\boldsymbol{\alpha}\dot{\boldsymbol{a}}_j + \dot{\boldsymbol{a}}_j\boldsymbol{\alpha}) & \mathbb{I} + \dot{\boldsymbol{a}}_j\dot{\boldsymbol{a}}_j \\ \mathbb{I} & 0 \end{bmatrix} \begin{pmatrix} \boldsymbol{F}^{(i,j)} \\ \boldsymbol{f}^{(i,j)} \end{pmatrix} \quad i = j, j+1 \tag{B.9}$$

where $\boldsymbol{\alpha}$ and $\boldsymbol{\beta}^{(i)}$ are diagonal matrices whose elements are α_m and $\beta_m^{(i)} = \sqrt{\epsilon_i k_0^2 - \alpha_m^2}$, $\mathrm{Re}[\beta_m^{(i)}] + \mathrm{Im}[\beta_m^{(i)}] > 0$ ($m \in [-N_o, N_o]$) respectively; $\boldsymbol{F}^{(i,j)}$ and $\boldsymbol{f}^{(i,j)}$ are column vectors containing the $2N_o + 1$ Fourier components $F_m^{(i,j)}$ and $f_m^{(i,j)}$ and $\dot{\boldsymbol{a}}_j$ is the Toeplitz antisymmetric squared matrix of the Fourier coefficients of the the function $\dot{a}_j = \frac{da_j}{dx}$:

$$(\dot{a}_j)_{mn} = \frac{1}{\Lambda} \int_0^\Lambda \dot{a}_j \, e^{-i(m-n)Kx} dx \qquad n \in [-N_o, N_o] \tag{B.10}$$

After a little algebra, it is possible to reduce the differential equations B.9 to two eigenvalues problems of the kind $B\Psi = \rho^{-1}\Psi$.

The set of $2(2N_o + 1)$ eigenvalues $\rho^{(i,j)}$ can be split into the following two groups:

$$\begin{array}{ll} \rho_p^{(i,j)+} = \rho_p^{(i,j)} & \forall p : \mathrm{Re}[\rho_p^{(i,j)}] + \mathrm{Im}[\rho_p^{(i,j)}] > 0 \\ \rho_p^{(i,j)-} = \rho_p^{(i,j)} & \forall p : \mathrm{Re}[\rho_p^{(i,j)}] + \mathrm{Im}[\rho_p^{(i,j)}] < 0 \end{array} \tag{B.11}$$

and the general solution to B.4 can be written as:

$$F_+^{(i,j)}(v, u_j) = \sum_m e^{i\alpha_m v} \sum_p \mathcal{F}_{mp}^{(i,j)+} \, e^{i\rho_p^{(i,j)+} u_j} C_p^{(i,j)+} \tag{B.12}$$

$$F_-^{(i,j)}(v, u_j) = \sum_m e^{i\alpha_m v} \sum_p \mathcal{F}_{mp}^{(i,j)-} \, e^{i\rho_p^{(i,j)-} u_j} C_p^{(i,j)-} \tag{B.13}$$

$$F^{(i,j)}(v, u_j) = F_+^{(i,j)}(v, u_j) + F_-^{(i,j)}(v, u_j) \qquad i = j\,, j+1 \tag{B.14}$$

where $C_p^{(i,j)\pm}$ is the unknown amplitude and $\mathcal{F}_{mp}^{(i,j)\pm}$ is the generic m^{th} element of the p^{th} eigenvector (associated to $\rho_p^{(i,j)\pm}$).

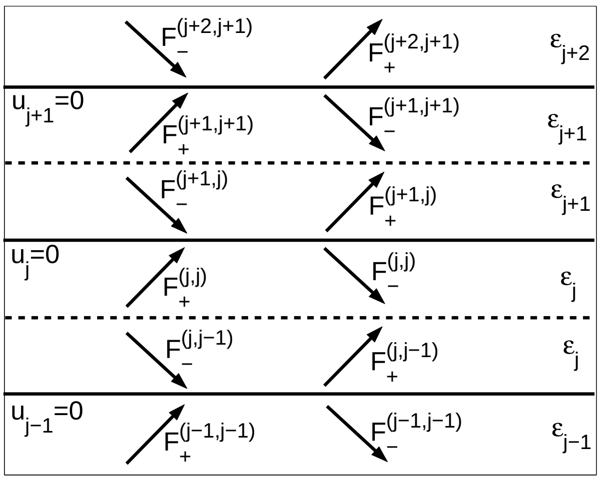

Figure B.2: Schematic representation of up-going and down-going waves in the multi-layered structure. Solid lines represent real medium boundaries, dashed lines represents fictitious interfaces where field connection must be imposed

Two terms contributes to the field $F^{(i,j)}(v, u_j)$: those terms denoted with the superscript "+" are associated to propagating or decaying waves traveling in the positive y-direction, while those denoted with the superscript "$-$" represent waves propagating or decaying in the negative y-direction. In the drawing of Fig. B.2 an intuitive representation of the fields $F_{\pm}^{(i,j)}(v,u_j)$ is shown. Once the complete set of eigenvectors has been calculated for all interfaces, boundary conditions must be imposed.

B.3 Boundary conditions and field connection

In order to determine the unknown amplitudes $C_p^{(i,j)\pm}$, the continuity of the tangential electric and magnetic fields across each interface must be imposed. $H_z(x,y)$ is always tangential to the structure profiles, then:

$$F_-^{(j,j)} + F_+^{(j,j)} = F_-^{(j+1,j)} + F_+^{(j+1,j)} \qquad j = 1, 2, \dots N-1 \tag{B.15}$$

At each interface, the tangential component $G^{(i,j)}(v,u_j)$ of the electric field is proportional to the scalar product of the tangential vector and the electric field vector:

$$G^{(i,j)}(v,u_j) = \boldsymbol{E}^{(i,j)}(v,u_j)\cdot \boldsymbol{t}^{(j)} = \boldsymbol{E}^{(i,j)}(v,u_j)\,\cdot\,\hat{\boldsymbol{x}} + \boldsymbol{E}^{(i,j)}(v,u_j)\,\cdot\,\dot{a}_j\hat{\boldsymbol{y}} \tag{B.16}$$

where

$$\boldsymbol{E}^{(i,j)}(v,u_j) = \left(\frac{i\eta_0}{k_0\epsilon_i}\frac{\partial F^{(i,j)}}{\partial y}\,,-\frac{i\eta_0}{k_0\epsilon_i}\frac{\partial F^{(i,j)}}{\partial x}\,,0\right)\;;\qquad \eta_0 = \sqrt{\frac{\mu_0}{\epsilon_0}} \tag{B.17}$$

which gives

$$G^{(i,j)}(v,u_j) = -\frac{i\eta_0}{k_0\epsilon_i}\left[\dot{a}_j\frac{\partial F^{(i,j)}}{\partial v} - (1+\dot{a}_j^2)\frac{\partial F^{(i,j)}}{\partial u_j}\right] \tag{B.18}$$

For symmetry reasons, it is preferable to write $G^{(i,j)}$ in a form similar to B.14:

$$G^{(i,j)}(v,u_j) = G_+^{(i,j)}(v,u_j) + G_-^{(i,j)}(v,u_j) \qquad i = j\,,j+1 \tag{B.19}$$

with

$$G_{\pm}^{(i,j)}(v,u_j) = \sum_m e^{i\alpha_m v}\sum_p \mathcal{G}_{mp}^{(i,j)\pm}\,e^{i\rho_p^{(i,j)\pm}u_j}C_p^{(i,j)\pm} \tag{B.20}$$

and

$$\mathcal{G}_{mp}^{(i,j)\pm} = \frac{\eta_0}{k_0\epsilon_i}\left(\sum_{n=-N_o}^{N_o}(\dot{a}_j)_{mn}\cdot\alpha_n\mathcal{F}_{np}^{(i,j)\pm} - \left(\delta_{mn} + (\dot{a}_j\cdot\dot{a}_j)_{mn}\right)\rho_p^{(i,j)}\mathcal{F}_{np}^{(i,j)\pm}\right) \tag{B.21}$$

The continuity condition for the tangential electric field is, then:

$$G_-^{(j,j)} + G_+^{(j,j)} = G_-^{(j+1,j)} + G_+^{(j+1,j)} \qquad j = 1, 2, \dots N-1 \tag{B.22}$$

The fields continuity conditions can be expressed using a scattering-matrix formalism. After having defined

$$s^{(j)} = \begin{pmatrix} \boldsymbol{\mathcal{F}}^{(j+1,j)+} & -\boldsymbol{\mathcal{F}}^{(j,j)-} \\ \boldsymbol{\mathcal{G}}^{(j+1,j)+} & -\boldsymbol{\mathcal{G}}^{(j,j)-} \end{pmatrix}^{-1} \begin{pmatrix} \boldsymbol{\mathcal{F}}^{(j,j)+} & -\boldsymbol{\mathcal{F}}^{(j+1,j)-} \\ \boldsymbol{\mathcal{G}}^{(j,j)+} & -\boldsymbol{\mathcal{G}}^{(j+1,j)-} \end{pmatrix} \tag{B.23}$$

equations B.15 and B.22 are summarized in the following relation

$$\begin{pmatrix} \boldsymbol{C}^{(j+1,j)+} \\ \boldsymbol{C}^{(j,j)-} \end{pmatrix} = s^{(j)} \begin{pmatrix} \boldsymbol{C}^{(j,j)+} \\ \boldsymbol{C}^{(j+1,j)-} \end{pmatrix} \qquad j = 1, 2, \dots N-1 \tag{B.24}$$

Fields $F^{(j,j)}(v, u_j)$ and $F^{(j,j-1)}(v, u_{j-1})$ are defined over the same spatial region having permittiviy ϵ_j ($j = 2, 3, \dots N-1$). Nonetheless, they are expressed by means of two different coordinate systems. A connection between these two fields is, then, required. In order to deal with this problem, Granet et al. [123] proposed the following assumption: for any (v, u_j) and (v, u_{j-1}) describing the same point in the j^{th} layer:

$$F_{\pm}^{(j,j)}(v, u_j) = F_{\pm}^{(j,j-1)}(v, u_{j-1}) \tag{B.25}$$

If the two couples of coordinates (v, u_j) and (v, u_{j-1}) describe the same point, we have:

$$u_j + a_j(x) = u_{j-1} + a_{j-1}(x) \tag{B.26}$$

In particular, in the (v, u_{j-1}) coordinate system, the points along interface $u_j = 0$ are identified by $u_{j-1} = a_j(x) - a_{j-1}(x)$, while the points along interface $u_{j-1} = 0$ are described by $u_j = a_{j-1}(x) - a_j(x)$ in the (v, u_j) coordinate system. The fields connection relation in medium j can be expressed as

$$F_{+}^{(j,j)}(v, 0) = F_{+}^{(j,j-1)}(v, a_j - a_{j-1}) = \sum_m e^{i\alpha_m v} \sum_p \mathcal{F}_{mp}^{(j,j-1)+} \, e^{i\rho_p^{(j,j-1)+}(a_j - a_{j-1})} C_p^{(j,j-1)+} \tag{B.27}$$

$$F_{-}^{(j,j-1)}(v, 0) = F_{-}^{(j,j)}(v, a_{j-1} - a_j) = \sum_m e^{i\alpha_m v} \sum_p \mathcal{F}_{mp}^{(j,j)-} \, e^{i\rho_p^{(j,j)-}(a_{j-1} - a_j)} C_p^{(j,j)-} \tag{B.28}$$

In order to reduce the previous expressions to a simpler form, we build the following rank-2 tensors, formed by the Fourier coefficients

$$\left[L^{(j,j-1)+}\right]_{mlp} = \frac{1}{\Lambda} \int_0^{\Lambda} e^{i\rho_p^{(j,j-1)+}(a_j - a_{j-1})} \, e^{-i(m-l)Kx} dx\,; \quad l \in [-N_o, N_o] \tag{B.29}$$

$$\left[L^{(j,j)-}\right]_{mlp} = \frac{1}{\Lambda} \int_0^{\Lambda} e^{i\rho_p^{(j,j)-}(a_{j-1} - a_j)} \, e^{-i(m-l)Kx} dx\,; \qquad l \in [-N_o, N_o] \tag{B.30}$$

The previous expressions can be interpreted as two stacks of $2N_o + 1$ Toeplitz matrices. With the help of tensors B.29 and B.30, we can write a linear transformation of eigenvectors $\mathcal{F}_{mp}^{(j,j-1)+}$ and $\mathcal{F}_{mp}^{(j,j)-}$:

$$\tilde{\mathcal{F}}_{mp}^{(j,j-1)+} = \sum_l \left[L^{(j,j-1)+}\right]_{mlp} \mathcal{F}_{mp}^{(j,j-1)+} \tag{B.31}$$

$$\tilde{\mathcal{F}}_{mp}^{(j,j)-} = \sum_l \left[L^{(j,j)-}\right]_{mlp} \mathcal{F}_{mp}^{(j,j)-} \tag{B.32}$$

which allow us to re-write equations B.27 and B.28 in the following compact form:

$$F_+^{(j,j)}(v,0) = \sum_m e^{i\alpha_m v} \sum_p \mathcal{F}_{mp}^{(j,j-1)+} e^{i\rho_p^{(j,j-1)+}(0)} C_p^{(j,j-1)+} = \tilde{F}_+^{(j,j-1)}(v,0) \tag{B.33}$$

$$F_-^{(j,j-1)}(v,0) = \sum_m e^{i\alpha_m v} \sum_p \mathcal{F}_{mp}^{(j,j)-} e^{i\rho_p^{(j,j)-}(0)} C_p^{(j,j)-} = \tilde{F}_-^{(j,j)}(v,0) \tag{B.34}$$

In a scattering-matrix formalism, expressions B.33 and B.34 can be written as

$$\begin{pmatrix} \boldsymbol{C}^{(j,j)+} \\ \boldsymbol{C}^{(j,j-1)-} \end{pmatrix} = t^{(j)} \begin{pmatrix} \boldsymbol{C}^{(j,j-1)+} \\ \boldsymbol{C}^{(j,j)-} \end{pmatrix} \qquad j = 2, 3, \ldots N-1 \tag{B.35}$$

with

$$t^{(j)} = \begin{pmatrix} \boldsymbol{\mathcal{F}}^{(j,j)+} & 0 \\ 0 & -\boldsymbol{\mathcal{F}}^{(j,j-1)-} \end{pmatrix}^{-1} \begin{pmatrix} \tilde{\boldsymbol{\mathcal{F}}}^{(j,j-1)+} & 0 \\ 0 & -\tilde{\boldsymbol{\mathcal{F}}}^{(j,j)-} \end{pmatrix} \tag{B.36}$$

The final step is to cascade all the scattering matrices $s^{(j)}$ and $t^{(j)}$:

$$j = N-1\,\text{interface} \qquad \begin{pmatrix} \boldsymbol{C}^{(N,N-1)+} \\ \boldsymbol{C}^{(N-1,N-1)-} \end{pmatrix} = s^{(N-1)} \begin{pmatrix} \boldsymbol{C}^{(N-1,N-1)+} \\ \boldsymbol{C}^{(N,N-1)-} \end{pmatrix}$$

$$j = N-1\,\text{medium} \qquad \begin{pmatrix} \boldsymbol{C}^{(N-1,N-1)+} \\ \boldsymbol{C}^{(N-1,N-2)-} \end{pmatrix} = t^{(N-1)} \begin{pmatrix} \boldsymbol{C}^{(N-1,N-2)+} \\ \boldsymbol{C}^{(N-1,N-1)-} \end{pmatrix}$$

$$j = N-2\,\text{interface} \qquad \begin{pmatrix} \boldsymbol{C}^{(N-1,N-2)+} \\ \boldsymbol{C}^{(N-2,N-2)-} \end{pmatrix} = s^{(N-2)} \begin{pmatrix} \boldsymbol{C}^{(N-2,N-2)+} \\ \boldsymbol{C}^{(N-1,N-2)-} \end{pmatrix}$$

. . . .

$$j = 2\,\text{medium} \qquad \begin{pmatrix} \boldsymbol{C}^{(2,2)+} \\ \boldsymbol{C}^{(2,1)-} \end{pmatrix} = t^{(2)} \begin{pmatrix} \boldsymbol{C}^{(2,1)+} \\ \boldsymbol{C}^{(2,2)-} \end{pmatrix}$$

$$j = 1\,\text{interface} \qquad \begin{pmatrix} \boldsymbol{C}^{(2,1)+} \\ \boldsymbol{C}^{(1,1)-} \end{pmatrix} = s^{(1)} \begin{pmatrix} \boldsymbol{C}^{(1,1)+} \\ \boldsymbol{C}^{(2,1)-} \end{pmatrix}$$

With some matrix algebra, it is possible to collapse all these matrices into a $2(2N_o+1) \times 2(2N_o+1)$ one, called *scattering matrix of the system* $\boldsymbol{S}$.

$$\begin{pmatrix} \boldsymbol{C}^{(\,N,\,N-1)+} \\ \boldsymbol{C}^{(\,1,\,1)-} \end{pmatrix} = \boldsymbol{S} \begin{pmatrix} \boldsymbol{C}^{(\,1,\,1)+} \\ \boldsymbol{C}^{(\,N,\,N-1)-} \end{pmatrix} \tag{B.37}$$

The amplitudes $C^{(\,1,\,1)+}$ and $C^{(\,N,\,N-1)-}$ represent the input of the scattering problem. In particular, $C^{(\,1,\,1)+} = 0$ since the structure is not illuminated from the bottom. Moreover, the incident field at interface $N-1$ expressed in the coordinate system (v, u_{N-1}) is $\psi = \exp\left(in_N k_0 \sin\theta v\right) \cdot \exp\left(in_N k_0 \cos\theta a_{N-1}(x)\right)$ and must be expressed in the base of eigenvectors $\boldsymbol{\mathcal{F}}^{(\,N,\,N-1)-}$. This is readily done if we consider the Fourier decomposition of ψ:

$$\psi = \sum_m P_m e^{i\alpha_m v} \qquad \text{with} \quad P_m = \frac{1}{\Lambda} \int_0^{\Lambda} e^{in_N k_0 \cos\theta a_{N-1}} \, e^{-imKx} dv \tag{B.38}$$

and defining the matrix $\boldsymbol{\mathcal{F}}^{(\,N,\,N-1)-}$ with only one non-zero column:

$$\left[\boldsymbol{\mathcal{F}}^{(\,N,\,N-1)-}\right]_{m1} = P_m \tag{B.39}$$

By using the last representation of $\boldsymbol{\mathcal{F}}^{(\,N,\,N-1)-}$ in the definition of the scattering matrix $s^{(N-1)}$, the presence of the incident field can be taken into account by setting $C^{(\,N,\,N-1)-} = 1$. The linear system of equations B.37 is now completely defined. Once the solutions $C^{(\,N,\,N-1)+}$ and $C^{(\,1,\,1)-}$ are found, a classical iteration method can be used for the calculation of the whole set of amplitude values $C^{(\,j,\,i)\pm}$ $(i = j, j+1)$.

Bibliography

[1] C. M. Sparrow, "On spectroscopic resolving power", Astrophys. J. **44**, 76–86 (1916).

[2] Lord Rayleigh, "On the theory of optical images, with special reference to the microscope", Phil. Mag. **54**, 167 (1896).

[3] E. Abbe, "Beiträge zur Theorie des Mikroskops und der mikroskopischen Wahrnehmung", Archiv. Mikrosk. Anat. **9**, 413–468 (1873).

[4] J. M. Vigoureux and D. Courjon, "Detection of nonradiative fields in light of the Heisemberg uncertainty principle and the Rayleigh criterion", App. Opt. **31**, 3170–3177 (1992).

[5] I. J. Cox and C. J. R. Sheppard, "Information capacity and resolution in an optical system", J. Opt. Soc. Am. A **3**, 1152–1158 (1986).

[6] I. Ichimura, S. Hayashi and G. S. Kino, "High density optical recording using a solid immersion lens", App. Opt. **36**, 4339–4348 (1997).

[7] G. Indebetouw, A. El Maghnouji and R. Foster, "Scanning holographic microscopy with transverse resolution exceeding the Rayleigh limit and extended depth of focus", J. Opt. Soc. Am. A **22**, 892–898 (2005).

[8] S. W. Hell and J. Wichmann, "Breaking the diffraction resolution limit by stimulated emission: stimulated-emission-depletion fluorescence microscopy ", Opt. Lett. **19**, 780–782 (1994).

[9] J. W. Goodman, *Introduction to Fourier optics*, (McGraw Hill, San Fancisco, Calif., 1968).

[10] E. H. Synge, "A suggested method for extending microscopic resolution into the ultra-microscopic region", Phil. Mag. **6**, 356–362 (1928).

[11] E. Betzig, M. Isaacson and A. Lewis, "Collection mode near-field scanning optical microscopy", Appl. Phys. Lett. **51**, 2088–2090 (1987).

[12] J. Grochmalicki and E. R. Pike, "Superresolution for digital versatile discs", App. Opt. **39**, 6341–6349 (2000).

[13] G. Bouwhuis, J. Braat, A. Huijser, J. Pasman, G. van Rosmalen and K. Shouhamer Immink, *Principles of Optical Disc Systems*, (Adam Hilger, Bristol, UK, 1985).

[14] T. Wilson and C. Sheppard, *Theory and practice of scanning microscopy*, (Acad. Press, London, UK, 1984).

[15] M. A. A. Neil, R. Juŝkaitis, T. Wilson and Z. J. Laczik, “Optimized pupil-plane filters for confocal microscope point-spread function engineering”, Opt. Lett. **25**, 245–247 (2000).

[16] T. R. M. Sales and G. M. Morris, “Fundamental limits of optical superresolution”, Opt. Lett. **22**, 582–584 (1997).

[17] G. Toraldo di Francia, “Super-gain antennas and optical resolving power”, Nuovo Cimento Suppl. **9**, 426–438 (1952).

[18] B. R. Frieden, “On arbitrary perfect imagery with a finite aperture”, Opt. Acta **16**, 795–807 (1969).

[19] G. Boyer and M. Sechaud, “Super-resolution by Taylor filters”, Appl. Opt. **12**, 893–894 (1973).

[20] A. Lewis, M. Isaacson, A. Harooutian and A. Muray, “Development of a 500 Å spatial resolution light microscope”, Ultramicroscopy **13**, 227–231 (1984).

[21] D. W. Pohl, W. Denk and M. Lanz, “Optical stethoscopy: image recording with resolution $\lambda/20$”, Appl. Phys. Lett. **44**, 651–653 (1984).

[22] M. Totzeck and H. J. Tiziani, “Interference microscopy of sub-λ structures: a rigorous computation method and measurements”, Opt. Comm. **136**, 61–74 (1997).

[23] J. D. Jackson, *Classical Electrodynamics*, 2nd ed., (Wiley, New York, New York, 1975).

[24] E. Meyer, H. J. Hug and R. Bennewitz, *Scanning probe microscopy*, (Springer, Berlin, Germany, 2003).

[25] G. Binnig, C. F. Quate and C. Gerber, “Atomic Force Microscope”, Phys. Rev. Lett. **56**, 930–933 (1986).

[26] N. F. van Hulst, M. H. P. Moers, O. F. J. Noordman, R. G. Tack, F. B. Segerink and B. Bölger, “Near-field optical microscope using a silicon-nitride probe”, Appl. Phys. Lett. **62**, 461–463 (1993).

[27] N. F. van Hulst, M. H. P. Moers and B. Bölger, “Near-field optical microscopy in transmission and reflection modes in combination with force microscopy”, J. Microscopy **171**, 95–104 (1993).

[28] A. G. T. Ruiter, M. H. P. Moers, M. de Boer and N. F. van Hulst, “Microfabrication of near-field probes”, J. Vac. Sci. Technol. B **14**, 597–601 (1996).

[29] C. Mihalcea, W. Scholz, S. Werner, S. Münster, E. Oesterschulze and R. Kassing, “ Multipurpose sensor tips for scanning near-field microscopy ”, Appl. Phys. Lett. **68**, 3531–3533 (1996)

[30] M. Stopka, D. Drews, K. Mayr, M. Lacher, W. Ehrfeld, T. Kalkbrenner, M. Graf, V. Sandoghdar and J. Mlynek, "Multifunctional AFM/SNOM cantilever probes: fabrication and measurements", Micr. Eng. **53**, 183–186 (2000).

[31] G. Schürmann, W. Noell, U. Staufer, N. F. de Rooij, R. Eckert, J. M. Freyland and H. Heinzelmann, "Fabrication and characterization of a silicon cantilever probe with an integrated quartz-glass (fused silica) tip for scanning near-field optical microscopy", App. Opt. **40**, 5040–5045 (2001).

[32] L. Aeschimann, T. Akiyama, U. Staufer, N. F. de Rooij, L. Thiery, R. Eckert and H. Heinzelmann, "Characterization and fabrication of fully metal-coated scanning near-field optical microscopy SiO_2 tips", J. Microscopy **209**, 182–187 (2003).

[33] U. C. Fischer, H. P. Zingsheim, "Submicroscopic pattern replication with visible light", J. Vac. Sci. **19**, 881–885 (1981).

[34] B. Hecht, H. Bielefeldt, Y. Inouye, D. Pohl and L. Novotny, "Facts and artifacts in near-field optical microscopy", J. Appl. Phys. **81**, 2492–2492 (1996).

[35] A. Nesci, *Measuring amplitude and phase in optical fields with sub-wavelength features*, (UFO Atelier für Gestaltung & Verlag, Allensbach, Germany, 2001)

[36] H. K. Wickramasinghe and C. C. Williams, "Apertureless Near Field Optical Microscope", US Patent 4,947,034 (April 28, 1989).

[37] F. Zenhausern, M. P. O'Boyle and H. K. Wickramasinghe, Apertureless near-field optical microscope, Appl. Phys. Lett. **65**, 1623–1625 (1994).

[38] A. Bouhelier, M. R. Beversluis and L. Novotny, "Near-field scattering of longitudinal fields," Appl. Phys. Lett. **82**, 4596–4598 (2003).

[39] E. Descrovi, L. Vaccaro, W. Nakagawa, L. Aeschimann, U. Staufer and H. P. Herzig, "Collection of transverse and longitudinal fields by means of apertureless nanoprobes with different metal coating characteristics," Appl. Phys. Lett. **85**, 5340–5342 (2004).

[40] R. Eckert, J. M. Freyland, H. Gersen, H. Heinzelmann, G. Schürmann, W. Noell, U. Staufer and N. F. de Rooji, "Near-field fluorescence imaging with 32 nm resolution based on microfabricated cantilevered probes", Appl. Phys. Lett. **77**, 3695–3697 (2000).

[41] K. S. Youngworth and T. G. Brown, "Focusing of high numerical aperture cylindrical-vector beams", Opt. Express **7**, 77–87 (2000).

[42] M. A. Lieb and A. J. Meixner, "A high numerical aperture parabolic mirror as imaging device for confocal microscopy", Opt. Express **8**, 458–474 (2001).

[43] R. Dorn, S. Quabis and G. Leuchs, "Sharper focus for a radially polarized light beam", Phys. Rev. Lett. **91**, 233901 (2003).

[44] R. Oron, S. Blit, N. Davidson, A. A. Friesem, Z. Bomzom and E. Hasman, "The formation of laser beams with pure azimuthal or radial polarization", Appl. Phys. Lett. **77**, 3322–3324 (2000).

[45] Z. Bomzon, V. Kleiner and E. Hasman, "Formation of radially and azimuthally polarized light using space-variant subwavelength metal stripe gratings", Appl. Phys. Lett. **79**, 1587–1598 (2001).

[46] Z. Bomzon, G. Biener, V. Kleiner and E. Hasman, "Radially and azimuthally polarized beams generated by space-variant dielectric subwavelength gratings", Opt. Lett. **27**, 285–287 (2002).

[47] U. Levy, C. Tsai, L. Pang and Y. Fainman, "Engineering space-variant inhomogeneous media for polarization control ", Opt. Lett. **29**, 1718–1720 (2004).

[48] S. C. Tidwell, D. H. Ford and W. D. Kimura, "Generating radially polarized beams interferometrically", App. Opt. **29**, 2234–2239 (1990).

[49] S. C. Tidwell, G. H. Kim and W. D. Kimura, "Efficient radially polarized laser beam with a double interferometer", App. Opt. **32**, 5222–5229 (1993).

[50] M. Stalder and M. Schadt, "Linearly polarized light with axial symmetry generated by liquid-crystal polarization converters", Opt. Lett. **21**, 1948–1950 (1996).

[51] M. Stalder and M. Schadt, "Polarisation converters based on liquid crystal devices", Mol. Cryst. Liq. Cryst. **282**, 343–353 (1996).

[52] S. Masuda, T. Nose, R. Yamaguchi and S. Sato, "Polarisation converting devices using a UV curable liquid crystal", SPIE **2873**, 301–304 (1996).

[53] C. H. Gooch and H. A. Tarry, "The optical properties of twisted nematic liquid crystal structures with twist angles $\leq$ 90 degrees", J. Phys. D **8**, 1575–1584 (1975).

[54] M. Schadt and W. Helfrich, "Voltage-dependent optical activity of a twisted nematic liquid crystal", Appl. Phys. Lett. **18**, 127–129 (1971).

[55] R. Clark Jones, "A new calculus for the treatment of optical systems", J. Opt. Soc. Am. **31**, 488–503 (1941).

[56] M. Mansuripur, "Distribution of light at and near the focus of high-numerical-aperture objectives", J. Opt. Soc. Am. A **3**, 2086–2093 (1986).

[57] M. Mansuripur, "Certain computational aspects of vector diffraction problems", J. Opt. Soc. Am. A **6**, 786–805 (1989); **10** (1993).

[58] T. Grosjean and D. Courjon, "Polarization filtering by imaging systems: effect on image structure", Phys. Rev. E **67**, 46611–46616 (2003).

[59] C. Rockstuhl, M. Salt, H. P. Herzig, "Theoretical and experimental investigations of phase singularities generated by optical micro- and nano-structures", J. Opt. A **6**, S271–S276 (2004).

[60] R. Dändliker, I. Märki, M. Salt and A. Nesci, “Measuring optical phase singularities at subwavelength resolution”, J. Opt. A **6**, S189–S196 (2004).

[61] C. Rockstuhl, A. A. Ivanovskyy, M. S. Soskin, M. Salt, H. P. Herzig and R. Dändliker “High-resolution measurement of phase singularities produced by computer-generated holograms”, Opt. Comm. **242**, 163–169 (2004).

[62] P. Hariharan, B. F. Oreb, and T. Eiju, “Digital phase-shifting interferometry: a simple error-compensating phase calculation algorithm”, App. Opt. **26**, 2504–2506 (1987).

[63] J. F. Nye and M. V. Berry, “Dislocations in wave trains”, Proc. R. Soc., **A 336**, 165–190 (1974).

[64] R. H. Jordan and D. G. Hall, “Free-space azimuthal paraxial wave equation: the azimuthal Bessel-Gauss beam solution”, Opt. Lett. **19**, 427–429 (1994).

[65] D. G. Hall, “Vector-beam solutions of Maxwell’s wave equation ”, Opt. Lett. **21**, 9–11 (1995).

[66] S. K. Rhodes, K. A. Nugent and A. Roberts, “Precision measurements of the electromagnetic fields in the focal region of a high-numerical-aperture lens using a tapered fiber probe ”, J. Opt. Soc. Am. A **19**, 1689–1693 (2002).

[67] M. Madou, *Fundamentals of microfabrication*, (CRC Presss LLC, Boca Raton, Florida, 1997).

[68] P. Kramper, M. Kafesaki, C. M. Soukoulis, A. Birner, F. M. Gösele, U. Gösele, R. B. Wehspohn, J. Mlynek and V. Sandoghdar, “Near-field visualization of light confinement in a photonic crystal microresonator”, Opt. Lett. **29**, 174–176 (2004).

[69] O. J. F. Martin and C. Girard, “Controlling and tuning strong optical field gradients at a local microscope probe apex”, Appl. Phys. Lett. **70**, 705–707 (1996).

[70] F. Keilmann, “Surace-polariton propagation for scanning near-field optical microscopy application”, J. Microscopy **194**, 567–570 (1999).

[71] L. Vaccaro, L. Aeschimann, U. Staufer, H. P. Herzig and R. Dändliker, “Propagation of the electromagnetic field in fully coated near-field optical probes”, Appl. Phys. Lett. **83**, 584–586 (2003).

[72] L. Novotny, D. W. Pohl and B. Hecht, “Scanning near-field optical probe with ultrasmall spot size,” Opt. Lett. **20,** 970–972 (1995).

[73] T. Yatsui, M. Kourogi and M. Ohtsu, “Highly efficient excitation of optical near-field on an apertured fiber probe with an asymmetric structure”, Appl. Phys. Lett. **71**, 1756–1758 (1997).

[74] T. I. Kuznetsova, V. S. Lebedev and A. M. Tsvelik, "Optical fields inside a conical waveguide with a subwavelength-sized exit hole", J. Opt. A: Pure Appl. Opt. **6**, 338–348 (2004).

[75] L. Novotny and C. Hafner, "Light propagation in a cylindrical waveguide with a complex, metallic, dielectric function," Phys. Rev. E **50,** 4094–4106 (1994).

[76] B. Hecht, B. Sick, U. P. Wild, V. Deckert, R. Zenobi, O. J. F. Martin and D. W. Pohl, "Scanning near-field optical microscopy with aperture probes: fundamentals and applications," J. Chem. Phys. **112,** 7761–7774 (2000).

[77] G. H. Owyang, *Foundations of optical waveguides*, (Elsevier North Holland, New York, New York, 1981).

[78] R. F. Harrington, *Time-Harmonic Electromagnetic Fields*, (McGraw Hill, New York, New York, 1961).

[79] O. J. F. Martin and M. Paulus, "Influence of metal roughness on the near-field generated by an aperture/apertureless probe", J. Microscopy **205**, 147–152 (2001).

[80] A. Bouhelier, J. Renger, M. R. Beversluis and L. Novotny, "Plasmon-coupled tip-enhanced near-field optical microscopy", J. Microscopy **210**, 220–224 (2002).

[81] M. I. Bakunov, S. B Bodrov and M. Hangyo, "Intermode conversion in a near-field optical fiber probe", J. Appl. Phys. **96**, 1775–1780 (2004).

[82] B. Sick, B. Hecht, U. P. Wild and L. Novotny, "Probing confined fields with single molecules and viceversa", J. Microscopy **202**, 365–373 (2001).

[83] L. Novotny, M. R. Beversluis, K. S. Youngworth and T. G. Brown, "Longitudinal fields modes probed by single molecules", Phys. Rev. Lett. **86**, 5251–5253 (2001).

[84] E. Descrovi, L. Vaccaro, L. Aeschimann, W. Nakagawa, U. Staufer and H. P. Herzig, "Optical properties of microfabricated fully metal-coated near-field probes in collection mode," J. Opt. Soc. Am. A, **22**, 1432-1441 (2005).

[85] T. Yatsui, K. Itsumi, M. Kourogi and M. Ohtsu, "Metallized pyramidal silicon probe with extremely high throughput and resolution capability for optical near-field technology", Appl. Phys. Lett. **80**, 2257–2259 (2002).

[86] L. Novotny, E. J. Sánchez and X. S. Xie, "Near-field imaging using metal tips illuminated by higher-order Hermite-Gaussian beams," Ultramicroscopy **71,** 21–29 (1998).

[87] E. Betzig and J. K. Trautman, T. D. Harris, J. S. Weiner and R. L. Kostelak, "Breaking the diffraction barrier: optical microscopy on a nanometric scale," Science **251,** 1468–1470 (1991).

[88] L. Aeschimann, L. Vaccaro, T. Akiyama, U. Staufer, N. F. de Rooij, R. Eckert and H. Heinzelmann, "Polarization properties of fully metal coated scanning near-field optical microscopy probes", AIP Conf. Proc. **696**, 906–910 (2003).

[89] T. Grosjean and D. Courjon, "Immaterial tip concept by light confinement," J. Microsc. **202**, 273–278 (2000).

[90] T. Grosjean, D. Courjon and D. Van Labeke, "Bessel beams as virtual tips for near-field optics," J. Microsc. **210**, 319–323 (2003).

[91] Tao Hong, Jia Wang, Liqun Sun and Dacheng Li, "Numerical simulation analysis of a near-field optical virtual probe," Appl. Phys. Lett. **81**, 3452–3454 (2002).

[92] W. L. Barnes, A. Dereux and T. W. Ebbesen, "Surface plasmon subwavelength optics," Nature (London) **424**, 824–830 (2003).

[93] W. L. Barnes, S. C. Kitson, T. W. Preist and J. R. Sambles, "Photonic surfaces for surface-plasmon polaritons," J. Opt. Soc. Am A **14**, 1654–1661 (1997).

[94] S. C. Kitson, W. L. Barnes and J. R. Sambles, "Full photonic band gap for surface modes in the visible," Phys. Rev. Lett. **77**, 1670–2673 (1996).

[95] S. I. Bozhevolnyi, J. Erland, K. Leosson, P. M. W. Skovgaard and J. M. Hvam, "Waveguiding in surface plasmon polariton band gap structures," Phys. Rev. Lett. **86**, 3008–3011 (2001).

[96] T. Okamoto, F. H́Dhili and S. Kawata, "Towards plasmonic band gap laser," Appl. Phys. Lett. **85**, 3978–3970 (2004).

[97] A. Bouhelier, T. Huser, H. Tamaru, H. J. Güntherodt, D. W. Pohl, Fadi I. Baida and D. Van Labeke, "Plasmon optics of structured silver films," Phys. Rev. B **63**, 155404-1–155404-9 (2001).

[98] H. Ditlabacher, J. R. Krenn, G. Schider, A. Leitner and F. R. Aussenegg, "Two-dimensional optics with surface plasmon polaritons," Appl. Phys. Lett. **81**, 1762–1764 (2002).

[99] D. C. Skigin and R. A. Depine, "Surface shape resonances and surface plasmon polariton excitations in bottle-shaped metallic gratings," Phys. Rev. E **63**, 046608-1–046608-10 (2001).

[100] S. C. Kitson, W. L. Barnes and J. R. Sambles, "Photonic band gaps in metallic microcavities," J. Appl. Phys. **84**, 2399–2403 (1998).

[101] K. M. Engenhardt and S. Gregory, "Surface-plasmon-polariton excitation of optical microcavities and second-harmonic emission," J. Opt. Soc. Am. B **17**, 593–599 (2000).

[102] P. André, F. Charra and M. P. Pileni, "Resonant electromagnetic field cavity between scanning tunneling microscope tips and substrate," J. Appl. Phys. **91**, 3028–3036 (2002).

[103] T. Okamoto, T. Kobayashi and I. Yamaguchi, "Local plasmon sensor with gold colloid monolayers deposited upon glass subtrates," Opt. Lett. **25**, 372–374 (2000).

[104] C. Rockstuhl, M. Salt and H. P. Herzig, "Analyzing the scattering properties of coupled metallic nano-particles," J. Opt. Soc. Am. A, **21**, 1761–1768 (2004)

[105] L. Li, J. Chandezon, G. Granet and J. P. Plumey, "Rigorous and efficient grating-analysis method made easy for optical engineers," App. Opt. **38**, 304–313 (1999).

[106] L. Li, G. Granet, J. P. Plumey and J. Chandezon, "Some topics in extending the C method to multilayer gratings of different profiles," Pure Appl. Opt. **5**, 141–156 (1996).

[107] W. L. Barnes, T. W. Preist, S. C. Kitson, J. R. Sambles, "Physical origin of photonic energy gaps in the propagation of surface plasmons on gratings," Phys. Rev. B **54,** 6227–6244 (1996).

[108] W. L. Barnes, T. W. Preist, S. C. Kitson, J. R. Sambles, N. P. K. Cotter and D. J. Nash, "Photonic gaps in the dispersion of surface plasmons on gratings," Phys. Rev. B **51,** 11164–11167 (1995).

[109] W.-C. Tan, T. W. Preist, J. R. Sambles, M. B. Sobnack and N. P. Wanstall, "Calculation of photonic band structures of periodic multilayer grating systems by use of a curvilinear coordinate transformation", J. Opt. Soc. Am. A **15**, 2365–2372 (1998).

[110] P. B. Johnson and R. W. Christy, "Optical constants of the noble metals," Phys. Rev. B **6,** 4370–4379 (1972).

[111] J. R. Krenn, H. Ditlbacher, G. Schider, A. Hoheanau, A. Leitner and F. R. Aussenegg, "Surface plasmon micro and nano-optics," J. Microsc. **209,** 167–172 (2002).

[112] B. Fisher, T. M. Fisher and W. Knoll, "Dispersion of surface plasmons in rectangular, sinusoidal and inchoerent silver gratings," J. Appl. Phys. **75,** 1577–1581 (1994).

[113] E. Silberstein, P. Lalanne, J. P. Hugonin and Q. Cao, "Use of gratings theories in integrated optics," J. Opt. Soc. Am. A **18**, 2865–2875 (2001)

[114] D. Peyrade, E. Silberstein, P. Lalanne, A. Talneau and Y. Chen, "Short Bragg mirrors with adiabatic modal conversion," Appl. Phys. Lett. **81,** 829–831 (2002).

[115] L. Aeschimann, *Apertureless Scanning Near-field Optical Microscope probe for transmission mode operation*, (UFO Atelier für Gestaltung & Verlag, Allensbach, Germany, 2004)

[116] R. K. Luneberg, *Mathematical Theory of Optics*, (University of California Press, Berkeley and Los Angeles, Calif., 1964), pp. 319–320.

[117] E. Popov and L. Mashev, “Conical diffraction mounting generalization of a rigorous differential method”, J. Opt. **17**, 175–180 (1986).

[118] M. E. inchaussandague and R. A. Depine, “Rigorous vector theory for diffraction from gratings made of biaxial crystals”, J. Mod. Opt. **44**, 1–27 (1997).

[119] T. W. Preist, J. B. Harris, N. P. Wanstall and J. R. Sambles, “Optical response of blazed and overhanging gratings using oblique Chandezon transformations”, J. Mod. Opt. **44**, 1073–1080 (1997).

[120] J. Chandezon, M. T. Dupuis, D. Maystre and G. Cornet, “Multicoated gratings: a differential formalism applicable in the entire optical region”, J. Opt. Soc. Am. **72**, 839–846 (1982).

[121] L. Li, “Multilayer-coated diffraction gratings: differential method of Chandezon *et al.* revisited”, J. Opt. Soc. Am. A **11**, 2816–2828 (1994), **13**, 543 (1996).

[122] T. W. Preist, N. P. K. Cotter and J. R. Sambles, “Periodic multilayer gratings of arbitrary shape”, J. Opt. Soc. Am. A **12**, 1740–1748 (1995).

[123] G. Granet, J. P. Plumey and J. Chandezon, “Scattering by a periodically corrugated dielectric layer with non-identical faces”, Pure Appl. Opt. **4**, 1–5 (1995).

[124] R. Petit, “A tutorial introduction”, in *Electromagnetic Theory of Gratings*, Vol. 22 of Topics in Current Physics, R. Petit (Springer-Verlag, Berlin, 1980), pp. 9–11.

Acknowledgements

At the end of the thesis, while writing the last chapter of the whole document, one thought suddenly breaks into my mind: all this work could not have been carried out without the precious help of a lot of people. It is with pleasure that I want to acknowledge all those colleagues and friends who contributed in so different ways to this final result.

First of all, I would like to thank my thesis advisor, Prof. Hans Peter Herzig, who trusted me by giving me the opportunity to join his group and work in the exciting domain of micro and nano optics. I thank as well Prof. René Dändliker for his competent suggestions and his availability to all kind of optics-related discussions.

I want to address a special thank to Dr. Susanne Quabis, Prof. Olivier Martin and Prof. Urs Staufer who spent a lot of time in reading and correcting my manuscript and finally accepted to become members of my thesis examination jury.

After my stay at the IMT, I optimistically believe that, after all, I perhaps learned something on near-field optics. This miracle could only happen thanks to the help of Dr. Luciana Vaccaro, who brought me to move the first steps in this domain. Thanks, Luciana, for all your support, even in the more difficult moments.

A warm thanks goes to Dr. Laure Aeschimann, who played the role of my SNOM-sister during this near-field adventure spent in Neuchâtel between Breguet 2, Jaquet-Droz 1 and the crêperie "chez Bach et Buck". She is greatly acknowledged for having provided me fantastic micromachined, fully metal-coated, cantilever-based SNOM quartz probes allowing incredible and repeatable measurements.

Writing scientific paper is certainly a good thing while performing a PhD. Unfortunately, how to do it is not always straightforward. I want to thank Dr. Wataru Nakagawa and Dr. Martin Salt for the wise suggestions they gave me about the hazardous and impenetrable world of scientific press.

The success of a good experimental work relies also on the support of a competent technical stuff and broad-band mind colleagues. I had the chance to work with Irène Philipoussis, Marcel Groccia and Dr. Toralf Scharf, who well represented these two aspects. In particular, I thank Irène and Toralf for all the Liquid Crystal stuff and Marcel for his support in light detection problems.

I would like to recall here my colleague, Dr. Carsten Rockstuhl, with whom I shared my office at the IMT, ground floor. I thank him for his precious hints on computational electromagnetics and the good time we had together.

The SNOM-system we built up was based on a highly performing DAQ electronic module produced by a small Italian company. I thank the A.P.E. Research guys Paolo Sigalotti, Dr. Stefano Prato and Christian Sandrin for the competent work they did and their prompt, almost on-line, help.

Even if near-field optical microscopy is a very powerful technique, sometimes it is useful to look to small things without going crazy with super complicated optical alinement. I am glad to Dr. Massoud Dadras who introduced me in the world of electronic microscopy and allowed me to use the fantastic SEM in the CSEM building. I also thank Dr. Michael Pavius for the work on the Dual Beam FIB we did together at the EPFL.

Particular thanks are addressed to Prof. Daniel Courjon and Dr. Thierry Grosjean for the fruitful scientific exchanges we had in Besancon.

During the last four years, a personal universe populated by extraordinary shining souls was always moving around me. I would like to thank all of them by simply recalling their name: Omar, Piero, Gianluca, Mirko, Caspar, Natascia, Laure, Stephanie, Virginie, Chiara, Eugenio, Maura, Francesca, Ilva & Davide, Paola, Iwan, Olivier, Felix, Sylvie, Kim, Mary-Claude, Philippe, Claude, Valerie, Patrick, Andreas, Christian, Vincent.

As a final remark, I would like to thank the European SLAM project and the Swiss program TOP NANO21 for having funded this research activity.

My last thanks are for my parents for all their support.

Publications

E. Descrovi, L. Vaccaro, W. Nakagawa, L. Aeschimann, U. Staufer and H. P. Herzig, "Collection of transverse and longitudinal fields by means of apertureless nanoprobes with different metal coating characteristics", Appl. Phys. Lett. **85**, 5340 (2004).

E. Descrovi, L. Vaccaro, L. Aeschimann, W. Nakagawa , U. Staufer and H. P. Herzig, "Optical properties of microfabricated fully metal coated near-field probes in collection mode", J. Opt. Soc. Am. A **22**, 1432 (2005).

E. Descrovi, L. Vaccaro, L. Aeschimann, W. Nakagawa , U. Staufer, T. Scharf and H. P. Herzig, "On the coupling and transmission of transverse and longitudinal fields into fully metal-coated optical nano-probes", Proc. SPIE, **5736**, 96 (2005).

E. Descrovi, V. Paeder, L. Vaccaro and H. P. Herzig, "A virtual optical probe based on localized Surface Plasmon Polaritons", Opt. Express **13**, 7017 (2005)